DETECTION OF ROTOR AND LOAD FAULTS IN BRUSHLESS DC MOTORS OPERATING UNDER STATIONARY AND NON-STATIONARY CONDITIONS

A Dissertation
Presented to
The Academic Faculty

by

Satish Rajagopalan

In Partial Fulfillment
of the Requirements for the Degree
Doctor of Philosophy in the
School of Electrical and Computer Engineering

Georgia Institute of Technology
August 2006

DETECTION OF ROTOR AND LOAD FAULTS IN BRUSHLESS DC MOTORS OPERATING UNDER STATIONARY AND NON-STATIONARY CONDITIONS

Approved by:

Dr. Thomas G. Habetler, Advisor
School of ECE
Georgia Institute of Technology

Dr. Bonnie H. Ferri
School of ECE
Georgia Institute of Technology

Dr. Ronald G. Harley
School of ECE
Georgia Institute of Technology

Dr. Chris Paredis
School of ME
Georgia Institute of Technology

Dr. Deepak M. Divan
School of ECE
Georgia Institute of Technology

Date Approved: June 14, 2006

To my loving parents

ACKNOWLEDGEMENTS

It has been four and a half years since I started my PhD in early 2002 and it could not be completed without the help of teachers, mentors, colleagues, family, and friends. During my stay at Georgia Tech, I have received assistance, support, and guidance from many people and I am indebted to them. First, I am greatly indebted to Dr. Thomas G. Habetler and Dr. Ronald G. Harley for serving as my co-advisors throughout my tenure at the Georgia Institute of Technology. Their invaluable suggestions at difficult times have contributed a lot towards the success of this thesis. I would like to thank Dr. Deepak Divan for his constant support, motivation, and valuable advice. I have benefited immensely from his knowledge and experience. I would also like to thank Dr. Bonnie Heck Ferri and Dr. Chris Paredis for taking some time of their busy schedule to serve on my PhD defense committee.

This thesis would not have been possible without the valuable advice and guidance from Dr. José Manuel and Dr. José Restrepo from Universidad Simon Bolivar, who patiently took the time to respond to my countless queries. Words would not be enough to thank them for their invaluable help.

I would like to acknowledge Delphi Corporation, NEETRAC, and Powerix Technologies for providing the financial support for my graduate studies. I must also thank the machinists, Lorand Csizar and Louis Boulanger, who were always available and willing to help with the laboratory experimental setup. I would also like to thank Deborah King for patiently putting up with my frequent purchase requests and room reservations.

I was fortunate to have many exceptional peers and colleagues in my research group. Among them, I wish to especially thank Harjeet Johal, Jean-Carlos Hernandez, Afroz Imam, Salman Mohagheghi, Joshua Perkel, George Stefopoulos, Dr. Vinod Rajasekaran, Dr. Rangarajan Tallam, and Dr. Jung Wook Park, for their invaluable input and countless enlightening conversations.

Lastly, I am eternally grateful to my parents for the love, support, and encouragement that have helped to make everything I have accomplished possible.

TABLE OF CONTENTS

LIST OF TABLES

LIST OF FIGURES

SUMMARY

The objective of this research is to advance the field of rotor and load fault detection in brushless direct current (BLDC) motors operating under a variety of operating conditions ranging from constant speed to continuous transient operation. This involves recognizing the rotor and fault signatures produced in BLDC motors, and estimating the severity of the fault both under stationary and non-stationary operating conditions.

A description of various kinds of rotor and load faults that can occur in a BLDC motor operated system is presented. The methods available to detect such faults in motors, including BLDCs operating at a constant speed, are discussed. The effects of various rotor faults on the motor current spectra of a BLDC machine are investigated through experiments. It is also theoretically as well as experimentally demonstrated that faults in gears coupled to electromechanical devices may be detected by monitoring either the voltage or current in the electromechanical device. This may offer an inexpensive alternative to vibration-based diagnostics that require accelerometers, which are very expensive.

Various current-based detection techniques available to detect rotor faults in electric motors operating in transient (non-stationary) operating conditions are reviewed. The techniques available in the mechanical engineering area to detect non-stationary fault signals are also discussed. Three algorithms are proposed to track and detect rotor faults in BLDC motors operating in non-stationary conditions: the windowed Fourier ridge algorithm, the quadratic time-frequency distribution based fault detection algorithm, and

finally the analytic wavelet based method. The windowed Fourier ridges method is easy to implement in real-time and can provide all-time monitoring of motor health. The quadratic time-frequency distribution also offers excellent tracking and may help in fault detection at lower motor speeds due to its better frequency resolution capabilities. The concepts are validated experimentally using sinusoidal, triangular as well as random speed references.

Some selected time-frequency distributions are also implemented on a digital signal processing (DSP) platform to demonstrate the viability of using them in a real-time commercial system. A simple fault metric based on the RMS of the fault ridges is also proposed to aid in fault detection. This fault classifier uses an adaptive thresholding scheme to warn the operator of an impending fault. Finally, a comprehensive condition monitoring scheme to track and detect rotor/load faults in BLDC motors is suggested.

CHAPTER 1

INTRODUCTION AND OBJECTIVE OF RESEARCH

1.1 Problem Statement

Brushless Direct Current (BLDC) motors are one of the motor types rapidly gaining popularity. BLDC motors are used in industries such as appliances, automotive, aerospace, consumer, medical, industrial automation equipment and instrumentation. As the name implies, BLDC motors do not use brushes for commutation; instead, they are electronically commutated. BLDC motors have many advantages over brushed DC motors and induction motors. A few of these are: better speed versus torque characteristics, high dynamic response, high efficiency, long operating life, noiseless operation, higher speed ranges. In addition, the ratio of torque delivered to the size of the motor is higher, making it useful in applications where space and weight are critical factors [1].

More BLDC machines are therefore being used, often in critical high performance applications. Fault diagnosis and condition monitoring of BLDC machines are therefore assuming a new importance. Early detection of faults and asymmetries could allow preventive maintenance to be performed and provide sufficient time for controlled shutdown of the affected process, thereby reducing the costs of outage time and repairs. Though considerable research has been reported in the diagnosis of induction motor faults, much research remains to be done in the diagnosis of particularly rotor faults in BLDC machines.

It is important to be able to detect faults while they are still developing. This is called incipient failure detection. Timely warning that can be followed by maintenance can avoid catastrophic failures and costly long down times. The incipient detection of failures also results in a safer operating environment. The high power density and high efficiency of the permanent magnet (PM) machine have led to the use of this machine in applications in which the high reliability of the machine is a key-feature. Faults can occur in the stator, rotor, inverter, or the external systems connected to the machine. Redundancy and conservative design techniques have been widely adopted for improving the reliability of PM drives against a variety of failures that can occur [2]. However, these techniques are expensive to realize. As an alternative, considerable diagnostic strategies and control schemes can be devised to ensure a fault-tolerant control drive. Vibration monitoring is the most popular choice for condition monitoring but is preferred for use only in large machines where expensive accelerometers could be afforded. Electrical monitoring, which includes current based monitoring, is the most recent of all condition monitoring techniques and is inexpensive as electrical sensors are lower in cost compared to mechanical transducers. The emphasis of this research is therefore on the development of a diagnostic scheme that uses readily available electrical signals in an electric motor, namely the motor stator current and terminal voltage.

The particular application where a BLDC motor is used also plays an important role in the type of diagnostic scheme to be used. Most of the available literature in the field of electrical motor diagnostics assumes that the motor is operating at a constant speed. This however is seldom the case in a real-life application and is even more so in BLDC motors which are often used in servo applications. A motor operating in such a

non-stationary environment has a non-stationary voltage and current signal. The term non-stationary in signal processing literature has a different connotation and is usually described statistically [3]. However, from an electric motor's operating point of view, this term simply refers to an operation where the motor's operating point is continuously changing with time and the motor is never operating at a constant speed throughout its operation. Analysis of non-stationary signals is inherently complicated as simple and commonly used signal processing algorithms such as the fast Fourier transform (FFT) cannot be used. This means that more sophisticated signal processing techniques often under assumptions of local or slow stationarity are needed. Even under these assumptions it is difficult to arrive at a solution that may be effective over a wide range of operating conditions and faults. This aspect of condition monitoring forms an important part of this research and is investigated in detail.

1.2 Objective

The objective of this research is to advance the field of rotor and load fault diagnosis in BLDC machines operating in a variety of operating conditions ranging from constant speed to continuous transient operation. This objective is addressed as three phases in this research.

The first phase experimentally characterizes the effects of rotor faults in the stator current and voltage of a BLDC motor operating at constant speed. To achieve this, the various BLDC motor faults such as eccentricities, unbalanced rotors, and demagnetized rotor magnets are replicated in a laboratory and their effect on the spectrum of the motor voltage and current studied. This helps in better understanding the behavior of rotor defects in BLDC motors.

The second phase investigates faults in loads coupled to a BLDC motor and their effect on the motor current and voltage spectrums. Based on this investigation, methods to detect faults in loads coupled to BLDC motors by monitoring the motor stator current are proposed. The load faults investigated occur in gear trains and coupling arrangements that are connected to a BLDC motor. Several gear defects are replicated in the laboratory and their effect on the motor current and voltage spectrum is studied.

As most BLDC applications involve non-stationary operating conditions, the diagnoses of rotor faults in non-stationary conditions form the third and most important phase of this research. Several signal processing techniques are reviewed to analyze non-stationary signals. Several algorithms are proposed that can track and detect rotor faults in non-stationary or transient current signals. These algorithms are also compared to suggest a recommendation to select an appropriate algorithm for a particular non-stationary operation depending on the available computing power for processing these methods. One common myth is that most of the signals processing techniques used for non-stationary signal analysis are not suitable for commercial implementation. This issue is addressed in detail. Optimal discrete time implementations of some of these techniques are explained. These techniques are also implemented on a digital signal processing (DSP) platform to demonstrate that the proposed methods can be implemented commercially.

1.3 Outline of Dissertation

To familiarize the reader with BLDC motor condition monitoring, Chapter 2 briefly reviews the fundamentals of BLDC motors and the commonly occurring fault

mechanisms. The need for condition monitoring as well as the more commonly used diagnostics techniques are also presented in this chapter.

The previous work in BLDC motor condition monitoring is reviewed in Chapter 3. This includes existing research in academia and industry in the area of non-stationary motor fault diagnostics. A detailed discussion of load fault, especially gear fault, detection is also presented.

The first major contribution of this research is presented in Chapter 4 where the effect of rotor faults on a BLDC motor operating at constant speed, are analyzed. It is shown that different rotor faults such as eccentricities, unbalanced rotors, and demagnetized rotor magnets create unique fault signatures in the motor current spectrum and could be used to diagnose the health of the motor.

Chapter 5 presents a new method to detect faults in loads such as gears connected to BLDC motors by simply monitoring either the stator current or the motor line-to-line voltage, or both. Various gear and coupling faults are implemented. The gear faults include broken teeth, loss of lubrication, and debris inside the gear. The results are also compared with simulation results. It is also shown that the proposed method can distinguish gear and coupling defects from other motor related defects.

Chapter 6 introduces the challenges behind the most important contribution of this research work, namely the detection of faults in BLDC motors operating under non-stationary conditions. A thorough review of the various signal processing techniques that could be used for non-stationary signal analysis is presented. Three of these techniques are developed into fault detection algorithms and are presented in Chapters 7 – 9.

Chapter 10 discusses fault classification schemes that can discriminate a faulty motor from a good one. A comprehensive condition monitoring scheme to classify rotor faults is also provided. Finally, a thorough comparison of the various non-stationary motor diagnostic schemes is carried out that includes the implementation of some of these techniques on an actual digital signal processing (DSP) platform.

Conclusions, contributions, and recommendations for future work are discussed in Chapters 11.

CHAPTER 2

BACKGROUND

To facilitate a clearer understanding of the proposed condition monitoring schemes, the operation of a BLDC motor is now considered in more detail. The various modes by which BLDC motors and their loads fail, and the mechanisms by which they induce fault signatures into the machine vibration and stator current, are also discussed.

2.1 Brushless DC Machines (BLDCM)

The availability of efficient semiconductor switches has provided a means for eliminating the mechanical switching on commutator machines while retaining many of their useful properties. This type of permanent magnet machine is called a brushless DC machine. Figure 2.1 displays some BLDC motors along with a stators and a rotor. These machines have a rectangular air-gap flux density and produce a trapezoidal back-emf in the stator. Back-emf waveforms for an ideal case are shown in Figure 2.2. The BLDC motor is specifically designed to develop nearly constant output torque when excited with six-step switched current waveforms, as shown in Figure 2.3 [4]. The stator windings are generally similar to those of an induction or a synchronous motor except that the conductors are distributed uniformly; that is, concentrated full-pitched windings are used to increase the width of the trapezoidal back-emf plateau region [5]. The rotor typically consists of surface-mounted permanent magnets that span 180-degree magnet arcs with non-overlapping phase belts of 60 degrees electrical.

Figure 2.1: BLDC motors including a stator and a rotor.

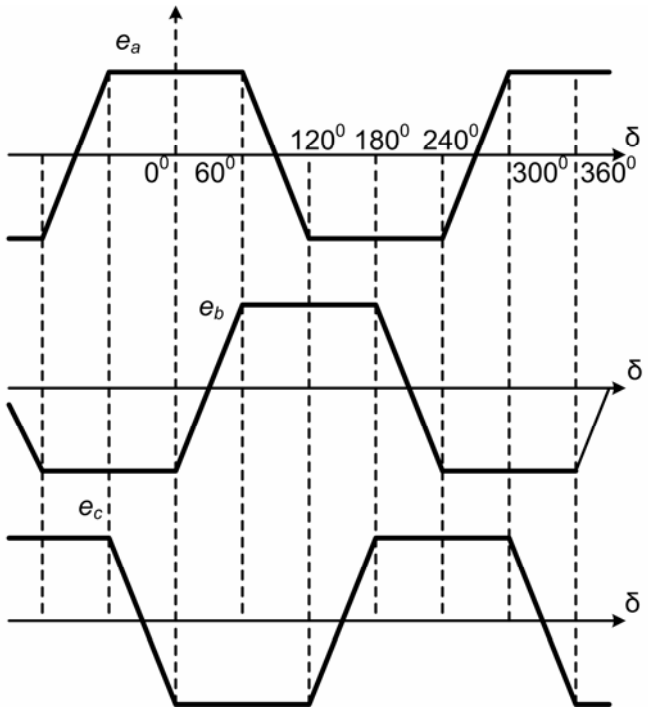

Figure 2.2: Induced emf in three phases.

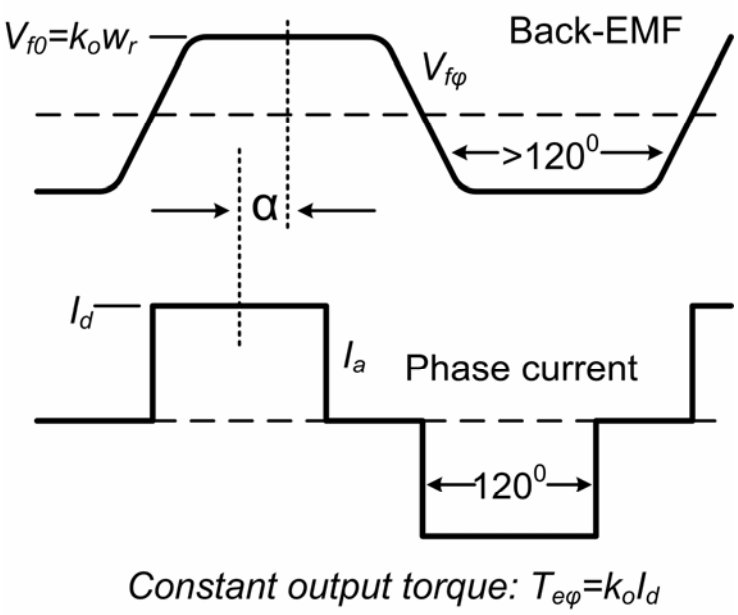

Figure 2.3: Typical back-emf and phase current waveforms for a BLDC motor.

Figure 2.2 shows that during every 60-degree interval, two of the phases have emf waveforms that are flat [5]. In the operation of a BLDC machine, during each of these 60-degree intervals, the two phases with the flat emf waveforms are effectively connected in series and the current through them is controlled, while the third phase is open.

This produces a net electromagnetic torque that does not fluctuate with the rotor position. The phase-to-phase back-emf for a two-pole BLDC machine is given by

$$e_{ph-ph} = k_E \omega_m \quad \text{where} \quad k_E = 4N_s B_f lr\,, \tag{2.1}$$

and the net electromagnetic torque for a two-pole BLDC machine is given by

$$T_{em} = k_T I \quad \text{where} \quad k_T = 4N_s B_f lr\,, \tag{2.2}$$

where k_E is the voltage constant in V/(rad/s), ω_M is the rotor speed in (rad/s), N_s is the total number of turns per phase in the concentrated winding, B_f is the average air-gap flux

density in Tesla, l is the length, r is the radius of the rotor in meters, k_T is the torque constant in Nm/A, I is the converter's DC link current in Amps, and $k_E = k_T$.

Equation 2.2 is particularly significant since it indicates that the torque developed by the machine can be controlled directly by varying the current amplitude. This similarity to a conventional DC motor gives the motor the name *brushless DC*. Despite the popularity of this name, brushless DC is actually quite misleading since the trapezoidal back-EMF machine is fundamentally a synchronous AC machine and not a DC machine as the name implies [6]. Thus, the BLDC motor behaves like a commutator motor. Its no-load speed is approximately proportional to the applied direct voltage, and the speed reduces somewhat with torque because of the voltage drop across the winding resistances.

The process of switching the current to flow through only two phases for every 60-degree rotation of the rotor is called electronic commutation. The motor is supplied from a three-phase inverter. The switching actions can be simply triggered by the use of signals from position sensors that are mounted at appropriate positions around the stator. One of the more common position sensors is a set of three Hall-effect sensor switches mounted in or near the machine's air gap to detect the impinging magnetic field of the passing rotor magnets [7]. When mounted at 60-degree electrical intervals and aligned properly with the stator phase windings, these Hall switches deliver digital pulses that can be decoded into the desired three-phase switching sequence. A BLDC motor drive with a six-step inverter and Hall position sensors is shown in Figure 2.4. Such a drive usually also has a current loop to regulate the stator current, and an outer speed loop for speed control. There are only six discrete inverter switching events during each electrical cycle.

Only two inverter switches, one in the upper inverter bank and one in the lower inverter bank, are conducting at any instant. These discrete switching events ensure that the sequence of conducting pairs of stator terminals (Figure 2.5) is maintained. In Figure 2.5, the conducting phases are indicated during each 60-degree interval, where one phase has a current, $+I$, (indicated by +), one phase has a negative current, $-I$, (indicated by -), and the third phase has zero current (open) [5]. Here, I is assumed to be a constant current through each of the three phases while the rotor is rotating ($I_a = I$). Thus, during every 60-degree interval a constant current, I, flows through any two of the motor phases resulting in a net constant electromagnetic torque [5]. This sequence of conducting pairs is essential to the production of a constant output torque.

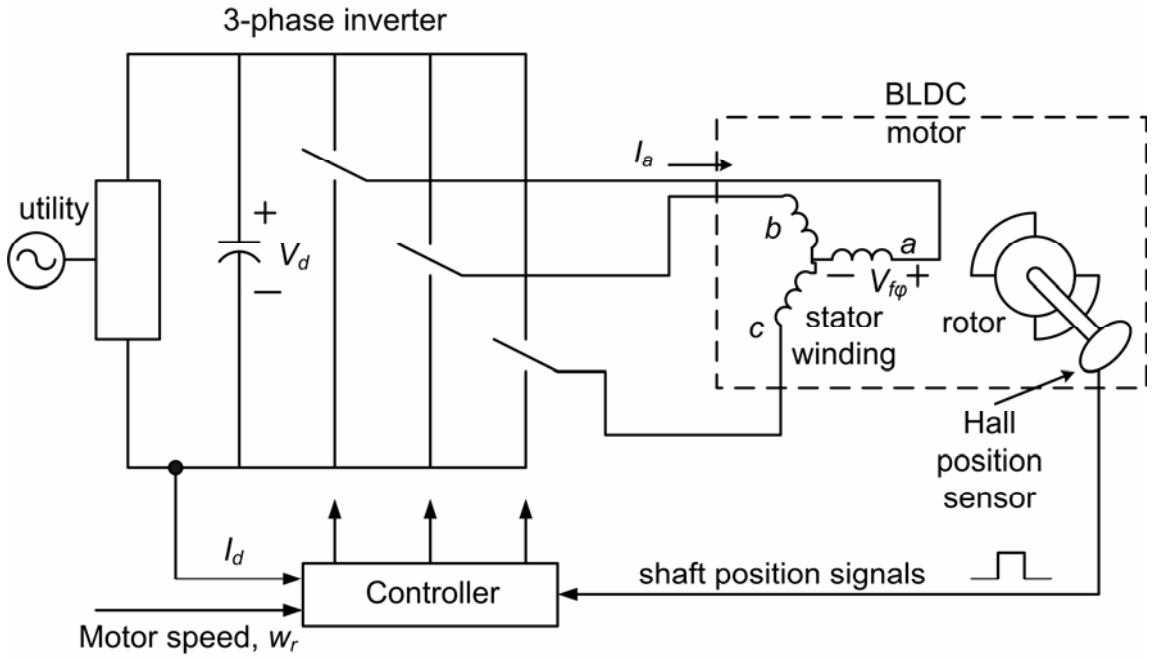

Figure 2.4: Electronically commutated BLDC motor drive.

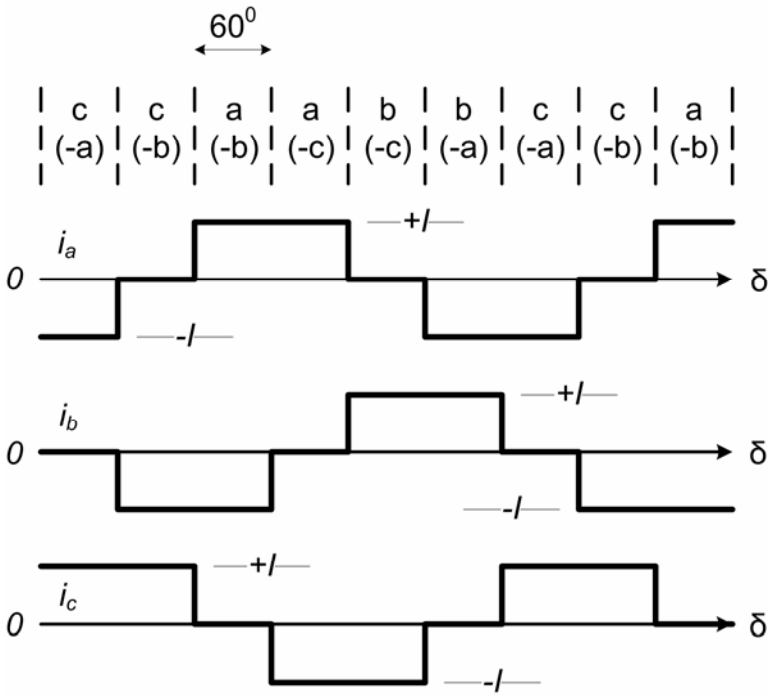

Figure 2.5: Phase currents for a constant torque in a BLDC motor.

The phase shift angle, α, indicated in Figure 2.3, is typically set by the physical alignment of the rotor angular position sensor that performs the self-synchronization, thereby controlling the electronic commutation. The angle, α, is held as near to zero as possible to maximize the torque and the output power. This corresponds to the standard practice of aligning the commutator brushes in a conventional DC motor, such that the brushes are orthogonal to the magnetic flux imposed by the stationary field.

2.2 Need for Condition Monitoring in BLDC Machines

The BLDC motors have many advantages over brushed DC motors and induction motors. A few of these are better speed versus torque characteristics, high dynamic response, high efficiency, long operating life, noiseless operation, and higher speed ranges. In addition, the ratio of the torque delivered to the size of the motor is higher,

making it useful in applications where space and weight are critical factors [1]. Therefore, BLDC machines are being used more often in critical high-performance applications. Fault diagnosis and condition monitoring of BLDC machines are therefore assuming a new importance.

Condition monitoring is defined as the continuous evaluation of the health of the plant and equipment throughout its service life [8]. It is important to be able to detect faults while they are still developing. This is called incipient failure detection. A timely warning that can be followed by maintenance can avoid catastrophic failures and costly long down times. The incipient detection of motor failures also provides a safe operating environment.

The high power density and high efficiency of the permanent magnet (PM) machine have led to its use in applications where the high reliability of the machine is a key-feature. Redundancy and conservative design techniques have been widely adopted for improving the reliability of PM drives against the variety of failures than can occur [2]. However, these techniques are expensive to realize. As an alternative, considerable diagnostic strategies and control schemes can be devised to ensure a fault-tolerant control drive.

2.3 Internal Faults in BLDC Motors

Potential faults inside a BLDC motor can be categorized as stator faults, inverter faults, rotor faults, and bearing faults. The detection of rotor and load-related faults in BLDC machines is the main focus of this research.

2.3.1 Stator Faults

The most frequently occurring stator fault is the breakdown of the winding insulation. This usually occurs in the region where the end windings enter the stator slots. It is caused by large electrical voltage stresses, electro-dynamic forces produced by winding currents, thermal aging from multiple heating and cooling cycles, and mechanical vibrations from internal and external sources. This winding insulation breakdown can result in turn-to-turn faults that eventually lead to short circuits to ground, resulting in the so-called grounded stator windings. Recent research [9] has been done to detect the fault while it is still in the turn-to-turn fault stage, so that the machine can be shut down before the more catastrophic grounded stator winding faults occur.

2.3.2 Inverter Faults

Almost all permanent magnet motors including the BLDC motors are inverter-fed. There are also some machines that are line started. However, the latter machines need damper windings. Many faults can occur in the inverter, such as the loss of one or more of the switches of a phase, the short circuit of a switch, and the opening of one of the lines to the machine.

2.3.3 Rotor Faults

Potential rotor faults in BLDC machines are eccentricities, damaged rotor magnets, and damaged Hall sensors. All of these rotor faults cause problems such as vibration and noise. They also cause dynamic problems by adding on to the motor's torque pulsations. These faults are explained here in more detail.

2.3.3.1 Rotor Eccentricities

In an ideal machine, the rotor is center-aligned with the stator bore, and the rotor's center of rotation is the same as the geometric center of the stator bore as shown in Figure 2.6. A rotor eccentricity is a condition of unequal air gap that exists between the stator and the rotor. Air-gap eccentricity can occur in the form of static or dynamic eccentricity. In the case of a static eccentricity, the position of the minimum radial air-gap length is fixed in space. Typical causes of static eccentricity include stator core ovality or incorrect positioning of the rotor or the stator at the commissioning stage. A dynamic eccentricity occurs when the center of the rotor is not at the center of rotation and the minimum air gap revolves with the rotor. This means that a dynamic eccentricity is a function of space and time. Typical causes of a dynamic eccentricity include bent shafts, mechanical resonances at critical speeds, and bearing wear. Figure 2.7 shows an illustration of how the rotor would rotate in the presence of each type of air-gap eccentricity [10].

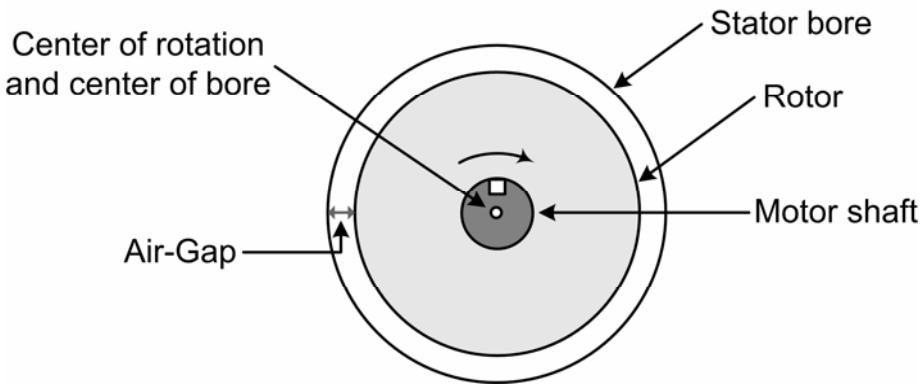

Figure 2.6: Ideal electric motor (non-eccentric air-gap).

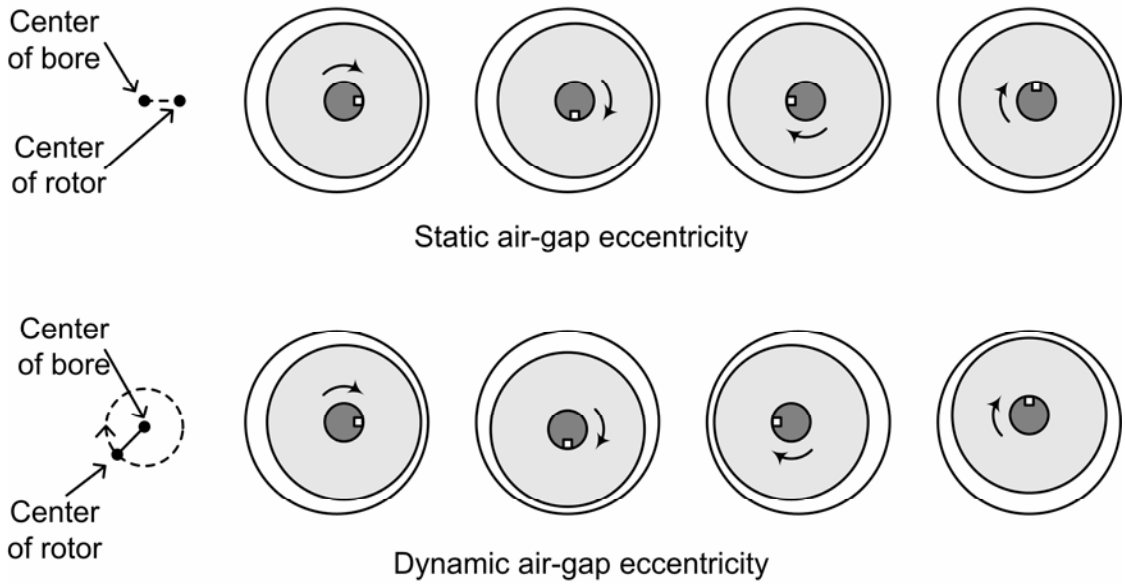

Figure 2.7: Illustration of static and dynamic air-gap eccentricity.

When the eccentricity becomes large, the resulting unbalanced radial forces (also known as unbalanced magnetic pull or UMP) can cause a stator-to-rotor rub, which can result in damage to the stator and the rotor [11]. In the case of static eccentricity, this is a steady pull in one direction. This makes the UMP in a static eccentricity difficult to detect unless special equipment is used, which is impractical for motors in service [12, 13]. A dynamic eccentricity on the other hand produces a UMP that rotates at the rotational speed of the motor and acts directly on the rotor. This makes the UMP in a dynamic eccentricity easier to detect by vibration or current monitoring.

2.3.3.2 Damaged Rotor Magnet

An air-gap flux disturbance that results from some anomaly of the permanent magnets is also an important fault that occurs frequently in BLDC motors. It is well known that some permanent magnets (Nd-Fe-B) corrode and can lead to disintegration [14]. Cracks that form during manufacturing can lead to disintegration at high speeds

[15]. A chipped magnet may also end up in the air gap, causing increased friction and potential damage to the stator insulation. The flux disturbances can also be caused by partial demagnetization of the magnets, which occurs for various reasons [16]. These flux disturbances may cause unbalanced magnetic pull between the stator and the rotor resulting in more stress on the bearings. This may eventually lead to bearing failures.

2.3.3.3 Damaged Hall Sensors

Another rotor fault that is encountered in BLDC motors is a Hall-sensor failure. Hall sensors are often used in BLDC motors for rotor position detection to determine the current commutation instances. The loss of a Hall sensor results in torque pulsations when the rotor is moving. During such a failure, the control is unable to start a BLDC motor.

2.3.4 Bearing Faults

The majority of electrical machines use rolling element bearings. Each bearing consists of two rings called the inner and the outer rings. A set of balls or rolling elements placed in raceways rotate inside these rings. Bearing failures are responsible for the highest incidence of recorded motor failures [17]. A continued stress on the bearings causes fatigue failures, usually at the inner or outer races of the bearings [18]. Small pieces break loose from the bearing, called flaking or spalling. These failures result in rough running of the bearings that generates detectable vibrations and increased noise levels. This process is helped by other external sources, including contamination, corrosion, improper lubrication, improper installation, and brinelling. The shaft voltages and currents are also sources for bearing failures [19]. These shaft voltages and currents result from flux disturbances such as rotor eccentricities.

2.4 External Faults in BLDC Machines

Faults may also occur in systems external to the BLDC machine that may have an impact on its operation. Motors are often coupled to mechanical loads and gears. Several faults can occur in this mechanical arrangement. Examples of such faults are coupling misalignments and faulty gear systems that couple a load to the motor. Faults in the loads can cause discontinuities in the production schedule, thus lowering manufacturing efficiency. In some applications such as aircrafts, the reliability of gears may be critical in safeguarding human lives. For this reason, the detection of load faults (especially related to gears) has been an important research area in mechanical engineering for some time [20-23].

2.4.1 Gear Faults

2.4.1.1 Common Types of Gears

The most common types of gears in use are the spur gears, helical gears, bevel gears, worm gears, and straight (rack type) gears [24-27]. All these gears have a driving wheel and a driven wheel, but differ in the shape and arrangement of the wheels. Spur gears are characterized by teeth that are perpendicular to the face of the gear. These are by far the most commonly used gears and are generally the least expensive. Spur gears cannot be used when a direction change between the two shafts is required [24, 26]. A helical gear is similar to the spur gear except that the teeth are at an angle to the shaft, rather than being parallel to it. Therefore, the teeth on a helical gear are longer than the teeth on a spur gear of equivalent width. Helical gears have the major disadvantage of being expensive. They are used less frequently and are also slightly less efficient than a spur gear of the same size [24, 26]. The bevel gear is primarily used to transfer power

between intersecting shafts. The teeth of these gears are formed on a conical surface. Standard bevel gears have teeth that are cut straight, and are all parallel to the line pointing to the apex of the cone on which the teeth are based. However, they suffer from limited availability, cannot be used for parallel shafts, and can become noisy at high speeds [24, 26]. Worm gears are special gears that resemble screws, and can be used to drive spur gears or helical gears. Worm gears, like helical gears, allow two non-intersecting 'skew' shafts to mesh. Normally, the two shafts are at right angles to each other. One important feature of the worm gear meshes is their irreversibility. When a worm gear is turned, the meshing spur will turn, but turning the spur will not turn the worm gear. The resulting mesh is 'self-locking' and is useful in racheting mechanisms [24, 26]. However, they will tolerate large loads and are used in applications where high speed ratios are desired. Straight gears or racks are used to convert the rotational motion to translational motion by means of a gear mesh. They are in theory a gear with an infinite pitch diameter [24, 26].

2.4.1.2 Faults in Gear Trains

Gears are unusual in that they experience a number of different forms of damage of widely varying severity and importance. Roughly in order of importance, gear failures may be classified as follows: pitting, micropitting (gray staining), scuffing, root cracking, wear, scoring, plastic deformation, and case cracking [28]. Though pitting occurs most frequently, it is often not serious. Damage resulting from wear can be further classified as local wear, distributed wear, and gear backlash because of tooth thinning. Gear wear resulting from tooth thinning or an increase between the centers of the gears, is one of the more frequent failures. The thinning of teeth results in an increased backlash, resulting in

improper gear operation. Local gear wear involves damage to one or two teeth of a gear wheel. Distributed gear wear on the other hand occurs over a long period of time and involves the wearing down of a large number of teeth as a result of prolonged gear use. A different kind of fault, scuffing, occurs when the oil film breaks down to allow metal-to-metal contact. This results in a local welding followed by a tearing of the surface as the welds are sheared because of the moving gears. Scoring is a variant of scuffing, which occurs as a result of insufficient lubrication.

2.4.2 Misalignments

Misalignments are other common faults that occur in the shaft coupling of a motor that is not properly aligned or positioned with its mechanical load [29, 30]. Misalignments are categorized into two types: angular (horizontal) and radial (vertical) misalignments. These misalignments cause a slight unbalance in the rotor and produce undesired vibrations. Such vibrations eventually weaken the coupling and cause it to fail. They also stress the motor bearings thereby lowering their life.

2.5 Condition Monitoring Techniques

The condition monitoring of electrical and mechanical devices has been in practice for quite some time now. Several methods have evolved over time but the most prominent techniques are thermal monitoring, vibration monitoring, and electrical monitoring.

2.5.1 Thermal Monitoring

The thermal monitoring of electrical machines is accomplished either by measuring the local or bulk temperatures of the motor, or by parameter estimation. The

former method requires the installation of thermocouples. This is rarely done in small machines. An example of thermal monitoring by parameter estimation for small PMSMs is given in [31]. Here, a thermal model of the electrical machine is first developed from the machine electrical quantities, namely the current and voltage. This thermal model is then used to estimate the temperature of the motor and identify faults. Thermal monitoring can in general be used as an indirect method to detect some stator faults (turn-to-turn faults) and bearing faults. In a turn-to-turn fault, the temperature rises in the region of the fault, but this might be too slow to detect the incipient fault before it progresses into a more severe phase-to-phase or phase-to-neutral fault. In the case of detecting bearing faults, the increased bearing wear increases the friction and the temperature in that region of the machine. This is a slow process that can be detected by thermal monitoring.

2.5.2 Vibration Monitoring

A vibration monitoring is based on the concept that mechanical vibrations at various frequencies are related to identifiable sources in the machine and can be used to provide an indication of the condition of the machine. Bearing faults, rotor eccentricities, gear faults and unbalanced rotors are the best candidates for vibration based diagnostics. Almost all the rotor and bearing faults cause mechanical vibrations at specific frequencies [18, 32]. A listing of possible machine faults and their related vibration frequencies is given in [30].

The vibration energy of the machine is measured in units of one of three related quantities: displacement, velocity, or acceleration. These measurements are accomplished using displacement probes, velocity transducers, or accelerometers

respectively. The vibration monitoring of electric machines is accomplished through the use of broad-band, narrow-band, or spectral (signature) analysis of the measured vibration energy of the machine [30]. Vibration-based diagnostics is the best method for fault diagnosis, but needs expensive accelerometers and associated wiring. This limits its use in several applications, especially in small machines where cost plays a major factor in deciding the condition monitoring method. Another vibration-based method is to measure the acoustic vibration levels [30]. However, this is sensitive to changes in the measurement location because of reflections and reverberations of sound emanating from the machine and from other machines in the vicinity.

2.5.3 Electrical Monitoring

Monitoring the stator current, the stator voltage, sensing the air-gap flux, measuring shaft voltages and currents, and monitoring feedback signals (for example the Hall sensor position feedback of a BLDC motor), all fall under the category of electrical monitoring. These methods are used to detect various kinds of machine and inverter faults. The most common form of signal analysis technique used in electrical monitoring is the current spectra analysis, often termed as “Motor Current Signature Analysis (MCSA)” [33]. It has been shown that there is a relationship between the mechanical vibration of a machine and the magnitude of the stator current component at the corresponding harmonics [34]. For increased mechanical vibrations, the magnitude of the corresponding stator current harmonic components also increases. This is because the mechanical vibration modulates the air gap at that particular frequency. These frequency components then show up in the stator inductance, and finally in the stator current. For this reason, the MCSA can be used to detect rotor and bearing faults. As the flux density

in the air gap is defined as the product of the winding magneto-motive force (MMF) and the air-gap permeance, variations in either of these will cause anomalies in the flux distribution. The changes in the winding MMF mainly depend on the winding distribution. On the other hand, the air-gap permeance depends on numerous effects including stator slots, out-of-round rotors, air-gap eccentricities caused by mechanical unbalance and misalignment, and mechanical shaft vibrations caused by bearing or load faults [33]. The purpose of the MCSA is to detect changes in a machine's permeance by examining the current signals [35]. The MCSA uses the current spectrum of the machine for locating characteristic fault frequencies. The spectrum is obtained using a Fast Fourier Transformation (FFT) that is performed on the signal under analysis. The fault frequencies that occur in the motor current spectra are unique for different motor faults. Electrical monitoring holds much promise for the future as it is inexpensive and reliable.

2.6 Conclusions

This chapter has briefly reviewed the construction and operation of a BLDC motor. A description of various kinds of rotor and load faults that can occur in a BLDC motor operated system has been presented. The more commonly used condition monitoring techniques available to detect such faults has also been presented.

A review of the previous work in the condition monitoring of BLDC machines is presented next in Chapter 3.

CHAPTER 3

PREVIOUS WORK ON CONDITION MONITORING OF BLDC MOTORS

Electrical monitoring, which includes current based monitoring, is the most recent of all condition-monitoring techniques, and is the focus of the present research because of its low cost. A literature survey revealed a number of methods that have been used to detect the many different faults discussed in Chapter 2. This chapter reviews and summarizes the existing research that is pertinent to these topics and is limited to the detection of rotor and load related faults.

3.1 Rotor Fault Detection

3.1.1 Detecting Rotor Eccentricity

The detection of rotor eccentricities in induction motors that operate at constant speed has been the focus of ongoing research activities in industry as well as academia. Several researchers have shown that rotor defects in induction motors operating at a constant speed affect certain characteristic frequency components in the machine stator current and such rotor defects can be identified by monitoring the amplitude of these harmonic components [11, 13, 35]. This popular method is called Motor Current Signature Analysis (MCSA) [33]. In MCSA, the frequency spectrum of the stator current is computed using a fast Fourier transform (FFT). The rotor fault frequencies are then identified from the current spectrum and monitored to detect the severity of the fault. For

example, a dynamic eccentricity in induction motors [35] causes current components at frequencies given by

$$f_{de} = f_e \pm k\frac{f_e(1-s)}{P/2}, \tag{3.1}$$

where f_{de} is the dynamic eccentricity frequency, f_e is the fundamental frequency, s is the slip, and k is any integer

A more general expression that predicts characteristic frequencies of both static and dynamic eccentricity in induction motors is given [11] by

$$f_{sh} = \left\{\left(kR \pm n_d\right)\frac{2(1-s)}{P} \pm n_{\omega s}\right\} f_e, \tag{3.2}$$

where f_{sh} is the frequency of the current component that has to be monitored to detect the eccentricity, n_d = 1,2,3,… (the eccentricity order), s is the slip, P is the number of poles, $n_{\omega s}$ is the order of stator time harmonics that are present in the power supply driving the motor ($n_{\omega s}$ = ±1,±3,±5,…), R is the number of rotor slots, and k = 1, 2, 3,… is the order of slot harmonic produced due to rotor slots. Setting n_{rt}, n_d, and $n_{\omega s}$ to the appropriate integers yields the frequencies that have to be monitored to detect dynamic eccentricity, while setting n_d = 0 yields the principal slot harmonics that have to be monitored to detect static eccentricity.

The proof for the equations (3.1 - 3.2) are based on the fact that the eccentricities cause changes in the permeance. The flux density in the air gap is given as a product of the MMF and the air-gap permeance, P_g. For the a-phase stator winding, this flux density can be expressed as

$$B_{as}\left(\varphi_s,\theta_{rm}\right)=MMF_{as}\left(\varphi_s\right).P_g\left(\varphi_s,\theta_{rm}\right), \tag{3.3}$$

where φ_s is the angular measure around the stator air-gap, and θ_{rm} is the mechanical rotor angular position. The air-gap permeance can be considered to be a conductance to the MMF produced by the winding current and is inversely proportional to the length of the air gap. Under the initial modeling assumption, the permeance is constant because of the uniform air gap. However, any change in the air-gap length causes a variation of the permeance. These variations can be expressed as a Fourier series [11] and are either stationary (static eccentricity),

$$P_g\left(\varphi_s\right)=P_0+\sum_n P_n\cos\left[n\varphi_s+\alpha_n\right], \tag{3.4}$$

or rotating (dynamic eccentricity),

$$P_g\left(\varphi_s,\theta_{rm}\right)=P_0+\sum_n P_n\cos\left[n\left(\varphi_s-\theta_{rm}\right)+\alpha_n\right], \tag{3.5}$$

in nature where P_0 is the average air-gap permeance and P_n is the magnitude of the n-th permeance. An approximation of $n=1$ results in the equations (3.6) and (3.7); and is used to derive equation (3.1). The more general expression of (3.2) is obtained by directly using the above equations while also introducing the effects of the stator slots.

$$P_g\left(\varphi_s\right)=P_0+P_1\cos\varphi_s, \tag{3.6}$$

$$P_g\left(\varphi_s,\theta_{rm}\right)=P_0+P_1\cos\left(\varphi_s-\theta_{rm}\right), \tag{3.7}$$

The equations (3.6) and (3.7) are used to calculate the air-gap flux density from (3.3). Once the air-gap flux density is calculated, it is possible to calculate the magnetic flux linking a single coil in the machine by integrating over the span of the coil as shown in (3.8) for a two-pole machine,

$$\Phi_{lsas}\left(\varphi_s,\theta_{rm}\right)=\int_{\varphi_s}^{\varphi_s+\pi} B_{as}\left(\xi,\theta_{rm}\right)\, r\, l\, d\xi, \tag{3.8}$$

where r is the mean radius of the air-gap and l is the axial length of the rotor. The flux linkage for the entire winding is then determined by summing the effects of each coil in the winding. The derivation for the a-phase stator flux linkage will be explained here as an example. The winding distribution, $N_{as}(\varphi_s)$, of the a-phase stator winding of a two-pole machine can be defined to be

$$N_{as}\left(\varphi_s\right)=\frac{N_s}{2}\cos\left(\varphi_s\right), \tag{3.9}$$

where N_s is the number of turns in the sinusoidally distributed winding. The total a-phase stator flux linkage is the sum of two components:

1. The flux linkage for the entire winding distribution of (3.9) produced as a result of the main flux of (3.8).
2. The flux linkage because of the stator end winding leakage inductance.

The total a-phase stator flux linking the a-phase stator winding of a two-pole machine is therefore given by

$$\lambda_{asas} = L_{ls} i_{as} + \int_{\pi}^{2\pi} N_{as}\left(\varphi_s\right) \Phi_{lsas}\left(\varphi_s, \theta_{rm}\right) d\Phi_s \,, \tag{3.10}$$

where i_{as} accounts for the a-phase stator current. This flux linkage is finally used to calculate the inductances, which reflect the change in air-gap permeance. The a-phase stator winding self inductance can be expressed as

$$L_{asas} = \frac{\lambda_{asas}}{i_{as}} = L_{ls} + L_{ms} \,, \tag{3.11}$$

These calculations are repeated for all the self and mutual inductances of a three-phase, two-pole induction motor with the eccentricity described by (3.6) and (3.7). Once these inductances are calculated, they can be substituted into the d-q machine flux linkage equations, which yield the fault frequencies depicted in equations (3.1) and (3.2). A more detailed derivation can be found in [11, 30].

Another method to detect the eccentricities using shaft signals has been proposed by Hsu and Stein [19]. The eccentricities cause the flux to link the shaft, inducing voltages across the shaft ends. If there is an electrical path between the shaft ends, a current will flow (usually through the bearings). This establishes a correlation between the shaft signals and eccentricities of salient-pole synchronous machines. The magnitude and the thickness of shaft-signal loci reflect steady and dynamic eccentricities and can be used for detecting these faults.

In [36], Le Roux et al. have shown that the equations (3.1) and (3.2) can be adapted for use in the detection of rotor defects in permanent magnet synchronous machines (PMSMs). They demonstrated through simulations and experiments that the

MCSA can be used to detect rotor eccentricities in a PMSM by monitoring unique frequency components (f_{de}) given by,

$$f_{de} = f_e \pm k\frac{f_e}{P/2}. \tag{3.12}$$

The same concept is extended to the BLDC machines in [36], where Le Roux has shown through finite-element (FE) simulations, the presence of similar frequency components in the stator current of a BLDC motor. The 2D FE model of a six-pole BLDC motor designed in ANSOFT® RMxprt is shown in Figure 3.1. With no current flowing in the windings, the magnetic fields are solved by ANSOFT® MAXWELL 2D for a specific rotor position. This yields the parametric solution for the permanent magnet flux linking the stator windings and the winding inductances. The rotor is then rotated by a pre-specified angle (3^O mechanical) and the flux linkages and inductances re-calculated. This process is repeated until the rotor is rotated through a full revolution, which takes 120 steps. This process gives flux linkages and inductances as a function of rotor position, which is used later in look-up tables during a transient simulation of the complete BLDC motor drive system executed in MATLAB®. The parametric and the transient solutions are solved for the healthy motor, as well as for motors with rotor faults such as a static eccentricity, a dynamic eccentricity, and a demagnetized rotor magnet.

The Fourier analysis of the stator current obtained from the MATLAB simulations have revealed that the fault harmonics (for a six-pole BLDC motor, the rotor fault frequencies occur at $1/3^{rd}$, $2/3^{rd}$, $4/3^{rd}$, and $5/3^{rd}$ times the fundamental frequency as computed from (3.10)) for a defective motor are significantly different from a healthy

motor and this can be used to monitor the motor's health [36]. However no experimental validation has been provided to verify the claim.

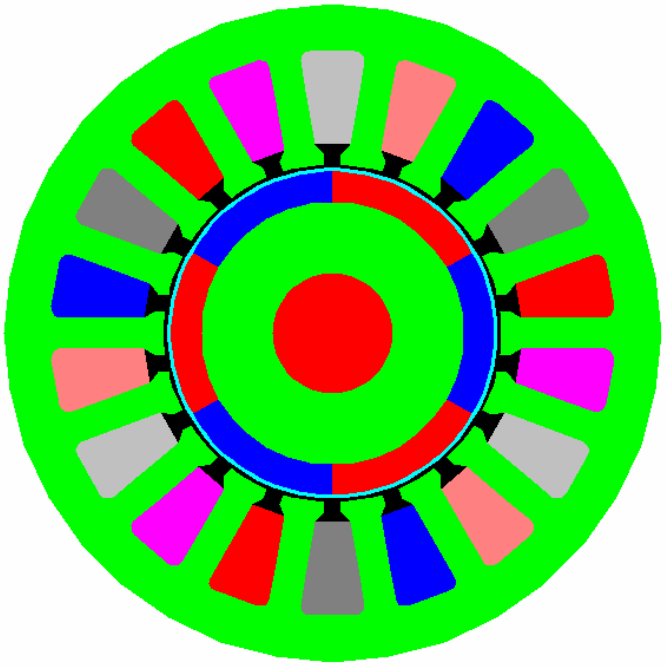

Figure 3.1: 2D FE model of a six-pole BLDC motor in MAXWELL 2D®.

3.1.2 Detecting Damaged Rotor Magnets

In [36], Le Roux has again demonstrated through finite-element simulations that the flux disturbances as a result of damaged magnets in BLDC and PMSM motors produce fault frequencies similar to the ones produced by a dynamic eccentricity. Again, no experimental verification has been provided to validate the claim.

In [36], Le Roux has also demonstrated that the damaged rotor magnets in a BLDC motor can also be detected by estimating the strength of the permanent magnet. This is simply the mean value of the added back-EMFs of the two conducting phases in

any particular 60-degree rotor position region. The estimated torque constant is then given by

$$\hat{K}_t = \frac{V - 2r_s I_{dc}}{\omega_r} = \frac{E}{\omega_r}, \tag{3.13}$$

where the supply voltage (V) and the DC-link current (I_{dc}) are averaged over every 60-degree region of the rotor position during steady-state operation, r_s is the stator resistance per phase, ω_r is the rotational velocity of the BLDC motor, and E is the back-EMF. This estimation neglects the effect of stator inductances, and works well when the back-EMF (E) is used directly, but this is not available on a physical machine. However, the estimated magnet strength is independent of other faults such as the dynamic and static eccentricities, implying that this estimation could still be used to detect a decrease in the magnet strength.

3.2 Load Fault Detection

Load fault detection (especially related to gears), has been a popular research area in mechanical engineering for some time. However, it has not attracted much attention from the electrical engineering community as most of the diagnostic strategies have focused on vibration analysis. A few papers describe the use of the motor to detect load faults such as load imbalance, etc. Even those however, typically, lump load faults as "unbalanced or misaligned load", along with motor faults such as rotor eccentricity [37]. As such, there has been little effort to use the motor as a tool to identify problems with the load it is driving, let alone to discriminate among various kinds of load faults.

3.2.1 Detection of Gear Faults

The most common method of diagnosing gear faults is through the vibration produced by them. Typically, the vibration can be measured using an accelerometer. The vibration spectrum is a good indicator of the various faults that occur in gear systems. One important element of gearbox vibrations is the periodic signal at the tooth-meshing rate. This so-called gear meshing frequency is easily calculated by multiplying the number of teeth on a gear with the rotating speed of the gear [38]. If the gear meshing amplitude increases without any corresponding change in speed or load, it indicates a problem is developing in the gearbox. Uniform or distributed wear tends to show up as an increase of the tooth-meshing component and its harmonics, more particularly the latter, and possibly as a simultaneous decrease in the ghost components [35, 36]. Local faults, such as cracked teeth, spalls, and localized pitting, give rise to components over a wide frequency range, partly by modulation (for the frequencies around and above the tooth meshing frequency) and partly as additive impulses. More distributed faults like misalignments and eccentricities, tend to give higher level of sidebands more closely grouped around the tooth-meshing frequency. Sidebands are produced simultaneously by amplitude and frequency modulation [39]. The interaction depends in a complex way on the dynamic response characteristics of the gearbox components. The aforementioned changes in the vibration signals can be detected using a number of techniques, of which the most important are synchronous signal averaging, spectrum analysis, and cepstrum analysis [39, 40].

Even though vibration based diagnostic methods are reliable, the high cost of accelerometers and associated wiring used in measuring vibration is a disadvantage in

many cost-sensitive arenas such as the automotive sector. In such cases, the detection of gear faults from the analysis of the motor current offers a cost-effective solution. In [33], Kliman and Stein have reported gear tooth meshing frequencies in the current frequency spectrum of motor operated valves (MOVs) using induction motors at constant speed, but have not been able to explain the origin and nature of these frequencies.

In [41], Attia et al. have demonstrated that damaged gear teeth can be detected by monitoring the stator current spectrum of an induction motor coupled to a gear system and operating at a constant speed. It is also reported by the same authors that local and distributed teeth damages produces unique fault harmonics around the fundamental frequency component spaced at the gear frequency. For example, a defect in the pinion causes stator current harmonics given by

$$f_{pin,h} = f_s \pm k * f_r \ , \quad k = 1, 2, 3,... \ , \tag{3.14}$$

where f_r is the pinion frequency and f_s is the electrical supply frequency. Similarly, a defect in the driven wheel produces fault frequencies at

$$f_{driw,h} = f_s \pm k * f_d \ , \quad k = 1, 2, 3,... \ , \tag{3.15}$$

where f_d is the driven wheel frequency.

3.2.2 Detection of Misalignments

Misalignments are usually easy to spot in the vibration spectrum and appear as harmonics at twice the rotating speed of the system [29, 30]. These harmonics appear in the stator current as unique spectral components given by

$$f_{mis} = f_e \pm 2 f_r , \tag{3.16}$$

where f_r is the rotational speed of the motor, and f_e is the electrical fundamental frequency of the stator current.

3.3 Fault Detection in Non-Stationary Operating Conditions

It has been assumed so far that the electric motor has been operating in a steady state condition (constant speed application). This fundamental assumption of stationarity allows the use of the well known method of Fourier Transformation in the frequency analysis of currents, voltages, and vibration signals to detect various rotor and mechanical faults in an electrical machine. However, there are several applications where the motor is never operating at a constant speed or load. Such transient or non-stationary applications include automobile power steerings and emergency breakers. In such applications, the motor is operating in a non-stationary state that may even include long spells of no activity (motor standing still). The motor operating in such a non-stationary environment has a non-stationary voltage, current and vibration signal. A typical segment of the stator current of a BLDC motor operating in such a non-stationary state is shown in Figure 3.2 in which both the frequency and amplitude are changing continuously. Analysis of non-stationary signals is inherently complicated and sophisticated signal processing techniques are often needed as will be discussed later in this section.

3.3.1 Non-Stationary Signal Analysis in Vibration-Based Fault Diagnostics

There has been a significant amount of work in the mechanical engineering area, where researchers have used sophisticated signal processing techniques to identify faults

in gears operating in transient conditions. As some of these techniques could be applied to electrical engineering, a brief review of them is presented here.

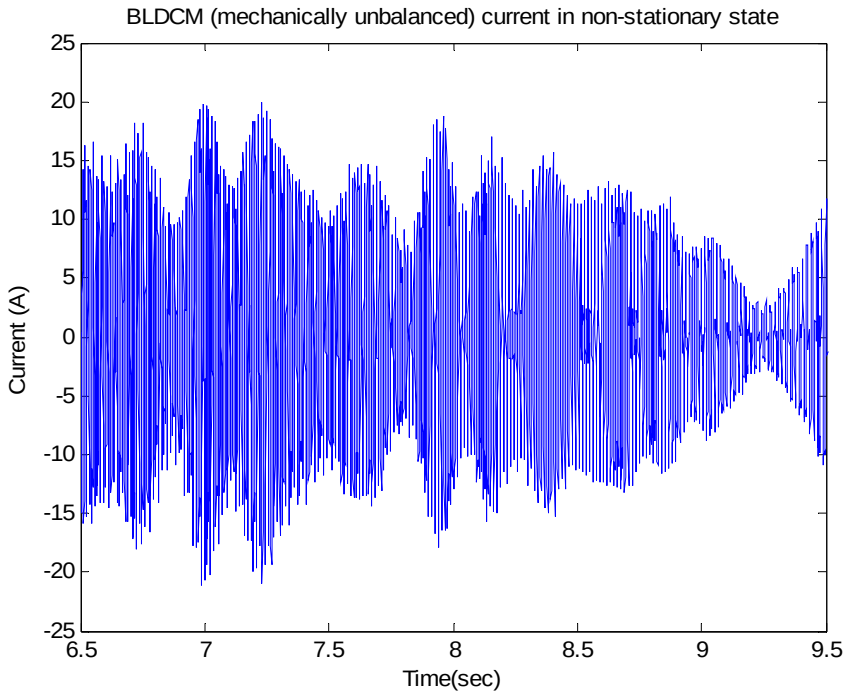

Figure 3.2: Non-stationary stator current in a BLDC motor.

Time-frequency distributions appear as a common choice of research in mechanical engineering. The 1990s has shown an increase in Wigner-Ville analysis in gearbox fault detection. The early application of these methods to gear faults in particular began with the work of Forrester [42-44]. He applied the Wigner-Ville distribution (WVD) to time domain averaged vibration signals of a helicopter gearbox and showed that different faults such as a tooth crack can be detected in the WVD contour plot. McFadden and Wang [45-47] also apply the normal WVD and the weighted version of the WVD to gear failure to improve the detection capability of the

method. In [48] Staszewski, Worden, and Tomlinson apply the wavelet transformation (WT) and the WVD to detect a broken tooth in a spur gear operating under non-stationary conditions. Statistics and neural networks are then used for classification of the fault condition. Besides the Wigner-Ville distribution, several other time-frequency distributions have been tried for diagnostics of rotating machinery. Several more similar applications of time-frequency distributions have been used for condition monitoring have been reported in [49-51].

3.3.2 Non-Stationary Signal Analysis in Electrical Signal Based Diagnostics

There has been little research in the area of fault diagnostics of motors operating under non-stationary conditions and has been limited to induction motor applications. In [52], Yazici and Kliman apply the Short Time Fourier Transform (STFT) to extract (preprocess) frequencies relevant to detecting broken bar and bearing defects, from the induction motor stator current. The extracted features are segmented into constant operating modes of the motor using a probabilistic method (Figure 3.3). The samples from each mode are then statistically analyzed to determine the fault. However, this algorithm is based on the assumption that the change in speed and load occur slowly and there are sufficient intervals of time where the motor can be assumed to operate in a stationary condition. This is common in applications such as rolling steel mills and the cement industry.

Another approach to a similar application, through the use of wavelets, is presented in [53]. Here, a residual is calculated by subtracting the output of a multi-step ahead neuro-predictor from the actual current signal. The neuro-predictor is developed using recurrent dynamic neural networks and predicts ahead in time, the stator current of

a healthy machine. A wavelet packet transform algorithm is then used to separate the different harmonics from the residual signal and to compute the fault indicators (Figure 3.4).

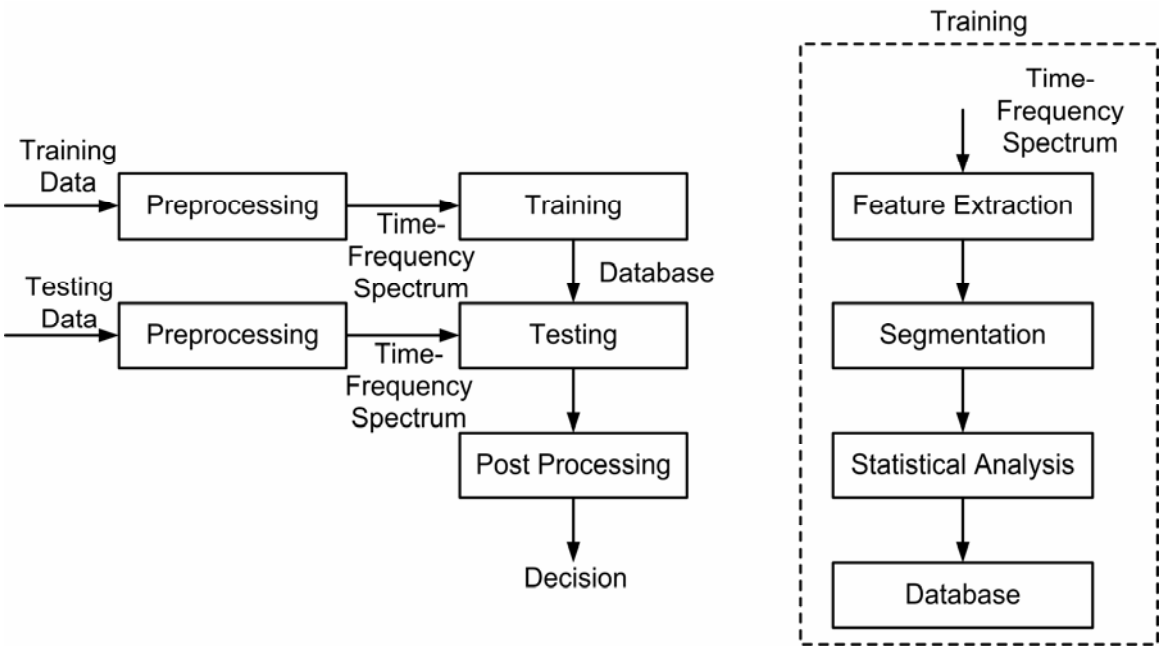

Figure 3.3: STFT-based fault diagnostics scheme for induction motor diagnostics.

Rather than use artificial neural networks, some researchers apply the electrical models of induction motors to calculate the residual. In [54], the researchers use a Park model of the squirrel cage induction drive to predict the behavior of a healthy motor. A residual is again calculated by subtracting the output of the Park model from the actual stator current. Wavelets are then used to process the residual. Thresholding of wavelet coefficients that are sensitive to motor faults allows detection of rotor and stator faults. The authors claim that this algorithm is more sensitive to stator faults than rotor faults, as rotor defects produce small changes in the stator current when compared to stator defects.

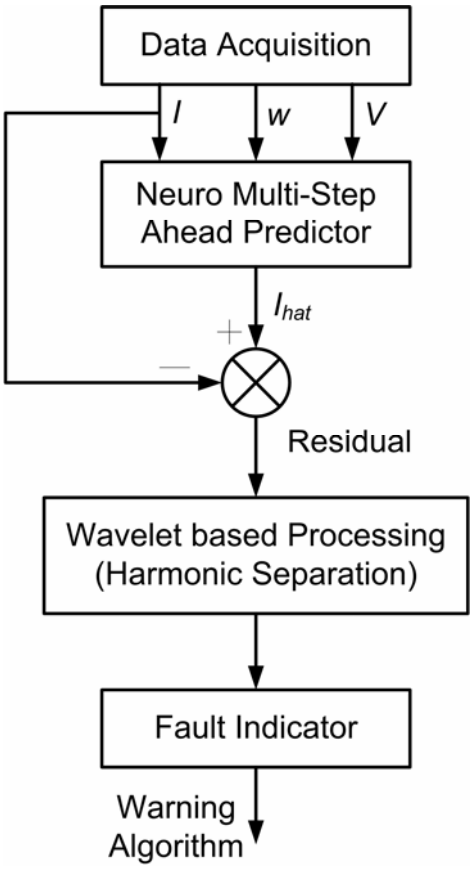

Figure 3.4: STFT-based fault detection algorithm for induction motor diagnostics.

Another area where non-stationary signal analysis has been attempted is in the diagnosis of machine faults from the starting current transients in induction motors. This enables the detection of faults under no load condition. In [55], Burnett et al. detect bearing faults by using discrete wavelet transforms and time-frequency distributions to analyze the starting current transient of an induction motor. The frequency sub-bands for pre-fault and post-fault conditions are compared to identify the effects of bearing resonant frequencies as the motor starts. Recently, time-frequency distributions are also being used for non-stationary load fault detection in induction motors [56]. Eren and Devaney, and Douglas et al. also use a similar method to detect broken rotor bars in

induction motors [57, 58]. However, none of these methods attempt to diagnose faults in applications where the motor is continuously in a non-stationary stage or where assumptions of local or slow stationarity may be questionable and unrealistic.

3.4 Conclusions

Various current-based detection techniques available to detect rotor faults in electric motors operating in transient (non-stationary) operating conditions have been reviewed. Finally, techniques available in the mechanical engineering area to detect non-stationary fault signals have also been discussed setting the stage for methods proposed in this research.

The next chapter describes the first contributions of this research. The effect of various rotor defects on the operation of a BLDC motor is studied experimentally and analyzed in Chapter 4.

CHAPTER 4

ANALYSIS OF ROTOR FAULTS IN BLDC MOTORS OPERATING AT CONSTANT SPEED

The objective of this chapter is to experimentally characterize the effects of potential BLDC motor rotor faults on the motor terminal quantities such as voltage and current. The effects of unbalanced and pulsating loads on the ability to detect rotor faults from characteristic fault frequencies are also studied experimentally. All experiments are conducted in **steady-state** conditions.

4.1 Experimental Arrangement

The experimental arrangement consists of a six-pole, 12 V, 1 kW BLDC motor with surface mount magnets coupled to a dynamometer load. The BLDC motor is driven by an inverter that features an integrated current control loop and provides the electronic commutation necessary to operate the BLDC motor. The inverter is supplied from a 12 V lead-acid deep cycle marine battery. Hall sensors mounted on the rotor shaft provide position control feedback information to the drive. An analog speed controller designed in the lab is added to the drive system to smooth out speed fluctuations and to provide speed control (Appendix A). The circuit schematic of the analog speed controller and its functionality is provided in Appendix A. The block diagram of the BLDC drive system is presented in Figure 4.1.

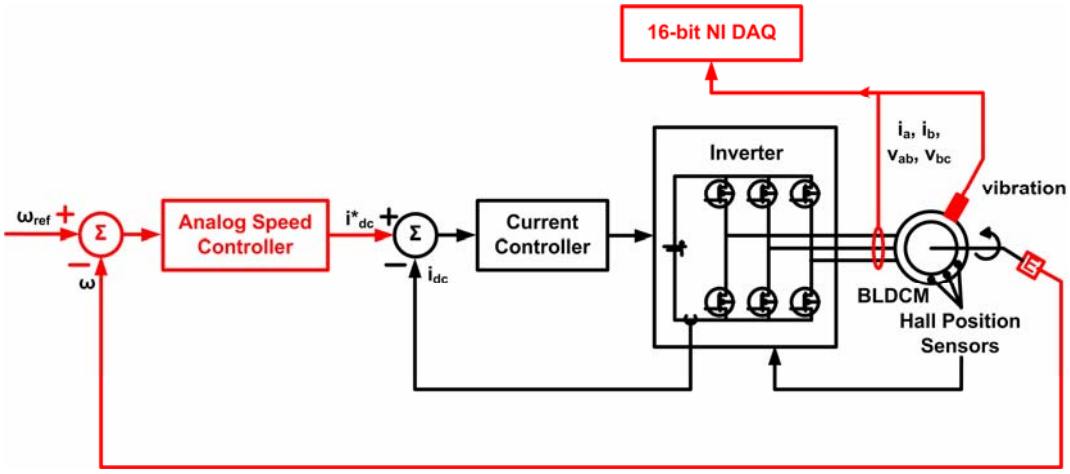

Figure 4.1: Block diagram of BLDC motor control system.

A picture of the experimental arrangement is shown in Figure 4.2. The dynamometer used is an 115V, 1/15 hp DC motor operated as a generator. The dynamometer is coupled to the BLDC motor using a backlash free coupling. The coupled motors are bolted onto a steel base plate that is firmly clamped to the mount. The speed is sensed using a 1000 ppr A-B 1305 optical encoder manufactured by Allen Bradley, Inc. A Wilcoxon Research Model 793 accelerometer with a sensitivity of 100mV/G accelerometer is mounted on the base to sense the vibrations. Hall-Effect sensors are used to sense two line currents and two line-to-line voltages in the BLDC motor. The sensed voltages and currents are acquired through a National Instruments data acquisition system. All data are sampled at a rate of 10 kHz and the data is recorded for 20 seconds to obtain a FFT frequency resolution of 0.05 Hz. All frequencies above 2 kHz are filtered using an eighth-order elliptic low pass anti-aliasing filter prior to the data acquisition. The BLDC motor is operated at two constant speeds: 1800 rpm and 1200 rpm. Experiments are conducted for various load conditions ranging from light load (30% full load) to full load.

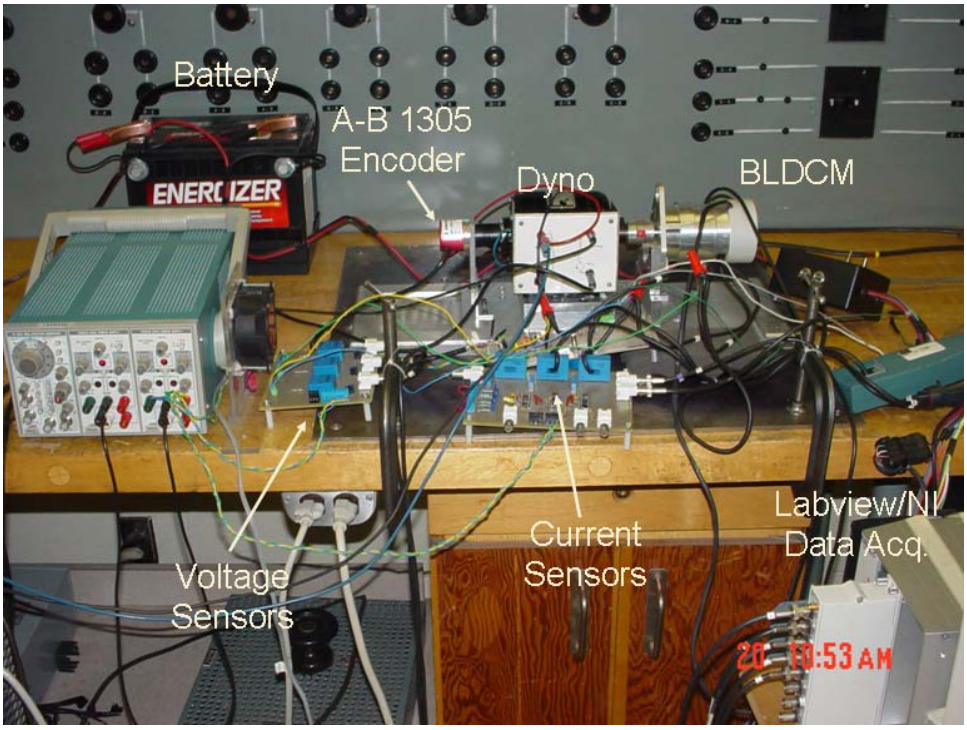

Figure 4.2: BLDC motor - DC generator test rig.

4.2 Dynamic Eccentricity

In dynamic eccentricity, the centre of the rotor is not at the centre of the stator and the position of minimum air gap rotates with the rotor. An actual dynamic eccentricity is implemented in the laboratory [55]. One end of the rotor is first removed from the bearing. This end is selected as the one opposite to the end that houses the Hall position sensors. The end of the rotor housing the Hall sensors is not disturbed. In a machine shop, material is removed from one side of the rotor shaft at the non-sensor end of the motor and the rotor is then placed back onto the bearing. Shims are now inserted between the bearing and the shaft on the side opposite to where the material was removed as shown in Figure 4.3, thus pushing the center of rotation of the rotor away from the center of the stator. The nominal length of the air gap is 0.75 mm and the rotor is shifted

by approximately 0.25 mm (32% of nominal air-gap length) from its center by inserting a steel shim of thickness 0.001 inches (~ 0.25 mm). The defect induced in this manner represents a realistic dynamic eccentricity fault that can occur during normal motor operation.

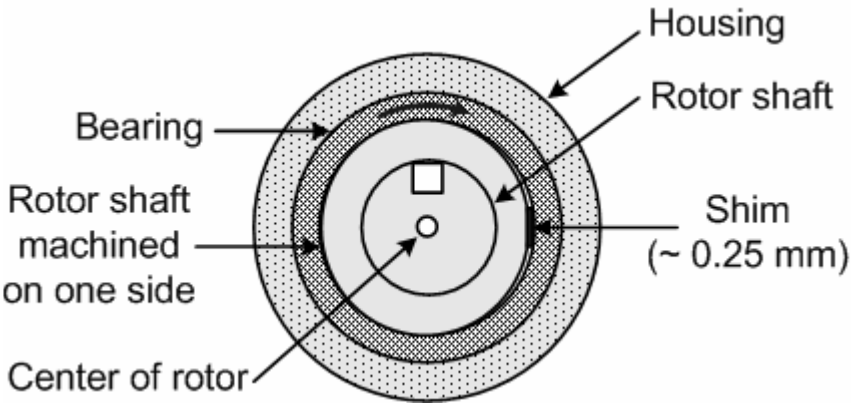

Figure 4.3: Experimental implementation of dynamic eccentricity.

For a six-pole BLDC motor, the rotor fault frequencies occur at 1/3rd, 2/3rd, 4/3rd, and 5/3rd times the fundamental frequency, as computed from (3.10). The experimental results for the light load (30% full load) and the full load cases are presented in Tables 4.1 and 4.2 respectively. This instrumentation accuracy is calculated from the individual sensor inaccuracies: Hall sensor accuracy = $\pm$ 0.9%; Sensor electronics and cable drift accuracy = $\pm$ 5%; Data acquisition and calibration accuracy = $\pm$ 2.5%. The total accuracy/error of the measurements is approximately the product of these individual accuracies and is about $\pm$ 10%. Under light load conditions in Table 4.1, the magnitude of the 2/3rd and the 4/3rd harmonics in the current spectrum of a faulty motor increases by 585% and 229% respectively over that of a good motor. Under full load conditions in Table 4.2, the magnitude of the 2/3rd harmonic in the current spectrum of the faulty motor

increases by 286% over that of a good motor operated under the same full load conditions. However, the magnitude of the 4/3rd harmonic changes only by 31% under fully loaded conditions. The reason for this different behavior under full load condition is that the motor is now more rigidly coupled to the load than it is under low load conditions. Hence, the air-gap fluctuation because of the dynamic eccentricity is less pronounced in full load condition, as compared to a light load condition.

Under light load conditions (Table 4.1), the magnitude of the 1/3rd and 5/3rd harmonics of a faulty motor decreases by 48% and 46% respectively when compared to that of a good motor under similar load conditions. However, the large magnitude of the 1/3rd and the 5/3rd harmonics (238 mA each) in a good motor operating under light load condition indicates that these harmonics are not caused by the dynamic eccentricity, but possibly because of other factors such as the coupling alignment. The same phenomenon is seen under full load conditions too (Table 4.2), where the magnitude of the 1/3rd and the 5/3rd harmonic are 306 mA and 310 mA respectively. It will indeed be demonstrated in Chapter 5, that these harmonics are significantly affected by the motor alignment.

Figure 4.4 shows a portion of the current spectrum for both the normal and the faulty cases (dynamic eccentricity) under full load conditions. The increase in the 2/3rd and 4/3rd harmonics is clearly visible in the case of the BLDC motor with dynamic eccentricity, just as predicted theoretically. A similar change is also noticed in the stator voltage spectrum of Figure 4.5. However, as the magnitude of the fault harmonic in the voltage spectrum is only a few milli-volts, it cannot be used as a reliable indicator to detect dynamic eccentricity.

Table 4.1: Light load case: Harmonic amplitudes of stator current spectrum – dynamic eccentricity (Measurement Error = ± 10%)

Harmonic	**Good Motor (mA)**	**Dynamic Eccentricity (mA)**	**% change**
$1/3^{rd}\ f_e$	238	124	-48
$2/3^{rd}\ f_e$	**40**	**274**	**+585**
$4/3^{rd}\ f_e$	**45**	**148**	**+229**
$5/3^{rd}\ f_e$	238	128	-46

Table 4.2: Full load case: Harmonic amplitudes of stator current spectrum – dynamic eccentricity (Measurement Error = ± 10%)

Harmonic	**Good Motor (mA)**	**Dynamic Eccentricity (mA)**	**% change**
$1/3^{rd}\ f_e$	306	119	-61
$2/3^{rd}\ f_e$	**86**	**332**	**+286**
$4/3^{rd}\ f_e$	58	76	+31
$5/3^{rd}\ f_e$	310	110	-64

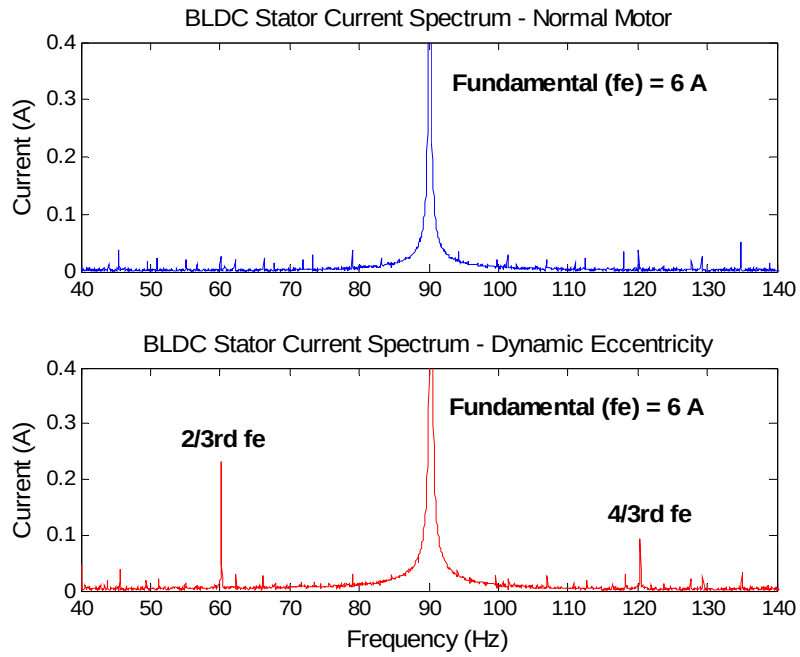

Figure 4.4: Comparison of BLDC motor current spectrum (Dynamic Eccentricity) under light load conditions.

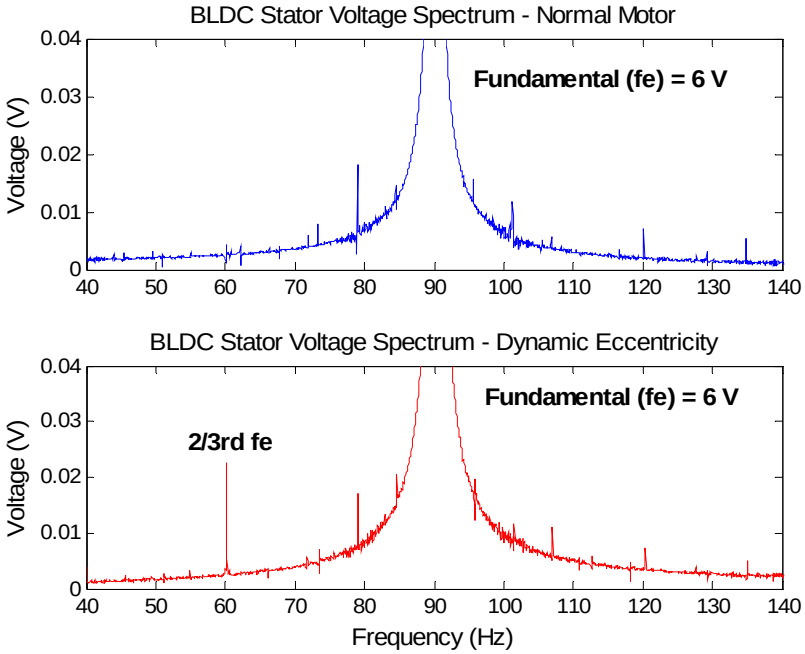

Figure 4.5: Comparison of BLDC motor voltage spectrum (Dynamic Eccentricity) under light load conditions.

4.3 Static Eccentricity

A static eccentricity in an induction motor can be detected from the magnitude of the principal slot harmonics (PSH) in the motor current spectrum [11]. However, in a BLDC motor, no PSH are produced in the current spectrum as the rotor is smooth and comprises of magnets that span an entire pole arc.

Another method that could be used to detect static eccentricity is through the detection of negative sequence current components that are produced because of the motor eccentricity. A static eccentricity results in unequal amounts of the magnet flux passing across the stator coils. This results in an unbalance in the three phase currents, which should theoretically result in a negative sequence current. However, in a permanent magnet motor such as the BLDC motor, the magnet behaves as air, the relative permeability of a magnet (μ_r = 1.09) being almost equal to that of air (μ_r = 1). Therefore, permanent magnet machines effectively have large air gaps. Hence, any physical shift an eccentricity may cause in the air-gap structure only has a small, even negligible effect on the flux distribution. This is verified through simulations, where the static eccentricity is parametrically solved using Maxwell 2D and a transient simulation of the complete BLDC motor drive (with only the current control loop) is carried out in MATLAB to observe any change in the current spectrum. Simulation results are presented in Table 4.3. Only a miniscule negative sequence current is noticed, which is not sufficient to act as an indicator to detect static eccentricity. The same behavior is also noticed in the positive sequence component of the 5^{th} harmonic and in the negative sequence component of the 7^{th} harmonic, which are also a resultant of the unbalance. Hence, it is concluded that detection of static eccentricity in BLDC motors is difficult if not

impossible, and all future eccentricity-related work in this research is limited to dynamic eccentricity.

Table 4.3: Effect of Static Eccentricity on the motor current spectrum of a BLDC motor from MATLAB simulations

	Stator Current (A)		**Stator Voltage (V)**	
Harmonic	**Normal Motor**	**Static Eccentricity**	**Normal (V)**	**Static Eccentricity (V)**
Fundamental	22.857	22.859	2.47	2.48
Positive Seq.	22.857	22.857	2.47	2.48
Negative Seq.	0.0052	0.0028	0.001	0.0028
5^{th} Harmonic	4.575	4.570	0.051	0.050
Positive Seq.	0.0048	0.0025	0.0035	0.0030
Negative Seq.	4.575	4.570	0.048	0.052
7^{th} Harmonic	3.264	3.268	0.107	0.1217
Positive Seq.	3.264	3.264	0.1146	0.1217
Negative Seq.	0.005	0.003	0.006	0.0035

4.4 Damaged Rotor Magnet Fault

The broken magnet defect is obtained by chipping off a part of the magnet on one pole of the BLDC machine, as shown in Figure 4.6. This artificial damage is also representative of a local demagnetization of the magnet. A damaged magnet causes an asymmetric flux distribution, which generates characteristic harmonics in the current

spectrum. The fault frequencies for a six-pole BLDC motor are the same as in the case of a dynamic eccentricity, namely $1/3^{rd}$, $2/3^{rd}$, $4/3^{rd}$, and $5/3^{rd}$ of the fundamental frequency.

Experimental results are provided in Tables 4.4 and 4.5 for the light (30% full load) and full load cases at an operating speed of 1800 rpm. The measurement accuracy is again about $\pm$ 10%. Under light load conditions in Table 4.4, the magnitude of the $2/3^{rd}$ and the $4/3^{rd}$ harmonics in the current spectrum of a faulty motor increases by 64% and 883% respectively over that of a good motor with undamaged rotor magnets. Under full load conditions in Table 4.5, the magnitude of the $2/3^{rd}$ and the $4/3^{rd}$ harmonics in the current spectrum of the faulty motor increases by 176% and 101% respectively, over that of a good motor operated under the same full load conditions. This large change in the fault harmonics can be used to detect a defective motor. However, the magnitude of the $1/3^{rd}$ and $5/3^{rd}$ harmonics do not change significantly, as these harmonics are more affected by the motor alignment rather than the rotor defect.

Figure 4.6: Broken magnet defect.

Table 4.4: Light load case: Harmonic amplitudes of stator current spectrum – damaged magnet (Measurement Error = ± 10%)

Harmonic	**Good Motor (mA)**	**Damaged Magnet (mA)**	**% change**
$1/3^{rd}$ f_e	193	238	+23
$2/3^{rd}$ f_e	**86**	**141**	**+64**
$4/3^{rd}$ f_e	**12**	**118**	**+883**
$5/3^{rd}$ f_e	197	242	+22

Table 4.5: Full load case: Harmonic amplitudes of stator current spectrum – damaged magnet (Measurement Error = ± 10%)

Harmonic	**Good Motor (mA)**	**Damaged Magnet (mA)**	**% change**
$1/3^{rd}$ f_e	196	202	+3
$2/3^{rd}$ f_e	**88**	**243**	**+176**
$4/3^{rd}$ f_e	**82**	**165**	**+101**
$5/3^{rd}$ f_e	203	204	0

4.5 Effect of Unbalanced Rotor

An unbalanced rotor is implemented by mounting a slotted disk on the shaft of the motor (Figure 4.7). A bolt can be positioned at any slot on the disk. As the unbalanced disk rotates, the bolt pulls outward as a result of the centrifugal force. The rotor is therefore being pulled continuously outward with a force that is dictated by both the mass of the bolt as well as the position of the bolt on the disk. Such an unbalanced disk causes slight dynamic eccentricity besides vibration and pulsating torques. The bolt is moved from the inner most point of the disk towards the outermost point on the radius of the disk in three discrete steps and the results are shown in Figure 4.8, where pos 1-3 represent the position of the bolt on the disk with pos 3 being the outermost position. The amplitude is normalized as a percentage of the fundamental. A clear increase in the principal sidebands ($2/3^{rd}$ and $4/3^{rd}$ fundamental frequency) is seen. This shows that a mechanically unbalanced rotor can be detected by monitoring the principal sideband frequencies that occur around the fundamental frequency.

4.6 Effect of Pulsating Load

The effect of a pulsating load torque is similar to the one encountered in applications such as reciprocating compressors. The frequencies in the BLDC stator current that are affected by such a pulsating load are given by

$$f_{vth} = f_e \pm f_r, \tag{4.1}$$

where f_{vth} is the harmonic frequency as a result of the pulsating load, f_e is the fundamental frequency, and f_r is the mechanical rotor frequency.

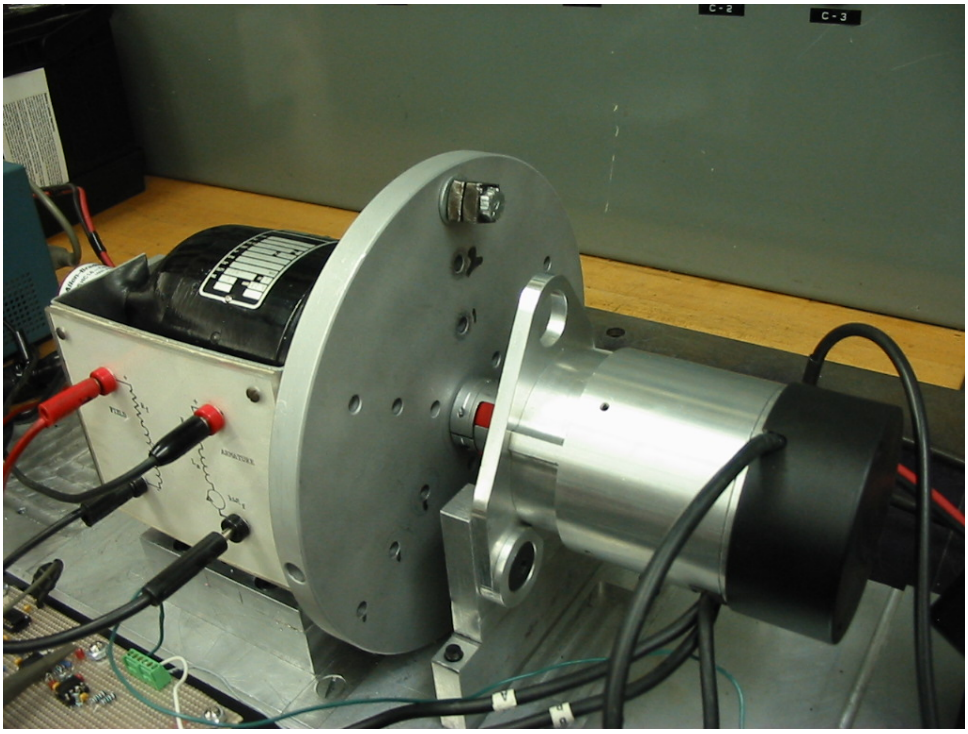

Figure 4.7: Unbalanced disk experiment.

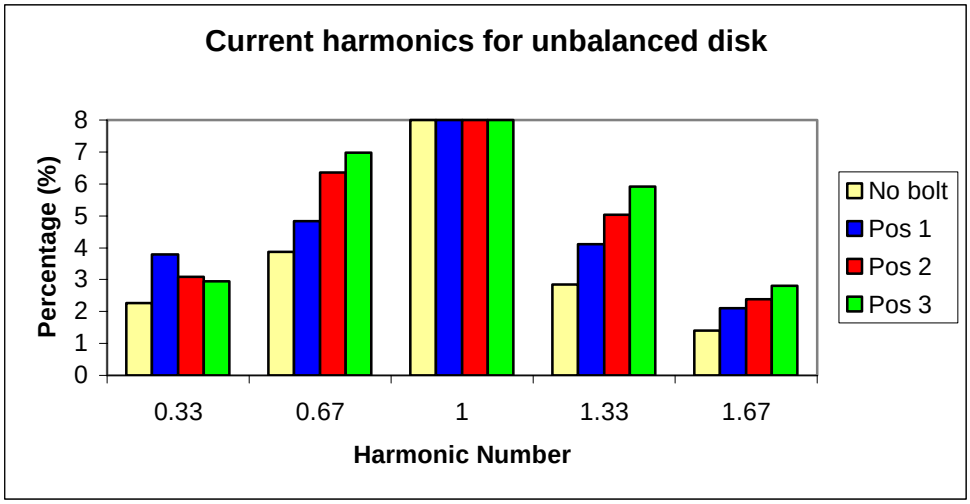

Figure 4.8: Fault harmonics in a unbalanced rotor system.

The frequencies in (4.1) happen to be the same frequencies that are also affected by dynamic eccentricities and broken magnets. A load torque varying at the rotor speed is implemented by modifying the dynamometer's resistive load. This is done by adding a resistor switched at the rotor frequency (30 Hz in this experiment) as shown in Figure 4.9. There are several ways a pulsating dyno load can be quantified. It can be described in terms of the load torque ripple or in percentage of the pulsating power. The latter approach is used here. It is assumed that V is the terminal dyno voltage, R_{fload} is a fixed resistance, and R_{pload} is the pulsating resistor switching at 50% duty cycle. The knowledge of the dyno parameters such as the armature resistance and the field resistance are needed only to convert the electric load power applied to the dyno into a mechanical torque load seen by the BLDC motor. Hence, these dyno parameters are not used, as the pulsating load applied to the BLDC motor is just quantified based on the dyno's electrical loading. A pulsed power of 10% of the total DC power is used in this experiment. A detailed derivation for quantifying the pulsating load is provided in Appendix B.

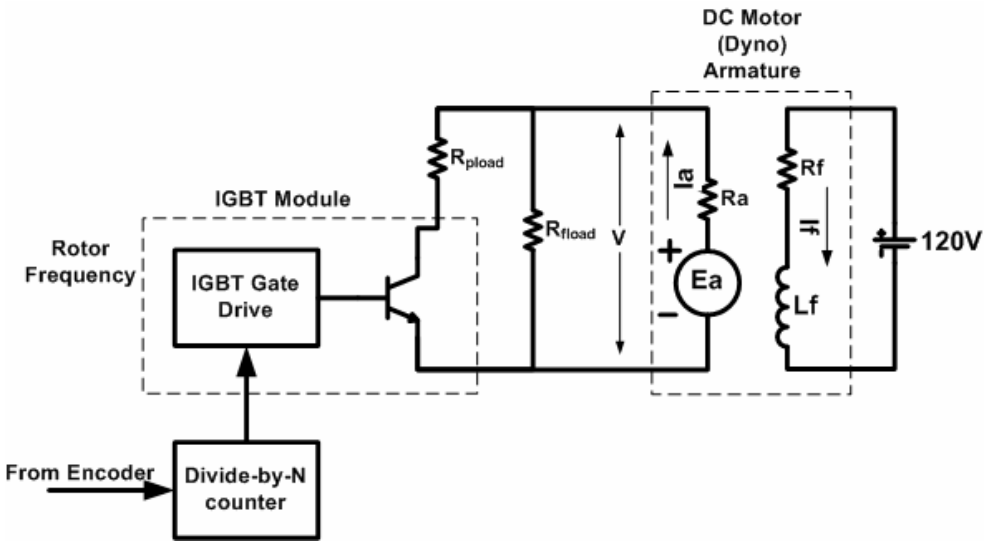

Figure 4.9: Pulsating load torque generator.

The experimental results are provided in Tables 4.6 and 4.7 for the light (30% full load) and full load cases at an operating speed of 1800 rpm, with a measurement accuracy of about $\pm$ 10%. In this experiment, R_{pload} is switched at the rotor frequency. This provides a pulsating load, with the load torque pulsating at the BLDC motor's rotor frequency. From (4.1), the only frequency components created by a load at pulsating at the rotor frequency are the 2/3rd and the 4/3rd fundamental frequency components, as

$$f_r = \frac{f_e}{3}. \tag{4.2}$$

Under light load conditions in Table 4.5, the magnitude of the 2/3rd and the 4/3rd harmonics in the current spectrum of a BLDC motor with pulsating load torque increases by 707% and 5308% respectively over that of a BLDC motor with no torque pulsations. Similarly, under full load conditions in Table 4.7, the magnitude of the 2/3rd and the 4/3rd harmonics in the current spectrum of a BLDC motor with pulsating load torque increases by 536% and 533% respectively, over that of a good motor operated under the same full load conditions. The magnitude of the 1/3rd and the 5/3rd harmonics do not change significantly, as they are not affected. This large change in these frequency components has the potential to mask other rotor fault signatures that occur at the same frequency. For example, under full conditions, the magnitude of the 2/3rd and the 4/3rd harmonics in the current spectrum of a BLDC motor with pulsating load torque are 560 mA and 516 mA respectively (Table 4.7). This magnitude is large compared to the magnitude of the same 2/3rd and the 4/3rd harmonics in the current spectrum of a BLDC motor with dynamic eccentricity, which is measured to be 332 mA and 76 mA respectively (Table 4.2).

Table 4.6: Light load case: Harmonic amplitudes of stator current spectrum – load pulsating at rotor frequency (Measurement Error = ± 10%)

Harmonic	**Good Motor (mA)**	**Pulsating Load (mA)**	**% change**
$1/3^{rd}\ f_e$	193	225	+17
$2/3^{rd}\ f_e$	**86**	**694**	**+707**
$4/3^{rd}\ f_e$	**12**	**649**	**+5308**
$5/3^{rd}\ f_e$	197	228	+16

Table 4.7: Full load case: Harmonic amplitudes of stator current spectrum – load pulsating at rotor frequency (Measurement Error = ± 10%)

Harmonic	**Good Motor (mA)**	**Pulsating Load (mA)**	**% change**
$1/3^{rd}\ f_e$	196	191	-3
$2/3^{rd}\ f_e$	**88**	**560**	**+536**
$4/3^{rd}\ f_e$	**82**	**519**	**+533**
$5/3^{rd}\ f_e$	203	210	+3

4.7 Synthesis of Experimental Results

The results obtained under a light load (30% full load) condition and a full load condition for the dynamic eccentricity, for the damaged magnet, and for the effect of a load torque varying at rotor frequency, are all summarized in Tables 4.8 and 4.9, respectively. These faults are also compared with a BLDC motor having a normal rotor. In the Tables 4.8 and 4.9, the magnitude of the harmonics is normalized to the respective harmonic magnitude of a good motor.

Table 4.8 (Light load case) shows that the two stator current sidebands at $2/3^{rd}$ and $4/3^{rd}$ the fundamental frequency changes by 6.5 and 3.2 times respectively in a dynamically eccentric motor when compared to a good motor. The same sidebands increase by 1.6 and 9.1 times in the case of a damaged magnet fault, again when compared to a good motor. These changes in magnitudes of these sidebands are significant when compared to those of a normal motor. A similar change is also seen under full load conditions in Table 4.9. Thus, the rotor defects in a BLDC motor can be distinctly identified.

However, a load torque varying at the rotor frequency also affects the same sidebands and thus has the potential to mask the rotor defects. For example, the results in Table 4.8 show that that a load pulsating at the rotor frequency can produce a $4/3^{rd}$ fault harmonic that is 46 times larger than that of a motor with no load pulsation. This increase is more than 5 times the increase in the same harmonic when the rotor defect is a damaged magnet. Hence, pulsating loads can produce signatures that can be mistaken for real rotor faults.

Table 4.8: Light load case: Normalized harmonic amplitudes of total (abc-frame) stator current (Individual Measurement Error = $\pm$ 10%)*

Harm. number	**Normal Rotor**	**Dynamic Eccentricity**	**Broken Magnet**	**Pulsating Torque**
$1/3^{rd}$ f_e	1.0	0.5	1.1	1.0
$2/3^{rd}$ f_e	1.0	**6.5**	1.6	**7.0**
$4/3^{rd}$ f_e	1.0	**3.2**	**9.1**	**46.0**
$5/3^{rd}$ f_e	1.0	0.5	1.1	1.0

Table 4.9: Full load case: Normalized harmonic amplitudes of total (abc-frame) stator current (Individual Measurement Error = $\pm$ 10%)*

Harm. number	**Normal Rotor**	**Dynamic Eccentricity**	**Broken Magnet**	**Pulsating Torque**
$1/3^{rd}$ f_e	1.0	0.4	0.9	1.0
$2/3^{rd}$ f_e	1.0	**3.5**	**2.5**	**6.2**
$4/3^{rd}$ f_e	1.0	1.2	**1.8**	**6.2**
$5/3^{rd}$ f_e	1.0	0.3	0.9	1.0

*Normalized harmonic amplitudes in bold denote significant change in harmonic amplitudes even if individual measurement errors are included.

4.8 Conclusions

The effect of various potential rotor faults on the motor current spectrum of a BLDC machine has been investigated through experiments. Experimental results show that the rotor defects affect mainly the two sidebands at $2/3^{rd}$ and $4/3^{rd}$ of the fundamental frequency. The two smaller sidebands at $1/3^{rd}$ and $5/3^{rd}$ the fundamental frequency are affected to a lesser extent and are influenced more by the alignment of the experimental arrangement than the actual rotor fault. The misalignment defect is further investigated experimentally in Chapter 5 to validate this assertion. The ability to detect rotor conditions such as dynamic eccentricity diminishes in the presence of vibrations and cyclically varying loads as seen in the unbalanced rotor and pulsating load experiments. The measurement accuracy in the experiments is about $\pm$10%. While detailed statistical analysis is not conducted to conclusively determine that motor current signature analysis can be a robust fault detection technique, the experimental results suggest that motor current signature analysis may be applied to the diagnosis of BLDC motor rotor condition, particularly in applications where steady state operation will be encountered. Care must be taken while developing a condition-monitoring scheme, as it is shown experimentally that pulsating loads have the capability to mask rotor fault signatures. The detection of load related faults such as gear and coupling defects in steady state operating conditions is next addressed in Chapter 5.

CHAPTER 5

DETECTION OF LOAD FAULTS IN BLDC MOTORS OPERATING AT CONSTANT SPEED

The objective of this chapter is to diagnose faults in loads coupled to BLDC motors operating at **constant speed**. Two common sources of faults in the load system are gears and couplings. As gear faults are common and critical to the functioning of any electromechanical system, they form the main topic of discussion in this chapter. This chapter investigates in detail the effects on the motor terminal voltage and current of various gear faults, including damaged gear teeth, loss of lubrication, and external debris in the gear train. The most common coupling-related faults are misalignments, and these are briefly discussed toward the end of this chapter.

5.1 Introduction

Gears form an important part of many electro-mechanical systems. In most systems, the gear forms a part of the mechanical load that is coupled to an electrical device, which usually is an electric motor. Several faults can occur in the gear arrangement. Faults in gears can cause discontinuities in production schedules in industries thus lowering productivity. The critical importance of a gear in most systems (for instance in aircraft such as helicopters) has led to the development of gear condition monitoring as an active research area in mechanical engineering for some time. However, most of the diagnostic strategies have focused on vibration analysis, and the monitoring of gear health has not attracted much attention from the electrical engineering community. The different types of commonly used gears and the typical faults that occur

in them, has already been explained in Chapter 2. This chapter proposes an alternative way of detecting faults in gears coupled to BLDC motors by monitoring either the motor current or the voltage. It will be shown that the gear faults create unique spectral components in the voltage and current spectra that can be used to track and detect these faults.

5.2 Detection of Gear Faults Through Current/Voltage - Theory

A gear often consists of a pinion and a driven wheel. When coupled to a motor, the pinion of a reduced speed gear rotates at the speed of the rotor, while the driven wheel rotates at the reduced speed that is set by the ratio of the number of teeth in the driven wheel to the number of teeth in the pinion. Any fault in either the pinion or the driven wheel presents itself as a unique harmonic component in the motor stator current and voltage. This can be explained as follows: A gear defect such as a damaged tooth produces an abnormality in the load torque "seen" by the motor. This abnormality is transferred to the motor current from the load. Depending on the abnormality, unique frequencies can be seen in the current frequency spectrum. The most common mechanism of generation of the fault frequencies is through amplitude modulation (AM).

5.2.1 Amplitude Modulation (AM)

In amplitude modulation or AM, a carrier signal of frequency ω_c is modulated by a signal of frequency ω_m. The resulting amplitude modulated signal has spectral components at frequencies ω_c, $\omega_c + \omega_m$, $\omega_c - \omega_m$. The same theory can also be applied to detect gear faults in the motor current spectrum where the two sidebands around the fundamental (carrier-frequency) represent certain gear faults uniquely. In faults such as scoring, the increase in friction caused by the low level of lubricant, results in a low

frequency modulating signal that resembles a slow sine wave. In a speed reducing gear, this modulating frequency is the frequency of the reduced gear speed. This modulating frequency, ω_m, appears in the motor load torque as slow pulsations. In BLDC motors, the torque produced is directly proportional to the armature current as given by

$$T_L \approx T_{em} = k_T I \,, \tag{5.1}$$

where T_L is the load torque containing the pulsating component, T_{em} is the electromagnetic torque produced by the BLDC motor that is almost equal to the load torque at steady speed conditions, k_T is the motor torque constant, and I is the average BLDC motor current. Hence the pulsating load torque component gets transferred into the BLDC motor current. The BLDC stator current now has a low-frequency signal that modulates the normal current wave that consists of the fundamental and other inverter frequencies. The stator current spectrum thus consists of the fundamental frequency ω_c and the two gear fault sidebands at $\omega_c + \omega_m$ and $\omega_c - \omega_m$.

In other defects such as a local tooth defect, the modulating signal is a periodic impulse train rather than a sine wave. In such and other more complicated gear defects, a graphical rather than a purely mathematical treatment helps in determining the gear fault frequencies. This is explained in detail in the next section.

5.2.2 Determining Gear Fault Frequencies in BLDC Stator Current Through a Graphical Approach

Gear faults such as a single damaged tooth in the driven gear or debris in the lubricant present themselves as a periodic impulse in the load torque whenever the pinion comes in contact with the damaged tooth. These short-duration periodic torque impulses

transfer to the motor current, as illustrated in the waveform *i(t)* in Figure 5.1. The fundamental frequency of the current is amplitude modulated by the impulse to produce a rich set of harmonic components around the fundamental. The occurrence of unique frequencies in the current spectrum resulting from a defective gear can be explained through a graphical approach developed for analyzing vibration spectra in [60, 61] and adapted here to the stator current and voltage. In Figure 5.1, the fault exists for a time τ and is repeated every T seconds as the driven gear completes one rotation. The current *i(t)* is the *amplitude modulation* of the normal wave $g_1(t)$ and the short-duration impulse $g_2(t)$. $G_1(f)$ and $G_2(f)$ are the Fourier transforms of $g_1(t)$ and $g_2(t)$, respectively. Since the modulating signal $g_2(t)$ is an impulse, the corresponding Fourier transform $G_2(f)$ is a series of discrete harmonics occurring at multiples of 1/T. It is known from the convolution theorem [62] that

$$i(t) = g_1(t).g_2(t) \xleftrightarrow{F} I(f) = G_1(f) * G_2(f), \tag{5.2}$$

The graphical superposition of $G_1(f)$ and $G_2(f)$ results in the Fourier transform of the current, *I(f)*, as shown in Figure 5.1, where a rich spectrum of harmonics spaced at $f_o \pm k/T$ ($k = 1, 2, 3, \ldots$) is produced around the fundamental frequency f_o. This derivation can also be applied to the stator voltage.

In other words, a localized fault in the pinion (driving wheel) will produce stator current/voltage harmonics given by

$$\begin{aligned} &f_{pin,h} = f_o \pm k.f_r, \\ &\textit{For local teeth damage: } k = 1, 2, 3, \ldots, \end{aligned} \tag{5.3}$$

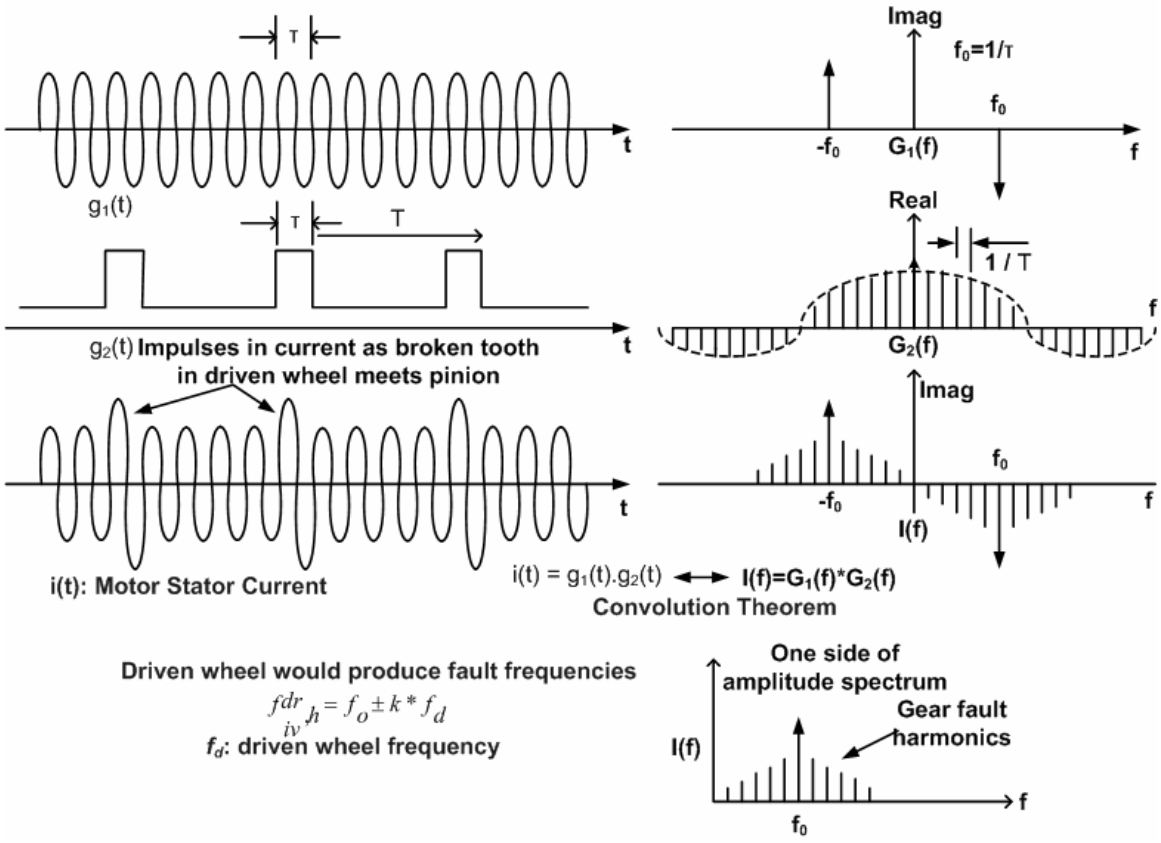

Figure 5.1: Fault harmonic generation in stator current resulting from local tooth damage in gears. (Modified from [39]).

where f_r is the pinion frequency. Similarly, the driven wheel will produce fault frequencies at

$$\begin{aligned} &f_{driw,h} = f_o \pm k.f_d, \\ &\textit{For scoring: } k = 1, \\ &\textit{For debris in gear, local teeth damage: } k = 1, 2, 3,... \end{aligned} \quad , \tag{5.4}$$

where f_d is the driven wheel frequency given by

$$f_d = \frac{f_o}{n.(P/2)}, \tag{5.5}$$

where n is the gear ratio and P is the number of motor poles. Thus, the magnitude and the frequency of the fault harmonics in the current/voltage frequency spectrum are dependent on the type and location of the fault in the gear, which define the modulating wave $g_2(t)$.

5.3 Experimental Setup for Gear Fault Detection

A worm gear system (Figure 5.2) is used in the experiments. The gear consists of a steel worm shaft that drives a 66-tooth plastic worm wheel gear, yielding a speed conversion ratio of 22:1. The worm gear is coupled to a six-pole, 12 V, 1 kW BLDC motor, which is supplied from a three-phase inverter in current control mode. This worm gear system is used in automobile power steering systems (Figure 5.3). In the tests, the load on the gear is its own inertia and no external loading is used. The line-line stator voltage and the stator current are sensed using closed loop hall sensors and the signals are acquired using a 16-bit data acquisition system. The electrical and the mechanical parameters of the experimental system for a typical supply frequency of 180 Hz are

- BLDC motor supply frequency (f_o) = 180 Hz
- Number of motor pole pairs (p) = 3
- Gear ratio (n) = 22:1
- Rotating frequency of the driven wheel (f_d) for a f_o of 180 Hz = 2.73 Hz (calculated using (5.5))
- Number of teeth on the plastic wheel = 66
- Gear meshing frequency = rotating frequency of driven gear X number of teeth on the gear = 180 Hz.

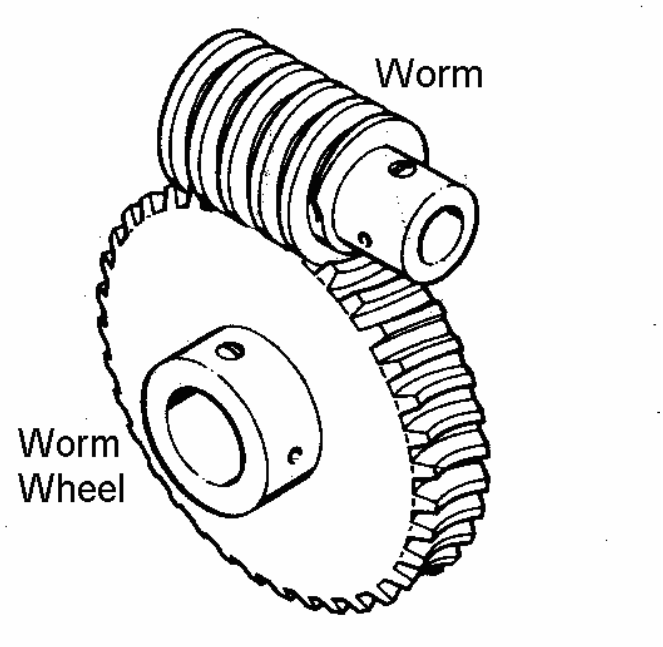

Figure 5.2: Worm gear.

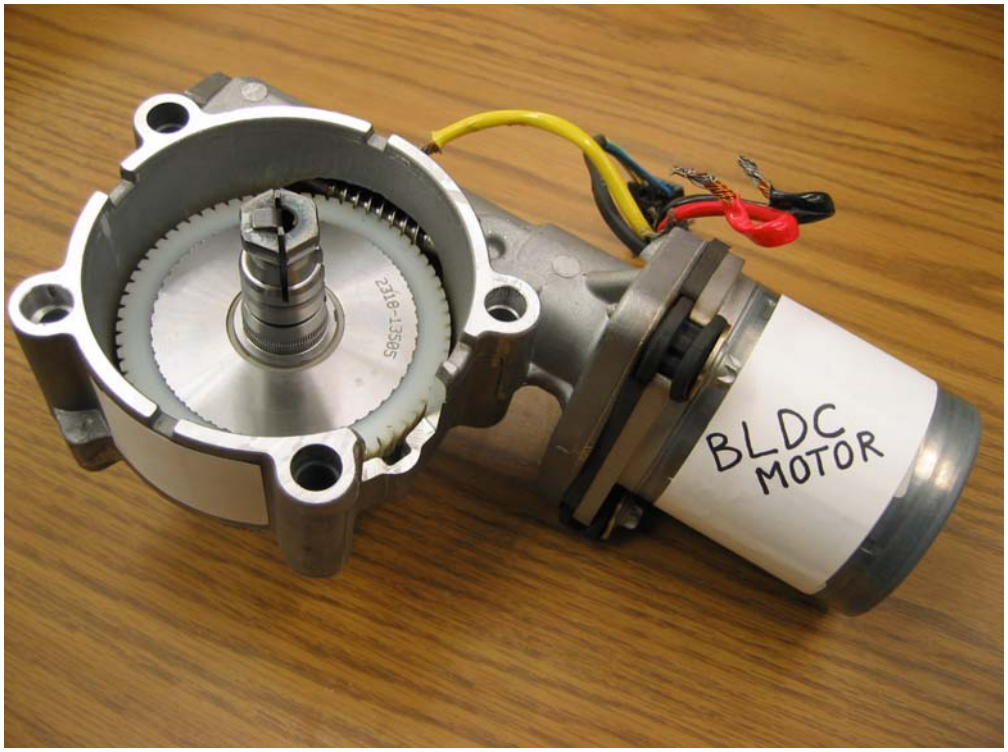

Figure 5.3: Worm gear-BLDC motor assembly.

5.4 Experimental Results for Gear Fault Detection

Experiments are conducted to verify whether faults in gear systems coupled to electromechanical devices such as motors can be detected by monitoring the current in the BLDC motor.

The following types of gear defects are implemented:

i. Damaged tooth (Two teeth, local fault)

ii. Scuffing, Scoring (loss of lubrication)

iii. Debris in lubricant

The gear meshing frequency of this worm gear coincides with the fundamental frequency of the BLDC motor stator current. Hence, this frequency cannot be viewed separately.

5.4.1 Damaged Tooth Fault

A localized damaged tooth fault is implemented by deforming two adjacent teeth on the plastic driven wheel of the worm gear by compressing them with a pair of pliers. Motor current and voltage waveforms are recorded. Whenever the deformed teeth reach the steel worm the BLDC motor experiences a "bump" in its load and since this is a periodic event, the BLDC motor experiences a pulsating load. The modulating frequency component in the AM is thus a periodic pulse as explained in the previous section. The stator current of one phase of the BLDC motor with this defective gear condition is shown in Figure 5.4. Such a pulsating load should in theory give rise to a rich group of harmonics around the fundamental frequency in the current spectrum and spaced at the frequency of rotation of the toothed gear wheel. This is verified by examining the current frequency spectrum in Figure 5.5. The fundamental frequency is not fixed exactly at 180 Hz because of the absence of speed control in the BLDC drive. Two frequency sidebands

at 177.7 Hz and at 183.1 Hz are noticeable in the normal gear current spectrum. This is because of the fact that all practical gear assemblies are non-ideal and exhibit some mild abnormality. The BLDC current spectrum for a defective gear, however, exhibits a rich spectrum of harmonics spaced 2.8 Hz apart. The frequency of 2.8 Hz is the driven wheel frequency f_d obtained from (5.5) for a fundamental frequency (f_o)of 187.2 Hz (Figures 5.4 and 5.5). The corresponding BLDC line-to-line voltage spectrum in Figure 5.6 also shows a rich spectrum of harmonics at the same frequencies that are present in the current spectrum.

5.4.2 Scoring (Insufficient or Loss of Lubrication)

Scoring occurs because of insufficient or loss of lubrication. This defect is implemented for testing by removing the lubricant using soap and water. The BLDC motor-gear combination is then operated with the BLDC motor rotating at a speed of about 3500 rpm. The stator current of one of the phases of the BLDC motor is recorded and is shown in Figure 5.7. The modulating frequency in Figure 5.7 is a low frequency sine wave as explained earlier. The removal of the lubricant increases the friction between the gear wheels and this friction appears as a pulsating load to the BLDC motor. This pulsation is the sinusoidal modulation of the BLDC motor stator current seen in Figure 5.7.

The lower plot of Figure 5.8 shows the BLDC current spectrum after about 10 minutes of operation. The gear is observed to be running hot because of friction. This gear fault is characterized by the two sidebands in the current and voltage spectrums spaced at $f_o \pm f_d$ and their magnitude increases because of friction. The two sidebands in Figure 5.8 occur at 170.9 Hz and 176.1 Hz for a f_o of 173.5 Hz and a f_d of 2.6 Hz

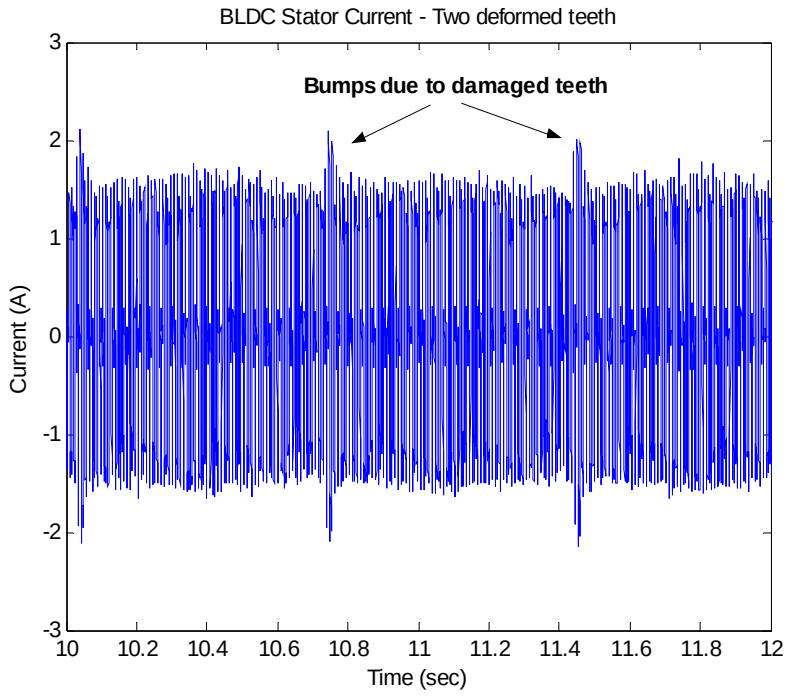

Figure 5.4: Stator current of BLDC motor with two deformed teeth in gear.

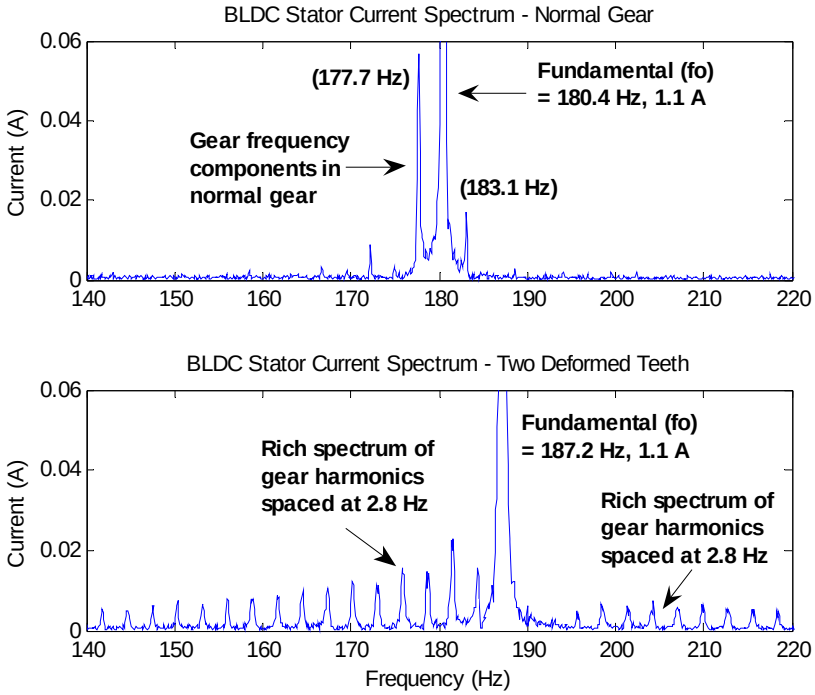

Figure 5.5: BLDC stator current spectrum for the damaged gear teeth case.

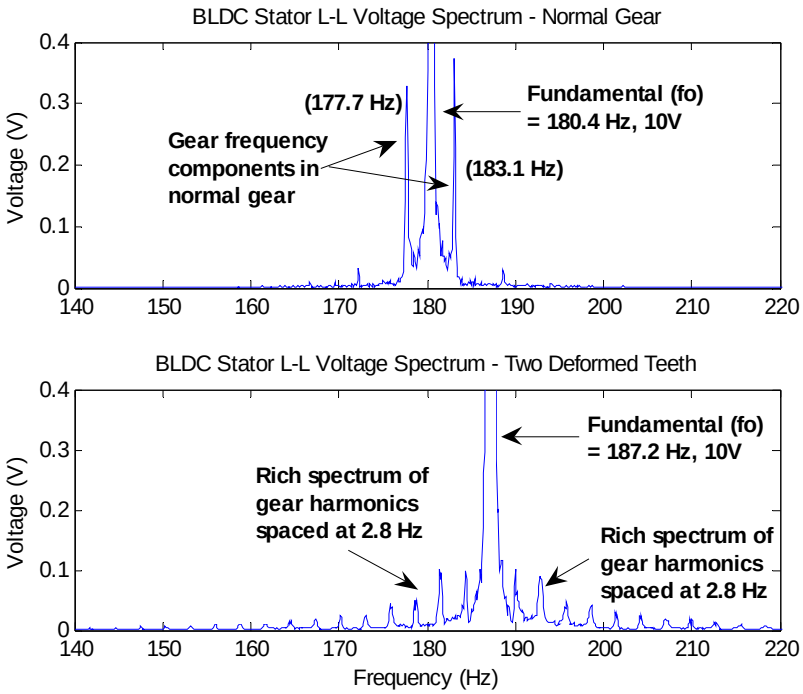

Figure 5.6: BLDC stator line-line voltage spectrum for the damaged gear teeth case.

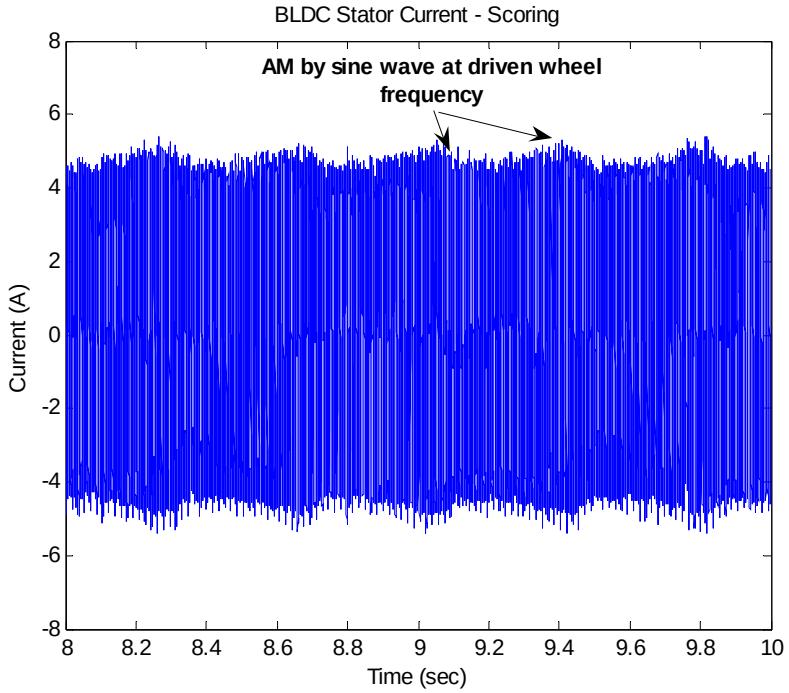

Figure 5.7: BLDC stator current with lubricant removed from gear.

(calculated from (5.5)) and their magnitudes increase to almost 10% of the fundamental. Thus, it can be concluded that the friction associated with the loss of lubrication can be detected by monitoring the gear harmonics around the fundamental. The fundamental itself also increases because the friction represents an increase in the load as the gear heats up with time. The line-line voltage spectrum in Figure 5.9 also shows a clear increase in the gear harmonics at 170.9 Hz and 176.1 Hz, thus indicating that the loss of lubrication in gears can also be detected by monitoring the motor stator voltage.

5.4.3 Debris in Gear Lubricant

Foreign particles or debris such as dust or metal scrap could get trapped inside the gear and possibly lead to gear failure. Debris in the lubricant causes an effect similar to the localized gear tooth damage. The BLDC motor experiences a pulsating load whenever the debris is trapped in between the worm and the wheel. To experimentally evaluate the impact of debris in lubricant, small pieces of soft paper are inserted into the gear while it is running and Figure 5.10 shows the resulting stator current spectrum. A rich spectrum of gear frequencies spaced 2.9 Hz apart appear around the fundamental and appears similar to the case of a localized teeth damage fault (Figure 5.5). The frequency of 2.9 Hz is the driven wheel frequency f_d obtained from (5.5) for a f_o of 190.2 Hz (Figure 5.10). Similar trends also appear in the stator line-line voltage spectrum (Figure 5.11), where the fault frequencies are appear at the exact locations, as in the corresponding BLDC motor current spectra of Figure 5.10.

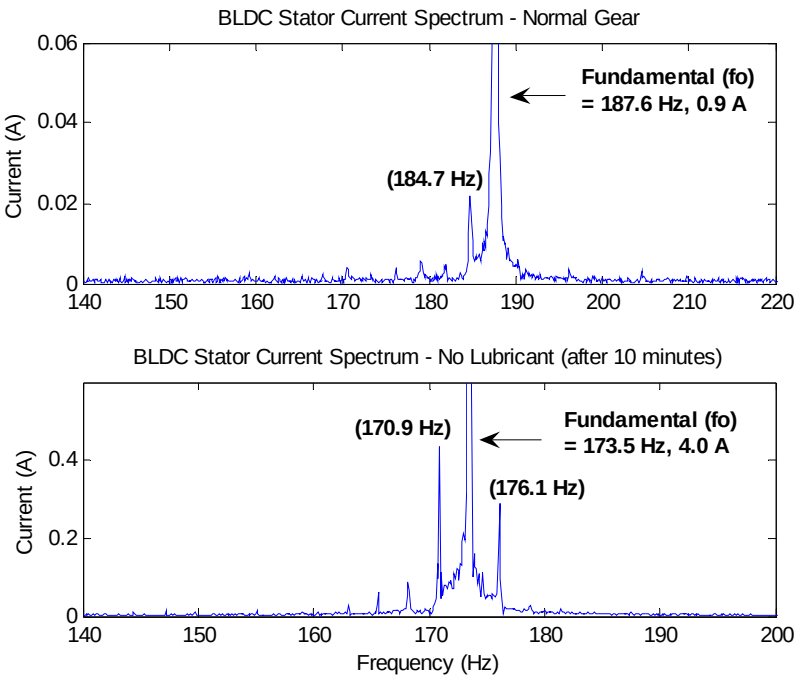

Figure 5.8: BLDC stator current spectrum after 10 minutes of operating with lubricant removed from gear.

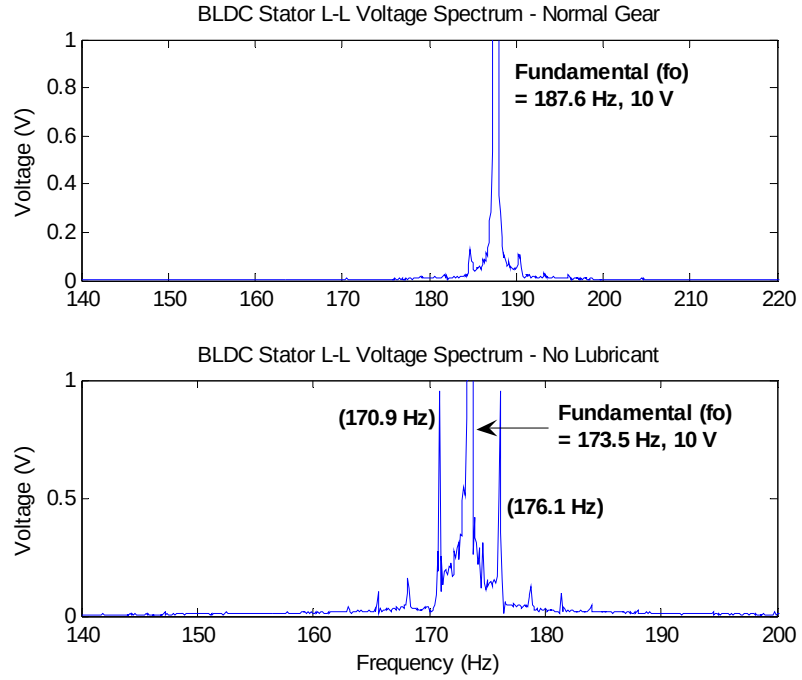

Figure 5.9: BLDC stator line-line voltage spectrum after 10 minutes of operating with lubricant removed from gear.

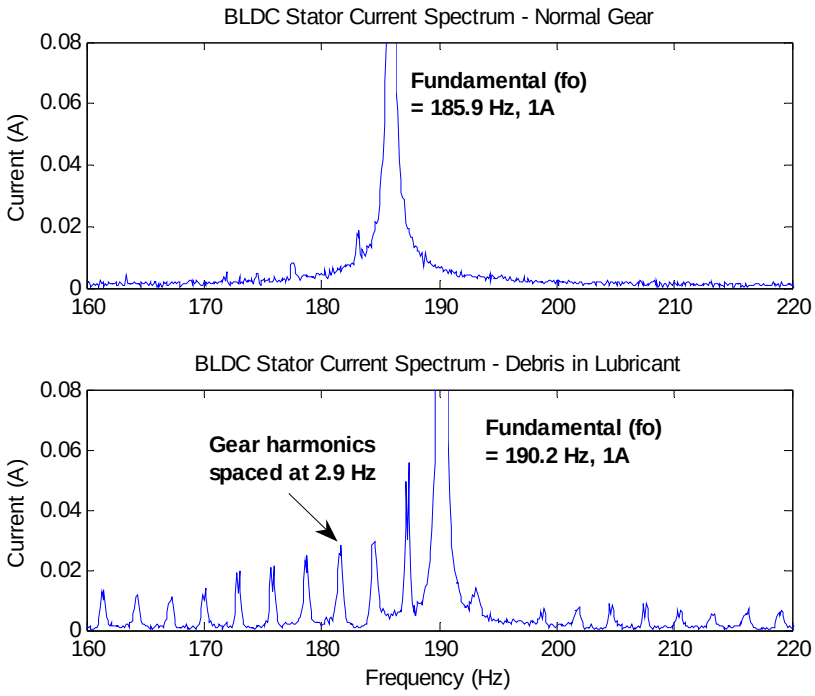

Figure 5.10: BLDC stator current spectrum with debris in lubricant.

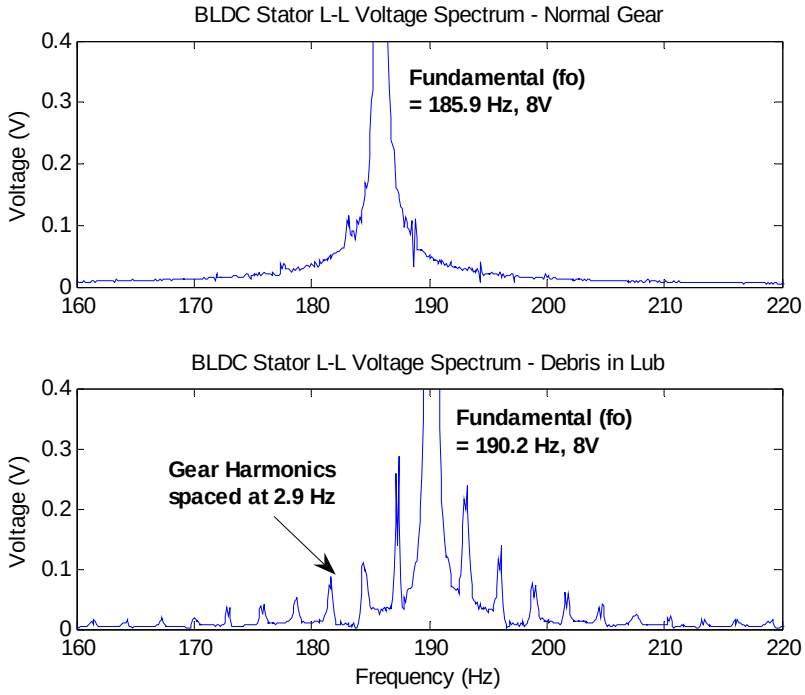

Figure 5.11: BLDC stator line-to-line voltage spectrum with debris in lubricant.

5.5 Simulation Results with Gear Load Model

The effect of a faulty gear on the stator current of a BLDC motor is studied through simulations. The six-pole, 12 V, 1 kW BLDC motor is first modelled using finite-element analysis. The same BLDC motor drive used in the tests is studied through simulations. The magnet flux linkages and machine inductances are obtained through finite element simulations using the Ansoft MAXWELL 2D and RMxprt packages. The finite element analysis is done in two-dimensions because three-dimensional (3D) effects (end windings, etc.) have negligible effect on the problem at hand. Magnet flux linkages and motor inductances are obtained from the finite element simulation using 120 steps for every complete rotor revolution. This information is then used in the form of a lookup table in a MATLAB program to simulate the BLDC motor drive with torque control.

The gear with a local damaged teeth fault is simulated using an impulsive load where the impulse lasts for half a current cycle and occurs at periodic intervals of time. While the experiments are conducted at no load conditions because of the limitations in the laboratory that restrict full load operation, no such restriction exists for simulations. The simulated gear fault operation at 50% full load motor operation is shown in Figure 5.12 where impulses are applied on the load at regular intervals of time (in this case every 0.3 seconds which corresponds to a frequency of 3.33 Hz that was chosen arbitrarily for this study). This represents local gear damage, where one or two teeth are damaged on a gear wheel.

This gear load is simple. The normal load torque applied by a gear is equivalent to a proportional load, where the load torque is proportional to the motor speed. During a gear defect such as a broken tooth, an impulse is created in the load, as the broken tooth

on one gear wheel comes in contact with the second wheel. This is approximately modeled as a load that has an impulse, every 0.3 seconds. The load model is depicted as

$$
\begin{aligned}
&\textit{Normal Load Torque on BLDC motor} \\
&T_{L(\text{due to gear})} = 0.03.\omega_{motor}\ Nm \\
&\\
&\textit{Short Duration Impulsive Load Torque} \\
&\textit{(due to gear defect, when the broken teeth} \\
&\textit{comes in contact with the other gear wheel)}\ , \\
&\textit{every 0.3 seconds for 50 ms} \\
&T_{L(\text{due to gear})} = 0.03.\omega_{motor} + 0.4\ Nm \\
&\\
&\textit{where } \omega_{motor} \textit{ is the mech. speed of the} \\
&\textit{BLDC motor (rad/s)}
\end{aligned}
\tag{5.6}
$$

In Figure 5.12, the top plot shows the mechanical BLDC motor speed. The speed dips, whenever the short duration impulse is felt by the current-controlled BLDC motor. The short impulse appears as an increased load to the motor. The bottom plot in the same figure shows the load torque model that imitates a gear fault.

The stator current spectrum of the simulated BLDC drive is shown in Figure 5.13 which contains a rich spread of harmonics around the fundamental component of current. The motor has a steady state operating speed of 350 rpm. The gear fault harmonics visible in the stator current spectrum are spaced 3.33 Hz apart, as the impulsive load representing the contact of the damaged gear tooth occurs every 0.3 seconds. It is thus demonstrated that such a pulsating load model adequately represents various gear defects and that most gear defects could therefore be detected by monitoring electrical quantities such as voltage and current.

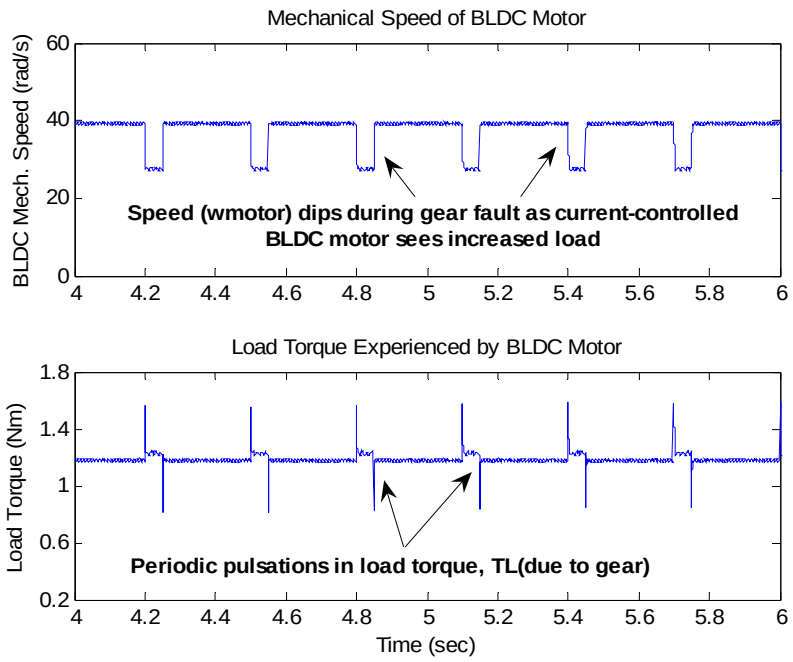

Figure 5.12: Top plot: Mechanical speed of BLDC motor (rad/s); Bottom plot: Load torque based gear fault model where the load torque varies as $0.03w_{motor} + 0.4$ Nm.

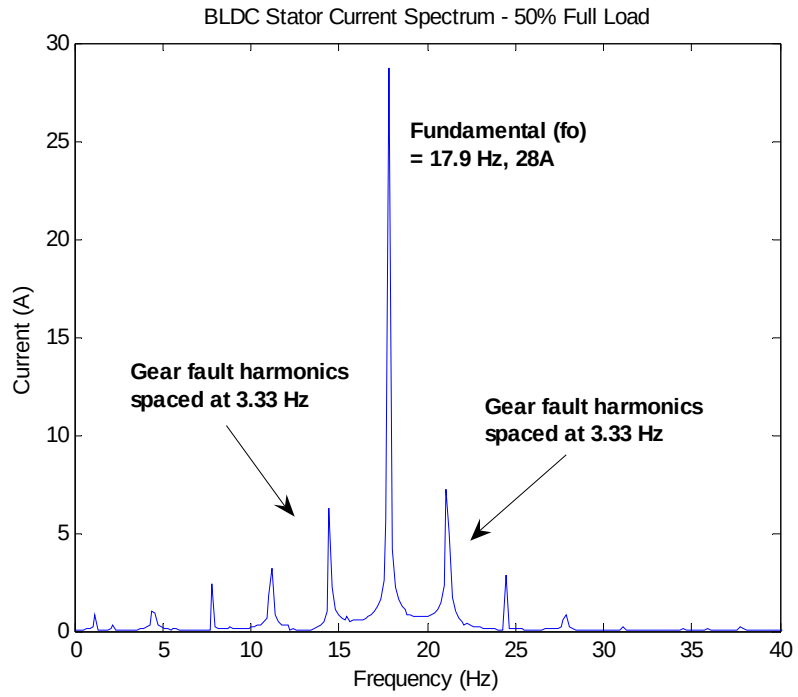

Figure 5.13: Simulated stator current spectrum of BLDC motor with defective gear (low speed-350rpm, 50% full load case).

5.6 Separation of Gear Faults from Rotor Related Faults in BLDC Motors

Potential rotor faults in BLDC machines include eccentricities, demagnetized rotor magnets, misalignments, and asymmetries [18]. Rotor eccentricities occur when there is an unequal air-gap between the stator and the rotor and are classified into two main types: static and dynamic [11, 63]. In such cases, the stator current of a BLDC motor can be used to monitor the motor health. It is known that certain rotor defects such as a dynamic eccentricities, a partially demagnetized magnet or even a misaligned rotor, can be detected by monitoring certain characteristic fault frequencies in the stator current of the BLDC motors operating at constant speed [59]. These frequencies are given by (3.16) (Chapter 3). These rotor fault frequencies are usually different from the gear fault frequencies given by (5.3) and (5.4).

The stator current spectrum of a BLDC motor-gear arrangement at a motor speed of around 3600 rpm is shown in Figure 5.14. The rotor fault frequencies are clearly different from the gear fault frequencies. This allows certain gear faults to be detected uniquely by simply monitoring the stator current or the voltage spectrum for characteristic frequencies, thus offering an inexpensive alternative to vibration-based diagnostics.

5.7 Voltage-Based Detection of Faults

In the research described in this paper, the BLDC motor drive is operated in a torque (current) control mode. An interesting observation that is made is the presence of fault frequency signatures in both the motor current and voltage spectra (Figures 5.5, 5.6, 5.8-5.11). These fault frequencies occur at the same location as in both the cases. This observation points out that voltage-based condition monitoring is possible in current-

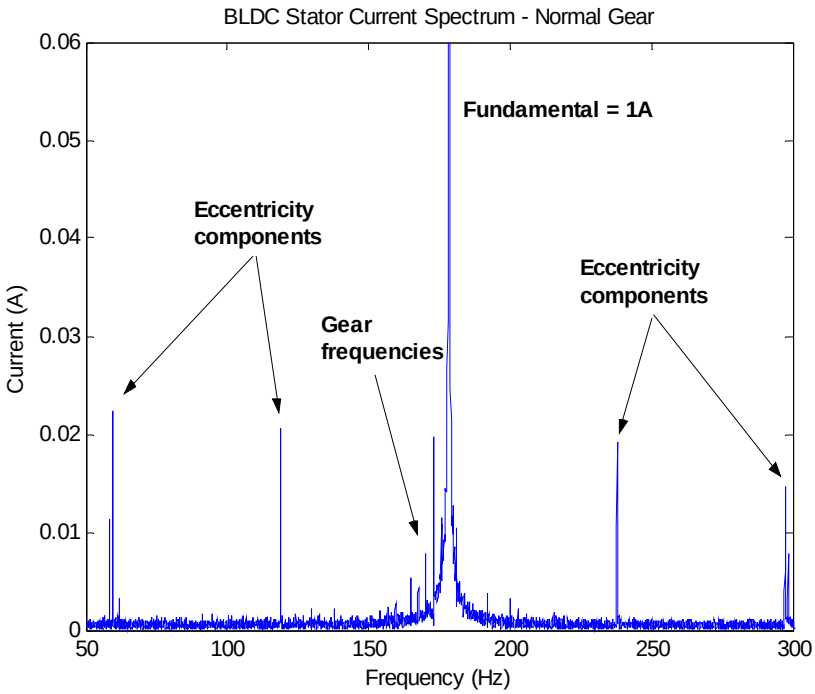

Figure 5.14: BLDC gear fault frequencies are different from the rotor eccentricity related frequencies.

controlled drive systems. This raises interesting questions: Why are the harmonics present in the motor current in a current controlled system and what is the mechanism of the generation of harmonics in the motor voltage in such drive systems?"

An ideal current-controlled motor with an infinite bandwidth current controller has no stator current harmonics, as the motor current is perfectly regulated to the reference value and any load perturbation is completely rejected in the stator current signal. However, in such a case, the abnormality in the electric motor should appear instead in the stator voltage. In reality, this is not completely true as practical current controllers have a finite bandwidth. Hence, if the load torque has a low-frequency oscillating component, especially at a frequency that is smaller than the bandwidth of the practical current controller, then the perturbation passes on to the stator current through

the controller, though attenuated to some extent (i.e. in this case the current controller is not able to completely filter off the perturbation). The current controller only partially attenuates or tries to correct for the perturbation (abnormality) by varying the voltage, resulting in some harmonics at the same frequencies being also present in the voltage. The magnitude of the harmonics in both the current and the voltage eventually depends on the current controller bandwidth. This presence of fault harmonics in both the motor current and voltage provides additional tools for fault detection that could make a diagnostic scheme more flexible and more reliable. This is useful for instance, if the fault signatures are too small to measure in the current.

5.8 Coupling Misalignment (Angular) Faults

An angular coupling misalignment causes fault harmonics similar to those caused by eccentricity related faults. The angular misalignment is implemented by inserting some shims on one of the bolts that fixes the six-pole BLDC motor to the frame, thus causing a misalignment. The experimental result under a 60% full load condition is shown in Figure 5.15 and displays the change in harmonics caused by the angular misalignment. It can be observed from Figure 5.15 that only the $1/3^{rd}$ and $5/3^{rd}$ harmonics increase as hypothesized by equation (3.14). Measured results for an aligned and a misaligned coupling have indicated an increase in the $1/3^{rd}$ fundamental frequency component from 206 mA to 520 mA (good coupling to a misaligned coupling) and a $5/3^{rd}$ fundamental frequency component change from 135 mA to 464 mA (good coupling to a misaligned coupling). It appears that the misalignment frequencies are represented by sidebands that occur at twice the rotor speed. This has indeed been widely believed in the industry [29, 30].

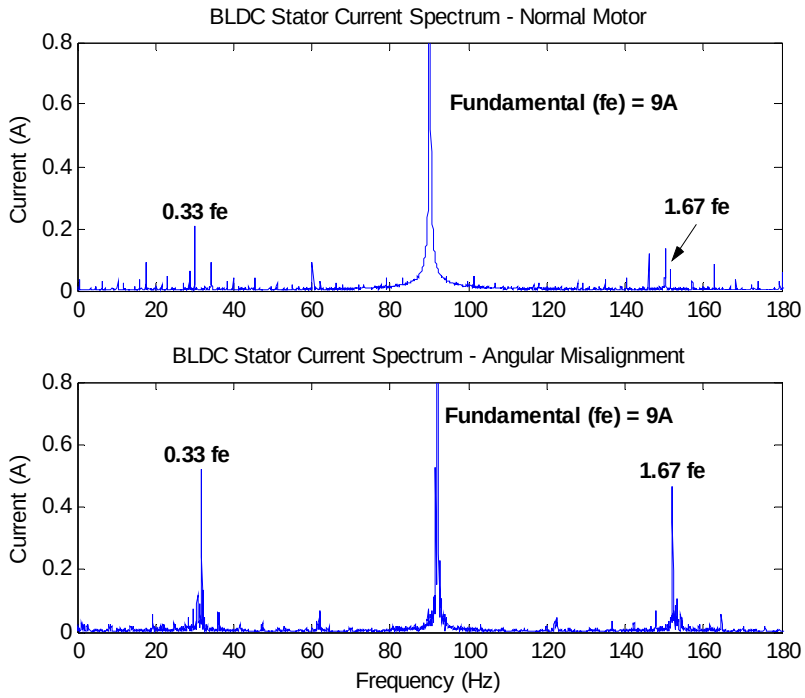

Figure 5.15: BLDC stator current spectrum – angular misalignment.

5.9 Conclusions

It has been demonstrated through both theory and experiments that faults in gears coupled to electric motors may develop unique fault signatures in either the voltage or the current in the motor driving the gear. This may offer a method an inexpensive and novel load-diagnostic alternative to vibration-based diagnostics that require accelerometers and associated sensor wiring.

The gear fault frequency components are clearly visible in the motor current and voltage spectra for faulty gears. These frequencies are different from the motor related faults such as eccentricities and can be uniquely identified. They change with the presence of a fault in the gear and tracking these frequencies in the current or voltage spectrum can help monitor the health of the gears

Three kinds of faults localized tooth damage, scoring (loss of lubricant), and debris in the gear lubrication have been experimentally implemented. The mechanism of generation of faults is further validated by simulation. For simulation, the faulty gear has been modeled as a pulsating load. Simulation results confirm that this model adequately represents the faulty gear behavior. Another important observation is that the motor and load faults can also be detected from the motor voltage. Detecting faults from the motor voltage is particularly helpful in applications that have only a current control loop, where the fault frequency components are more visible in the voltage than in the regulated motor current.

Chapters 4 and 5 investigate the subject of motor and load fault detection under constant speed operation. The third and most important part of this research investigates the problem of fault detection under non-stationary motor operation. An introduction to this problem is provided in the next chapter, Chapter 6.

CHAPTER 6

DETECTION OF ROTOR FAULTS IN BLDC MOTORS OPERATING IN NON-STATIONARY CONDITIONS

The objective of this chapter is to evaluate methods that can be used to track and detect rotor faults in BLDC motors operating under transient (non-stationary) conditions. The term non-stationary in signal processing literature has a different connotation and is usually described statistically [3]. However, from an electric motor's operating point of view, this simply refers to an operation where the motor's operating points continuously change with time and the motor is never operating at a constant speed through out its operation. Several significant challenges appear in the diagnostics of rotor faults in motors operating under non-stationary conditions and these will be discussed in detail in this chapter. This chapter also reviews the several signal processing techniques that could be used in non-stationary signal analysis, which is a crucial element to detect motor faults in non-stationary operating conditions.

6.1 Introduction

It has been assumed so far that the motor is operating in a steady state condition (constant speed application). This fundamental assumption of stationarity allows the use of the well known method of Fourier Transformation in the frequency domain analysis of currents, voltages, and vibration signals to detect the various rotor and mechanical faults in an electrical machine. However, there are several applications where the motor is never operating at a constant speed or load. Such applications are commonly encountered in the aerospace, appliances and automotive industries. Diagnosis of motor

health in such applications could be critical to maintaining and improving process uptimes in industries, or providing increased safety to humans.

A segment of a permanent magnet brushless DC motor (BLDC) stator current in a non-stationary state representing an automotive actuator application is shown in Figure 6.1. The top part of Figure 6.1 shows a BLDC stator current snapshot for 10 seconds sampled at 2 kHz. A dynamometer representing a speed proportional load is used to load the BLDC motor in Figure 6.1. The motor operates at full load at rated speed. One portion of the same current is zoomed for one second and is shown in the bottom part, clearly depicting the simultaneously changing motor frequency and amplitude. In the non-stationary motor behavior under investigation in this research, an electric motor operates in conditions shown in Figure 6.1 throughout its operation.

The motor operating in such a non-stationary environment has a non-stationary voltage, current, and vibration signal. Analysis of non-stationary signals is inherently complicated as simple and robust techniques such as the FFT can no longer be used. This means that more sophisticated signal processing techniques, often under assumptions of local or slow stationarity, are needed. Even under these assumptions, it is difficult to arrive at a solution that may be effective over a wide range of operating conditions and faults. These issues are further discussed in detail in this chapter.

6.2 Challenges in Non-Stationary BLDC Motor Fault Diagnostics

1. The stator current is a multi-component non-stationary signal containing many frequency components that have to be simultaneously monitored.
2. The motor to be diagnosed is a six-pole 12 V BLDC (trapezoidal back-EMF) motor that is driven from a square-wave inverter.

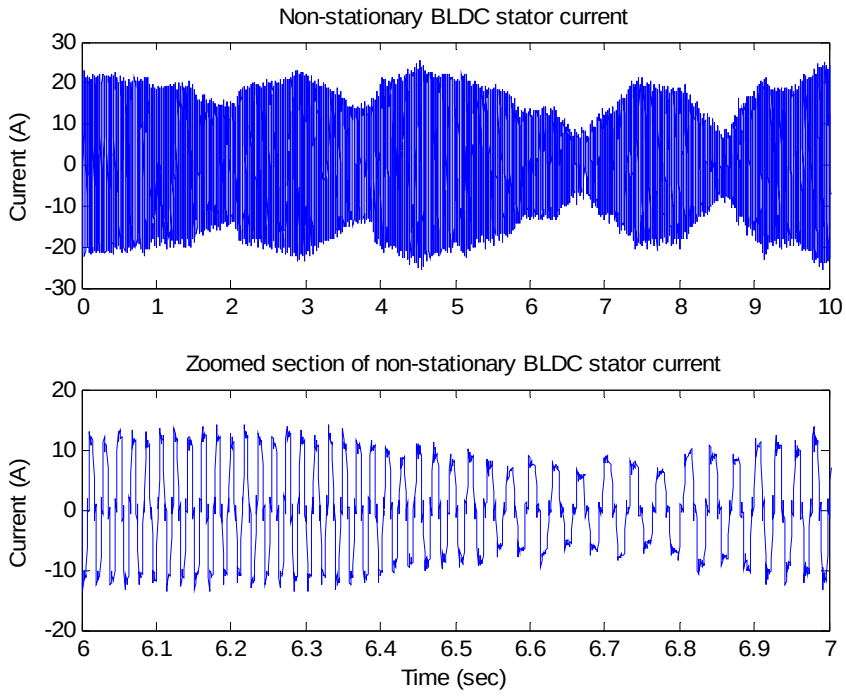

Figure 6.1: Top: Non-stationary stator current in a BLDC motor; Bottom: Zoomed section of top plot depicting continuously changing motor frequency and amplitude.

The main frequency components in the square-wave current signal of a Y-connected stator of a six-pole BLDC motor can be described as

a. Inverter frequencies f_e, $5\ f_e$, $7\ f_e$, $11\ f_e$, $13\ f_e$ … where f_e is the fundamental frequency.

b. Fault frequencies calculated from (3.10): $f_e/3$, $2\ f_e/3$, $4\ f_e/3$, $5\ f_e/3$. All the fault frequencies may or may not be present depending on the rotor defect.

3. The fault frequency amplitudes are less than 1% of the fundamental amplitude. Thus the rotor fault information in the stator current signal comprises a miniscule part of the total energy in the signal. This makes the separation of the fault frequencies from the inverter frequencies difficult.

4. f_e varies with time (over a range of 0 – 180 Hz in this case) as the signal is non-stationary.
5. The BLDC drive system does not have a speed sensor. The only available speed sensor is a Hall position sensor that is used to determine the rotor position every 60 degrees. Hence, any speed measurement may have to be derived from the Hall position sensor.

The focus of the present research is to develop a condition monitoring scheme that can detect incipient rotor faults under non-stationary operating conditions. The development of such a scheme is divided into the following parts:

- A **fault feature extraction method** that can extract information from the non-stationary signal (the BLDC motor stator current in this case), such that it can be used to detect faults. This is the most important and difficult part of any diagnostic scheme and would need sophisticated signal processing techniques.
- A fault **metric** that can use the information extracted above to determine the severity of the fault.

6.3 Signal Processing Techniques for Non-Stationary Fault Feature Extraction

As mentioned in the previous section, the first step in developing a non-stationary diagnostic scheme is to develop an analysis technique that can be used to convert the raw current signal to more useful information, particularly in the frequency domain. As the current is in a non-stationary state, the commonly used Fourier transformation can no longer be used, at least not in its original form. Several techniques in the signal processing literature have been developed to analyze such signals. The following methods are evaluated as potential solutions for this problem:

i. Time-frequency/time-scale methods:
    a. Windowed Fourier ridges (short time Fourier transform – STFT)
    b. Cohen class distributions
        i. Wigner-Ville distributions (WVD)
        ii. Choi-Williams distribution (CWD)
        iii. Zhao-Atlas-Marks distribution (ZAM)
    c. Wavelets
ii. Hidden Markov Models (HMMs)
iii. Time-series methods:
    a. Spectral estimation through ARMA models
    b. Adaptive filtering methods

These are now discussed in more detail.

6.3.1 Time-Frequency/Time-Scale Methods

Time-frequency analysis is the three-dimensional time, frequency, and amplitude representation of a signal, which is inherently suited to indicate transient events in the signal. Time-frequency (t-f) distributions are commonly used to diagnose faults in mechanical systems. The t-f distributions can accurately extract the desired frequencies from a non-stationary signal. In electric motors, the mechanical and electrical time constants are relatively large. Hence, the stator current in non-stationary operation varies slow enough to preserve all frequencies including the fault frequencies and these can be extracted over time. This makes the t-f distributions especially appealing to motor diagnostics.

The short time Fourier transform (STFT) is a mathematically linear t-f distribution. T-f distributions also include quadratic distributions, such as the Wigner-Ville distribution (WVD), the Choi-Williams (CWD) distribution and the Zhao-Atlas-Marks distribution (ZAM) [60-62]. The quadratic t-f distributions offer more frequency resolution than the linear t-f distributions. However, the price often paid is the generation of unwanted frequency components, ghosts, and artifacts; as well as the increased computation that is needed to suppress these unwanted spectral components.

Time-scale methods often refer to wavelets. In wavelet analysis, a signal is analyzed at different scales or resolutions: a large window is used to look at the approximate stationarity of the signal and a small window is simultaneously used to look for transients. This multi-resolution or multi-scale view of the signal is the essence of wavelet analysis [67]. The choice of the wavelet is critical to proper a fault feature extraction. A *real wavelet* does not possess separate phase information and hence is suitable only for detecting sharp transients [68]. This is not of much use in motor diagnostics where the fault information is spread throughout the signal. However, a *complex analytic wavelet* can separate amplitude and phase components from a signal and is commonly used to measure instantaneous frequencies [69]. This offers a better choice for motor fault detection.

6.3.2 Hidden Markov Models (HMM)

A HMM is a stochastic signal model that has been widely used for communication and signal processing applications. HMMs are based on an extension of the concept of Markov chains to include cases where the observation is a probabilistic function of the state [70]. Left-right HMMs have been most widely used for isolated

word recognition systems, where words are modeled by a series of phonetic states that occur as a one-way left to right sequence. These HMMs are developed through training a lot of data. These methods have also been widely used in vibration-based gear fault detection, tool wear diagnostics, and even in electrical machine monitoring, but again the underlying assumption in such applications has been local stationarity in the vibration signal [71-74]. However, in the present application the signal is continuously and randomly changing, and there is no local time period during which a stationary training data could be obtained. It is therefore suggested that the HMMs may not be a suitable technique for non-stationary motor diagnostics.

6.3.3 Time-Series Methods

Time-series modeling is a parametric solution for spectral analysis [3, 75, 76]. An important advantage of this method over the non-parametric spectral techniques that use windowed/tapered periodograms is the possibility to automatically select the best model order and model type. Moreover, the time-series spectra are more accurate when using stochastic processes, as compared to using periodograms [76]. The three model types that can be used for time-series modeling are the autoregressive (AR), the moving average (MA), and the combined ARMA models. However, the key point in time-series modeling is that these models can characterize all stationary stochastic processes but cannot model non-stationary phenomena. To overcome this, the non-stationary signal under analysis is divided into several segments such that each segment represents a stationary or a slowly varying waveform. Each segment is then used to develop and adapt the time-series model over time. The AR models are more suitable for modeling peaks in the spectrum and the MA models are better for modeling the valleys. In

practice, most stationary processes can be described adequately by AR(p), MA(q) or combined ARMA(p,q) processes of finite orders p and/or q. A typical ARMA(p,q) process has the form

$$H(z) = \frac{\sum_{k=0}^{q} b_q(k) z^{-k}}{1 + \sum_{k=1}^{p} a_p(k) z^{-k}}, \tag{6.1}$$

where b_q and a_p are the coefficients of the numerator and denominator of the ARMA model. A power spectrum of the model can be calculated from the estimated model parameters [3] as

$$\hat{P}_{ARMA}\left(e^{j\omega}\right) = \frac{\left|\sum_{k=0}^{q} \hat{b}_q(k) e^{-jk\omega}\right|^2}{\left|1 + \sum_{k=1}^{p} \hat{a}_p(k) e^{-jk\omega}\right|^2}, \tag{6.2}$$

where $\hat{b}_q$ and $\hat{a}_p$ are the estimated coefficients of the numerator and denominator of the estimated ARMA model. The roots of the denominator of *H(z)* directly yield the frequencies of the peaks in the corresponding power spectrum of (6.2) [77]. Thus, accurate and selective frequency estimation is possible. However, the accuracy of the model plays a large part in the effectiveness of this solution.

The parameters of the ARMA model can be estimated using either the Yule-Walker method, the Prony's method, the Shank's method or using the iterative prefiltering technique (Steiglitz-McBride method) [3, 76, 78]. The model order can be

chosen through several methods and efficient model ordering methods exist that yield mean square error estimates approaching the optimal Cramer-Rao bound [79-81].

Though this method seems promising, *several drawbacks appear when it is applied to non-stationary signals*. The first issue is stationarity. The segmented data window needs to contain stationary data. Time-varying waveforms affect the autocorrelation matrix upon which these models are based, thereby creating inaccurate models. A window with sufficient stationary time data is often difficult to obtain. Another difficulty commonly encountered is the choice of optimum model order. Over-modeling (higher than necessary order) and under-modeling (lower than optimum order) can both cause inaccurate models with spurious frequency components that may not exist in the real signal [3]. A possible solution may be adaptive time-series techniques, but these are not considered at this time because of their complexity.

6.4 Conclusions

A comparison of different available techniques to analyze non-stationary signals has been done and the following conclusions are reached:

a. Assuming that the electric motors and their loads have large mechanical time constants, any transient response to sudden changes in operating conditions is slow, resulting in the frequency information being preserved in the electrical signals of the motor. Therefore, the time-frequency and time-scale distributions appear to be the best initial approach to the problem of motor fault diagnostics because of their ease of implementation and their ability to extract fault frequencies dynamically over time. These distributions are investigated further in Chapters 7 - 9.

b. Another significant issue in motor fault diagnostics is the small magnitudes of the rotor fault frequency components, which means that the fundamental frequency component and the other higher inverter harmonics have to be filtered prior to any signal processing. If unfiltered, most signal processing methods would neglect these small fault magnitudes as noise. This filtering has to be adaptive as the signal is non-stationary.

CHAPTER 7

NON-STATIONARY ROTOR FAULT DETECTION USING WINDOWED FOURIER RIDGES

The objective of this chapter is to propose a windowed Fourier ridge algorithm for the detection of rotor faults in BLDC motors operating under continuous non-stationarity. A key assumption made here is that the stator current contains unique fault frequency components that can be used for rotor fault detection. The algorithm computes local maxima (or ridges) from the spectrogram (STFT) of an adaptively filtered motor current signal. The proposed method allows continuous real-time tracking of rotor faults in BLDC motors operating under continuous non-stationary conditions, thus allowing the continuous monitoring of the motor health. Although the method could be readily generalized, its presentation is limited in this chapter to BLDC motors.

7.1 Introduction

The first method proposed in this dissertation to detect rotor faults in a BLDC motor operating under transient conditions is based on the well-known STFT. It is known that rotor defects such as dynamic eccentricity can be detected by monitoring certain characteristic fault frequencies in the stator current of BLDC motors operating at a constant speed [59]. These frequencies are given by (3.10). These fault frequencies are also present when the current is non-stationary (dynamic motor operation). In such a case, the fault components change in frequency and magnitude depending on the operating point (speed and load) of the motor. These fault frequencies can be tracked continuously over time using the proposed algorithm.

7.2 Spectrogram And Windowed Fourier Ridges

7.2.1 Windowed Fourier Transform And Spectrogram

The windowed Fourier transform (WFT) was developed by Gabor in 1946, when windowed Fourier atoms were introduced to measure the "frequency variations" of sounds. The windowed Fourier transform, *Sf* of a function *s(t)* is given by [68]

$$Sf(t,\xi) = \int_{-\infty}^{+\infty} s(\tau)\, g(\tau - t)\, e^{-i\xi\tau} d\tau \,, \tag{7.1}$$

where $g(\tau)$ is a real and symmetric window translated by t and modulated by the frequency ξ, t is the instantaneous time, τ is the "running time". This transform is also called the short time Fourier transform (STFT) because of the multiplication by $g(\tau-u)$ localizes the Fourier integral in the neighborhood of $t = \tau$. The resolution in time and frequency of the WFT depends on the spread in time and frequency of the selected window type (Rectangle, Blackman, Hamming, Gaussian, Hanning, etc.). This spread is the smallest when the Gaussian window defined by (7.2) is used [68].

$$g(t) = e^{\left(-18t^2\right)}. \tag{7.2}$$

The STFT can be implemented digitally and efficiently in real time using discrete Fourier transforms (DFT). The energy density possessed by the WFT is called a Spectrogram, denoted by P_{Sf} and is given by [68]

$$P_S f(t,\xi) = \left|Sf(t,\xi)\right|^2 = \left|\int_{-\infty}^{+\infty} s(\tau)\, g(\tau - t)\, e^{-i\xi\tau} d\tau\right|^2 . \tag{7.3}$$

7.2.2 Windowed Fourier Ridges (WFR)

The spectrogram measures the energy of *s(t)* in the time-frequency neighborhood of *(t,ξ)*. The windowed Fourier ridges are the local maxima of the spectrogram that represent the instantaneous frequencies. The instantaneous frequency of any function, *s(t)*, is defined as a positive derivative of the phase, $\varphi'(t) \geq 0$, where φ is the phase of *s(t)* [68]. If the signal, *s(t)*, has only one frequency component, then the instantaneous frequency is $\xi(t) = \varphi'(t)$, and the amplitude *a* can be calculated by

$$a(t) = \frac{2\left|Sf\left(t, \xi(t)\right)\right|}{\sqrt{s_l}\left|\hat{g}(0)\right|}, \tag{7.4}$$

where s_l is the length and $\hat{g}(\omega)$ is the Fourier transform of the window, *g(t)*, respectively. If $\Phi_S(t,\xi)$ is the complex phase of $Sf(t,\xi)$, then it can be shown that the ridge points are also the points of stationary phase [68], since

$$\frac{\partial \Phi_S(t,\xi)}{\partial t} = \varphi'(t) - \xi = 0\,. \tag{7.5}$$

The equations (7.4) and (7.5) are based on a theorem that is explained in Appendix C. The ridge algorithm thus computes the instantaneous frequencies of a signal *s(t)* from the local maxima of $P_S f(t,\xi)$. This approach was introduced by Delprat et al. to analyze musical sounds [82].

The practical implementation of the ridge algorithm is as follows. Generally, the number of instantaneous frequencies is unknown. In such cases, all local maxima of $P_S f(t,\xi)$ that are also points of stationary phase are calculated. These points define curves in the *(t,ξ)* planes, which form the ridges of the windowed Fourier transform. Ridges that

have a small amplitude are often removed because they can be artifacts of noise variations or "shadows" of other instantaneous frequencies created by the side-lobes of $\hat{g}(\omega)$. If the signal consists of only a few frequencies then all the local maxima are themselves the ridges and can be checked by computing the stationarity of their respective phases using (7.5). The ridges will be distinct as long as the distance between any two instantaneous frequencies (φ'_1 and φ'_2) satisfies (7.6), where $\Delta\omega$ is the bandwidth of the window [68].

$$\left|\varphi_1'(t)-\varphi_2'(t)\right| \geq \frac{\Delta\omega}{s_l}. \tag{7.6}$$

7.3 Viability of Using WFR for Fault Detection

To illustrate the concept, a test signal i_a approximating a rotor fault, and having a fundamental of amplitude 0.05 A (corresponding to a filtered stator current) with two rotor fault sidebands of amplitude 0.07 A, is generated using

$$\begin{aligned} i_a = 0.05\cos\left(2\pi p(t)t\right) + 0.07\cos\left(4\pi p(t)t/3\right) \\ + 0.07\cos\left(8\pi p(t)t/3\right). \end{aligned} \tag{7.7}$$

The three frequencies in (7.7) are the fundamental frequency, $p(t)$, and the two rotor fault frequencies at 2/3rd and 4/3rd of the fundamental frequency $p(t)$. The amplitudes in (7.7) are chosen arbitrarily to imitate a rotor fault scenario as close as possible. A one second record with 2048 samples is used for comparing the various signal processing techniques. The frequency, $p(t)$, is varied sinusoidally between 0 and 120 Hz as in (7.8).

$$p(t) = \sin\left(2\pi ft\right) \ \textit{where } f = 120 \textit{ Hz}. \tag{7.8}$$

Figure 7.1 shows the two-dimensional time-frequency plot of the Fourier ridges (instantaneous frequencies) of the test signal extracted from the spectrogram computed using (7.3). The time-frequency plot of Figure 7.1 describes the variation of the three frequencies (y-axis) in the signal, i_a, over time (x-axis). The Wavelab802 toolbox for MATLAB from Stanford University is used to implement the windowed Fourier ridge algorithm [83]. The choice of a windowing function can play an important role in determining the quality of the overall results. The main role of the window is to damp out the effects of the Gibbs phenomenon that results from truncation of an infinite series [62, 84]. Different windows offer different trade offs between the ability to offer good frequency resolution and the introduction of undesired artifacts (Gibbs phenomenon) [62, 84]. A Gaussian window of length 0.1 seconds is used in the present simulation example though other window types could be used. This length is chosen through trial and error to obtain a good frequency resolution, while simultaneously maintaining time resolution. A larger window length produces a smaller frequency resolution, while not providing any significant improvement in the time resolution. Similarly, a shorter time window provides a marginally improved frequency resolution while reducing the time resolution. The rotor fault frequencies at 2/3rd and 4/3rd of the fundamental frequency, along with the fundamental itself, are seen to be distinctly tracked over time in Figure 7.1, except in the low-frequency region of 0 to 40 Hz. The frequency resolution is reduced at low frequencies and this is expected because of the relatively short window length. Figure 7.1 shows that the frequency components of the stator current waveform of a faulty

BLDC motor can be distinctly detected over a wide frequency range using the Fourier ridge method. The simulation demonstrates the feasibility of the approach, but also underscores possible limitations such as the choice of the length and type of the window. However, the method is robust and easy to implement in practice.

7.4 Windowed Fourier Ridge Fault-Detection Algorithm

A block schematic of the proposed algorithm is shown in Figure 7.2. The proposed algorithm to monitor developing rotor faults in a BLDC motor is as follows. Firstly, the fundamental and harmonics greater than two are adaptively filtered using an analog switch capacitor tracking filter (ATF) that is explained in more detail in section 7.6. As the amplitudes of the rotor fault frequencies in the stator current of a defective BLDC motor are small in comparison to the fundamental, the ridge algorithm will extract the fundamental frequency instead of the fault frequency. Hence, the stator current has to be filtered to remove the fundamental and all other inverter harmonics, prior to the application of the ridge algorithm. The adaptive filtering process removes all inverter harmonics and leaves only the fault frequencies behind in the signal.

Next, a spectrogram is obtained using (7.5) from the filtered current signal. A Gaussian window is used as it provides the best frequency resolution among all windows. The length of the window is typically chosen heuristically through trial and error. The Fourier ridges (amplitudes of the instantaneous frequencies of the spectrogram) are then extracted from the spectrogram by detecting the local maxima. This is done by looking at the peaks of the spectrogram. The peaks are determined to be actual frequency components if they satisfy the stationary phase condition of (7.5). The components of the spectrogram that do not satisfy (7.5) are automatically neglected.

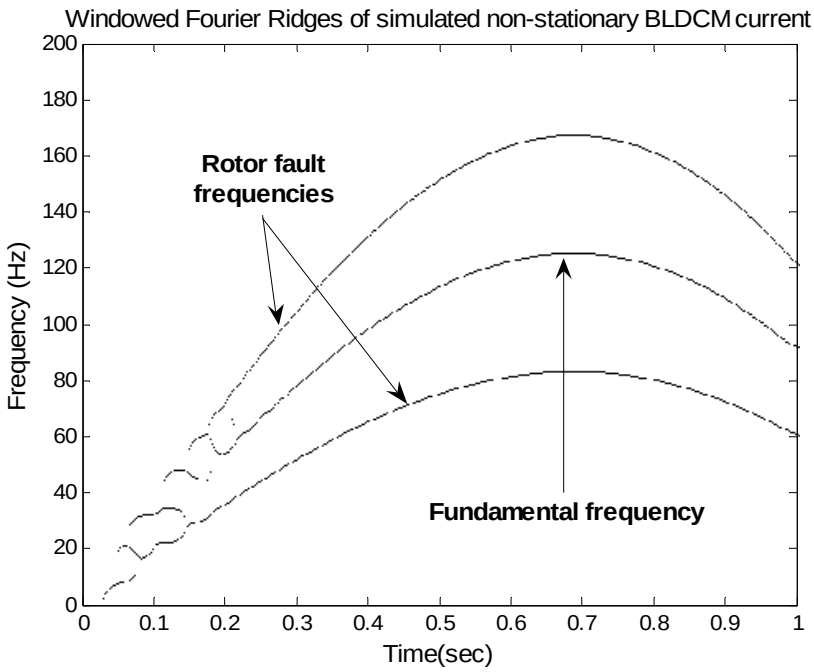

Figure 7.1: Windowed Fourier ridges of simulated non-stationary stator current in a faulty BLDC motor.

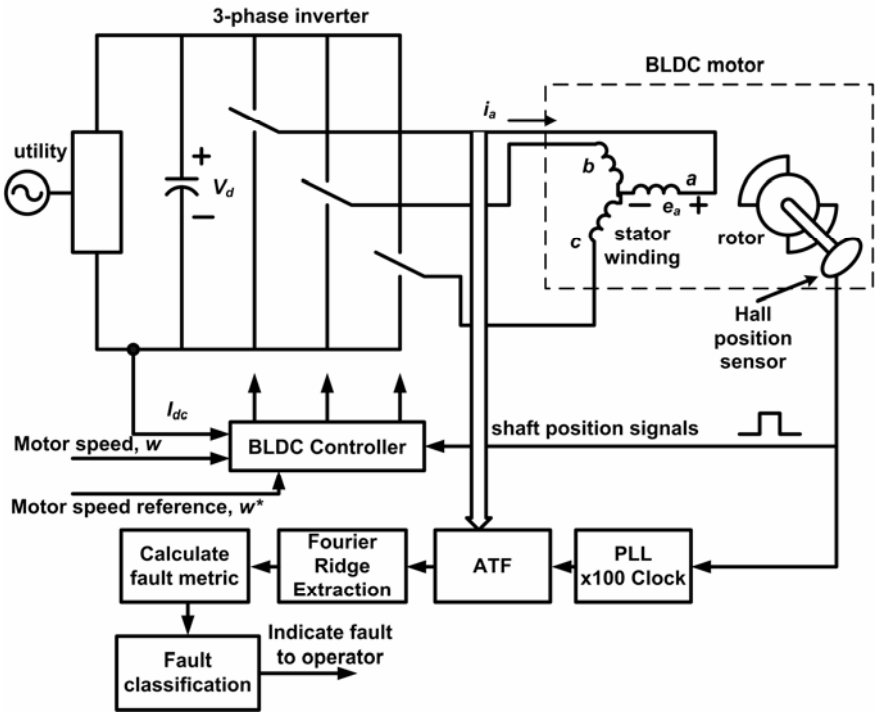

Figure 7.2: Rotor fault detection in BLDC motors using windowed Fourier ridge algorithm.

In practice, the process of determining the stationary phase for every frequency component is difficult to implement as the number of actual frequency components in the signal could be large and is needed only if the magnitude of the actual frequency components is comparable to noise (i.e, the signal-to-noise (S/R) ratio is poor). In the present application, the fault frequency components are much larger than the noise as shown in Figure 4.4 (Chapter 4). Hence, the components of the spectrogram that are ghosts, artifacts, and noise are removed by simply using a small threshold.

Fault classification is then done by using either a simple fault metric that directly monitors the magnitude of the fault frequencies (Fourier ridges) or by using more sophisticated classifiers such as an artificial neural network. The thresholds can be set to determine the severity of the fault and to provide an indication to the operator to take some precautionary action. Such thresholds can be set to vary with load and speed conditions. The fault classification algorithm will be explained in more detail in Chapter 10.

7.5 Experimental Setup

The experimental setup is shown in Figure 7.3. A 12 V, 1 kW, six-pole BLDC motor with surface mount magnets is coupled to a DC generator (dyno) that acts as a load. The dyno produces a load torque that is linearly dependent on the speed of the DC generator. At low DC generator speeds, a low load is obtained. Full load corresponding to 20 A of BLDC motor current is obtained at a speed of 1800 rpm.

The BLDC motor is driven by an inverter that features an integrated current control loop. The inverter is supplied from a 12 V deep cycle lead-acid battery as the intended application is an automobile power steering. An analog speed controller

designed at the Georgia Institute of Technology is used to control speed. A detailed block diagram of the complete BLDC motor controller is shown in Figure 7.4. The speed signal is provided by a 1000 ppr optical encoder coupled to the DC generator. Hall-Effect sensors are used to sense the motor stator currents. One of the phase currents is passed through the ATF as shown previously in Figure 7.2. The filtered current, as well as the raw input current, are acquired at a sampling rate of 2 kHz using a 16-bit data acquisition system.

For a six-pole BLDC motor, the rotor fault frequencies occur at $1/3^{rd}$, $2/3^{rd}$, $4/3^{rd}$, and $5/3^{rd}$ times the fundamental frequency as computed from (3.10). Rapid time-varying motor operation is obtained by varying the speed reference as shown in Figure 7.4. Experiments are conducted with sinusoidal, triangular, and randomly changing speed references. The sinusoidal and triangular references are varied between 0 to 10 Hz and represent most practically occurring applications. For example, the sinusoidal reference changes as in

$$\omega^* = 5\sin(2\pi f_{ref} t)$$
$$\textit{where } f_{ref} \textit{ is a frequency between 0 and 15 Hz} \tag{7.9}$$

A signal generator is used to provide the sinusoidal and triangular reference signals. The motor speed varies in the range of 600 rpm to 1800 rpm. The values of f_{ref} selected for these experiments are 3 Hz, 5 Hz, 8 Hz, 10 Hz, 12 Hz, and 15 Hz. The frequencies are selected to uniformly span over the range of 0 to 15 Hz. Two fault cases are presented here: a mechanically unbalanced rotor and a dynamically eccentric rotor. Both the faults are implemented as explained in Chapter 4.

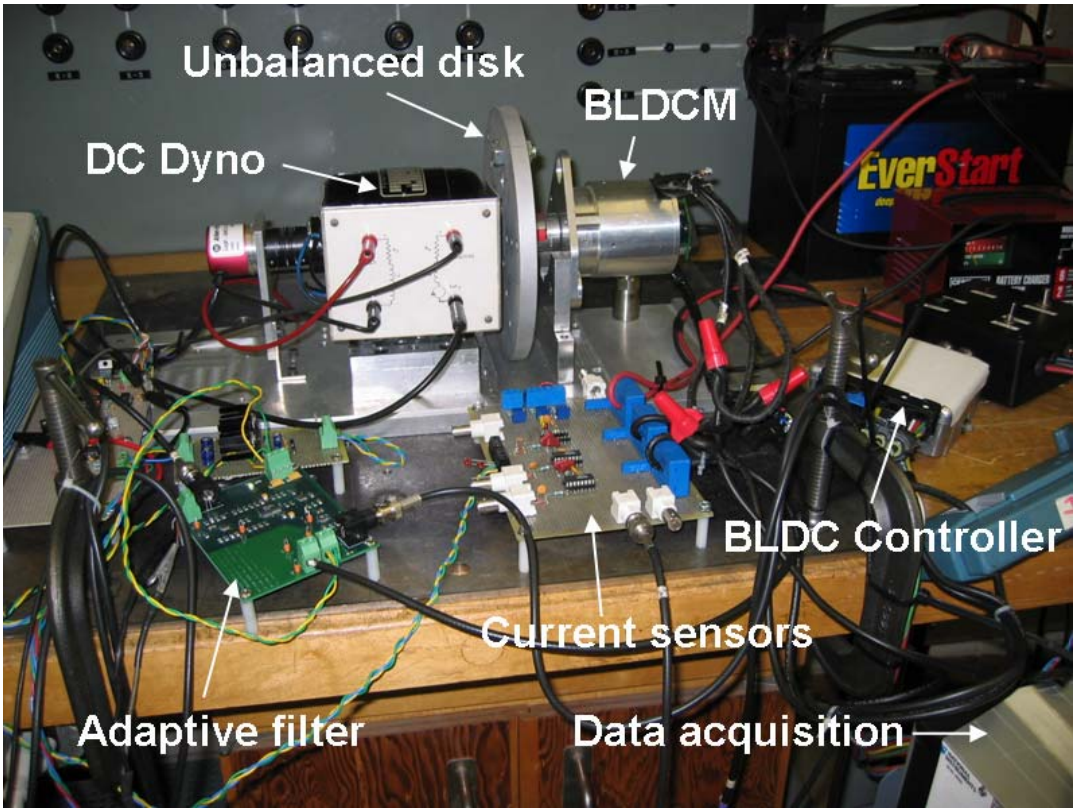

Figure 7.3: Experimental arrangement to test fault detection in dynamically operating BLDC motors.

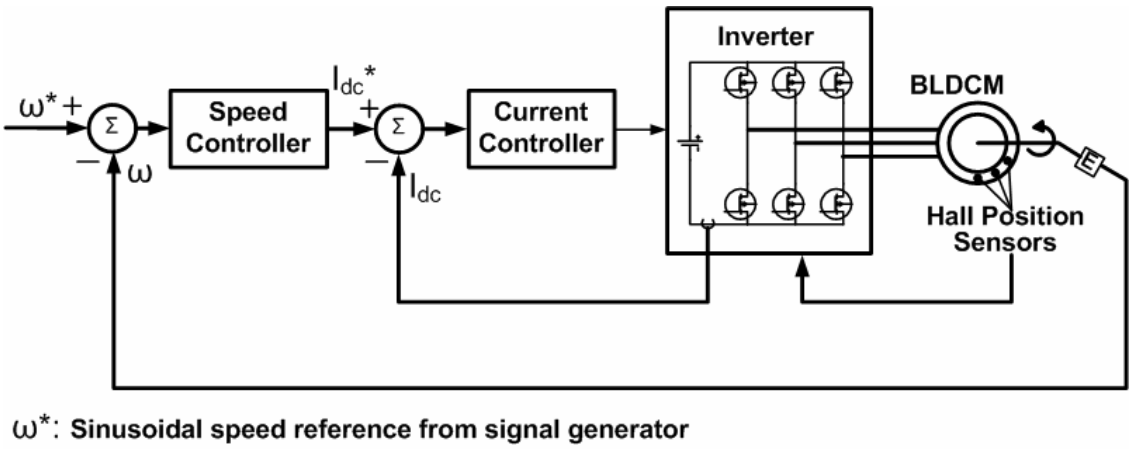

Figure 7.4: Detailed block diagram of BLDC motor controller.

7.6 Adaptive Tracking Filter (ATF)

The analog tracking filter (ATF) removes the fundamental and all harmonics that are greater than two. The ATF in Figure 7.5 consists of four components: a switch capacitor variable frequency elliptic notch filter, a switch capacitor variable frequency Butterworth low pass filter, a fixed frequency Butterworth low pass filter; and a Phase Locked Loop (PLL) clock. T The complete circuit is shown in Appendix D. Two filter systems, ATF1 and ATF2, are developed. A test ATF (ATF1) with a notch depth of 30 dB is initially prototyped on a vector board for evaluation. The ATF2 has a higher attenuation and its construction is described in the following sections.

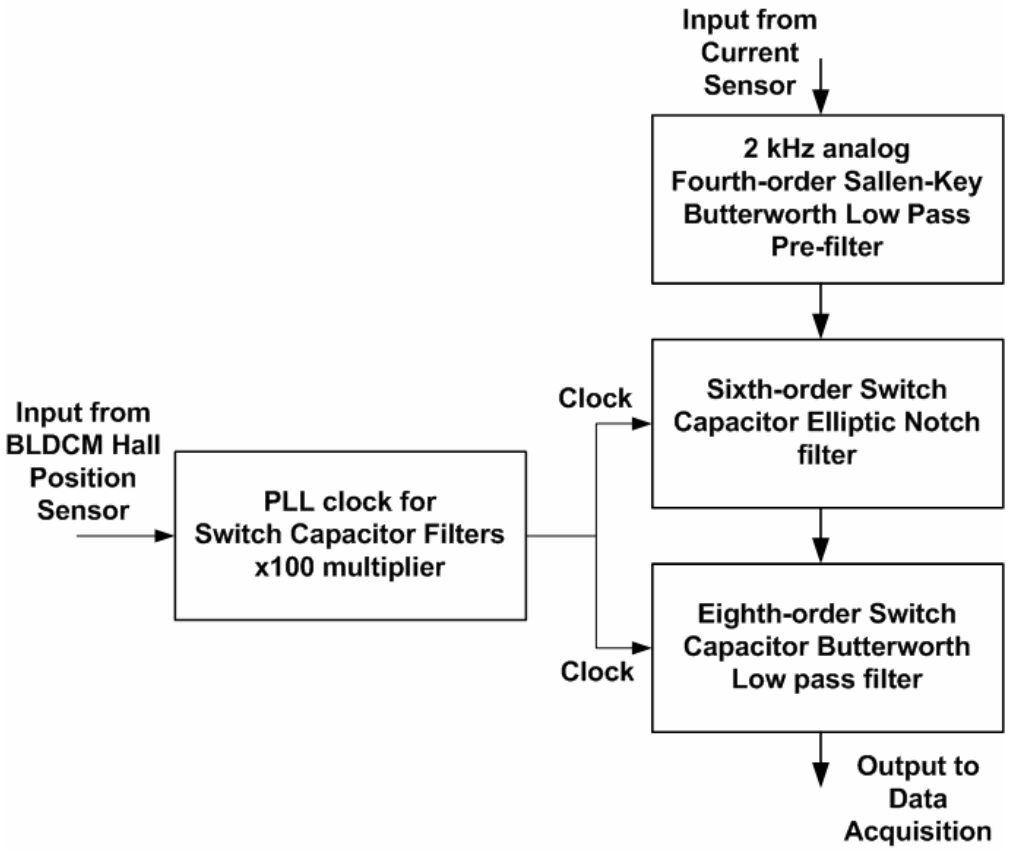

Figure 7.5: Block diagram of analog tracking filter (ATF).

7.6.1 Switch Capacitor Notch / Low Pass Filter

The notch filter of ATF2 that removes the fundamental is a sixth-order elliptic switch capacitor filter designed using the software FilterCAD from Linear Technologies [85]. The sixth-order filter is implemented using the LTC1061 high performance triple universal integrated circuit [86]. The switch filter capacitor circuit of the ATF2 is shown in Figure 7.6. The ratio of the 0 dB width to the notch width is 10:1 with a notch attenuation of 56 dB. The response of the notch filter obtained from FilterCAD is shown in Figure 7.7.

An eighth-order Butterworth low pass switch capacitor filter is then used to filter out all harmonics that are greater than two. The low pass switch capacitor filter is implemented using a monolithic eighth-order filter chip, MAX295 (Figure 7.6), available from Maxim [87]. A low pass attenuation of well over 80dB is achieved. The MAX295 also has an uncommitted operational amplifier that is used to finally amplify the filtered signal prior to data acquisition. The pass band ripple is measured to be less than 100 mdB. A simple RC post-filter removes the clock feed-through.

7.6.2 Fixed Low Pass Filter

A 2 kHz cutoff, fourth-order Sallen-Key Butterworth analog active filter circuit (Figure 7.8) is used to remove the 20 kHz PWM frequency components from the input current signal. This filter serves as an anti-aliasing pre-filter that is essential for all switch capacitor filters. The Sallen-Key filter was designed using the software FilterPro that is available from Texas Instruments [88].

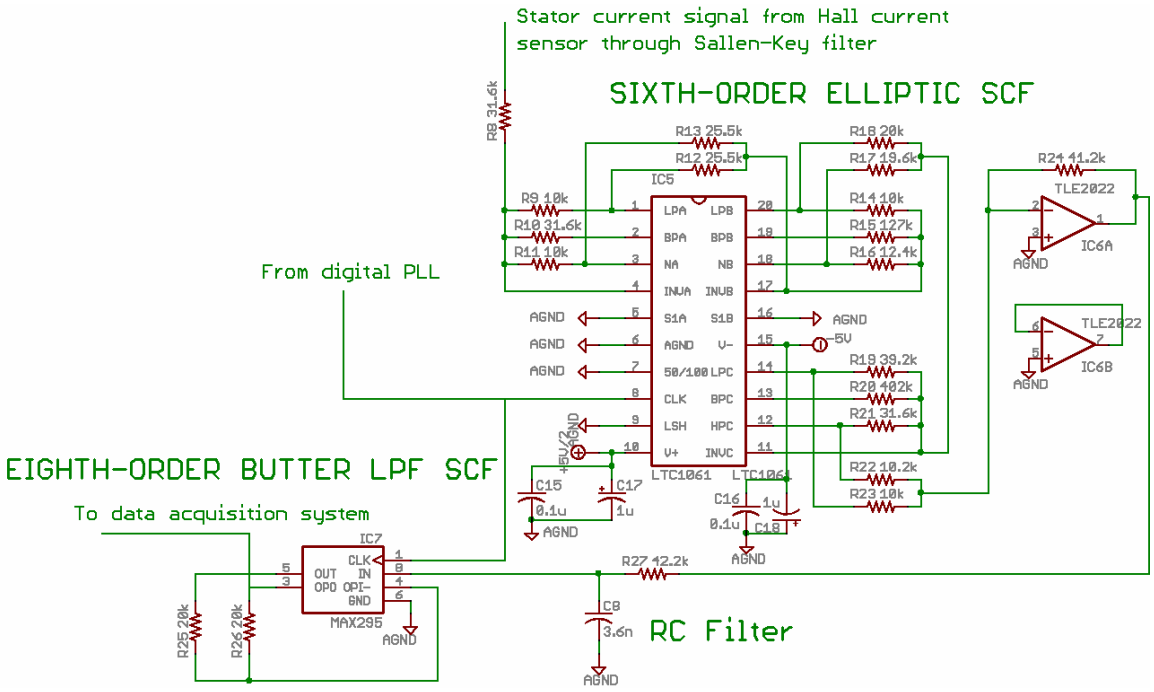

Figure 7.6: Circuit diagram of the switch capacitor filter section of the ATF.

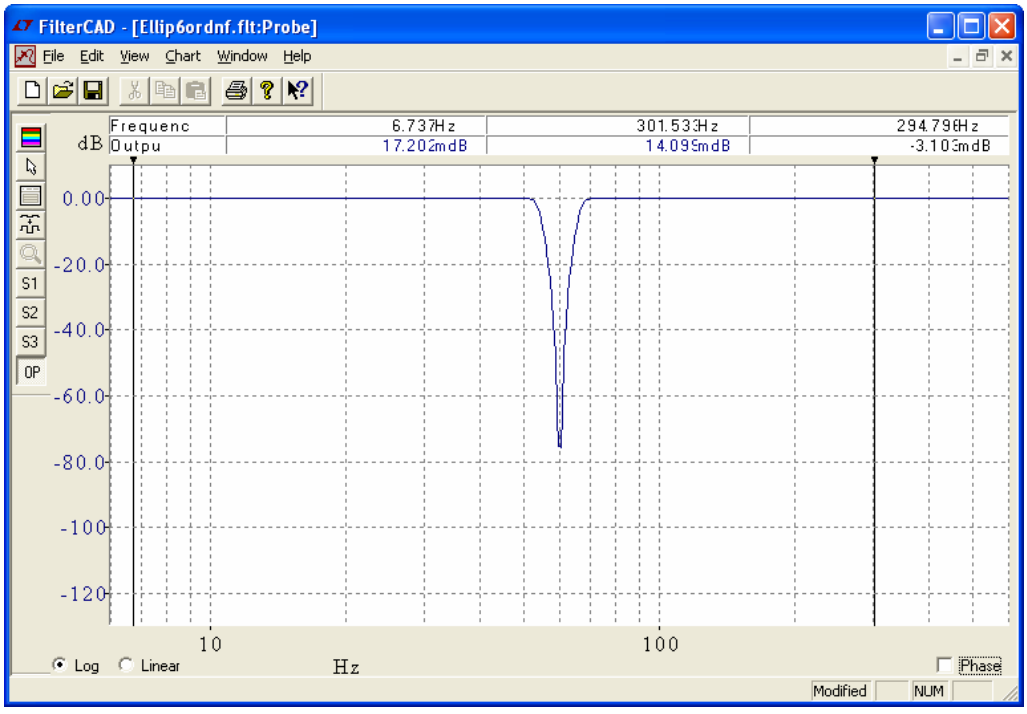

Figure 7.7: Frequency response of sixth-order Elliptic notch filter obtained using FilterCAD.

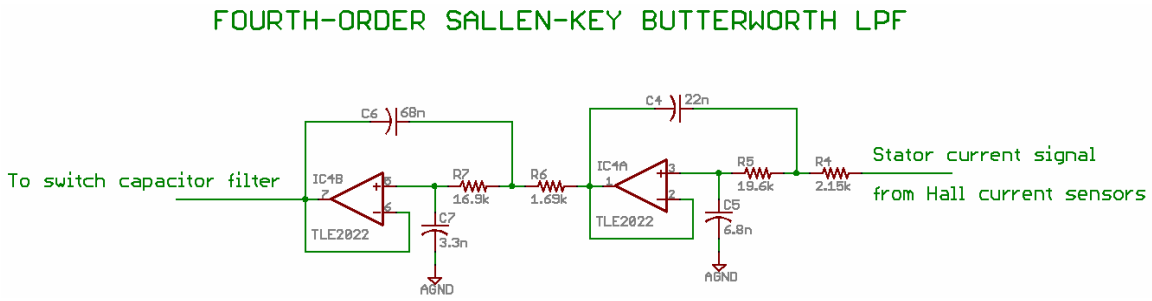

Figure 7.8: Circuit diagram of the fourth-order Sallen-Key Butterworth analog filter.

7.6.3 Digital Phase Locked Loop (PLL) Tracking/Clock Circuit

The switch capacitor filters need a clock frequency that is 100 times the fundamental frequency. A PLL circuit (Figure 7.9) using the commonly available CMOS circuit CD4046 is used to track the fundamental frequency from the Hall position sensor output, whose frequency is the frequency of the motor rotation and thereby the stator current. A divide-by-100 counter comprising of two CD4017 decade counters is inserted into the feedback loop of the PLL. This provides a frequency multiplication of 100 times the fundamental frequency obtained from the Hall sensor.

7.6.4 Filter Construction

The filter ATF2, described in the previous sections, is fabricated on a four-layer printed circuit board to obtain superior noise-free performance. Appendix D provides more details on the fabrication of this filter system. Figure 7.10 shows the completed ATF2 that is used in the experiments (Figure 7.3).

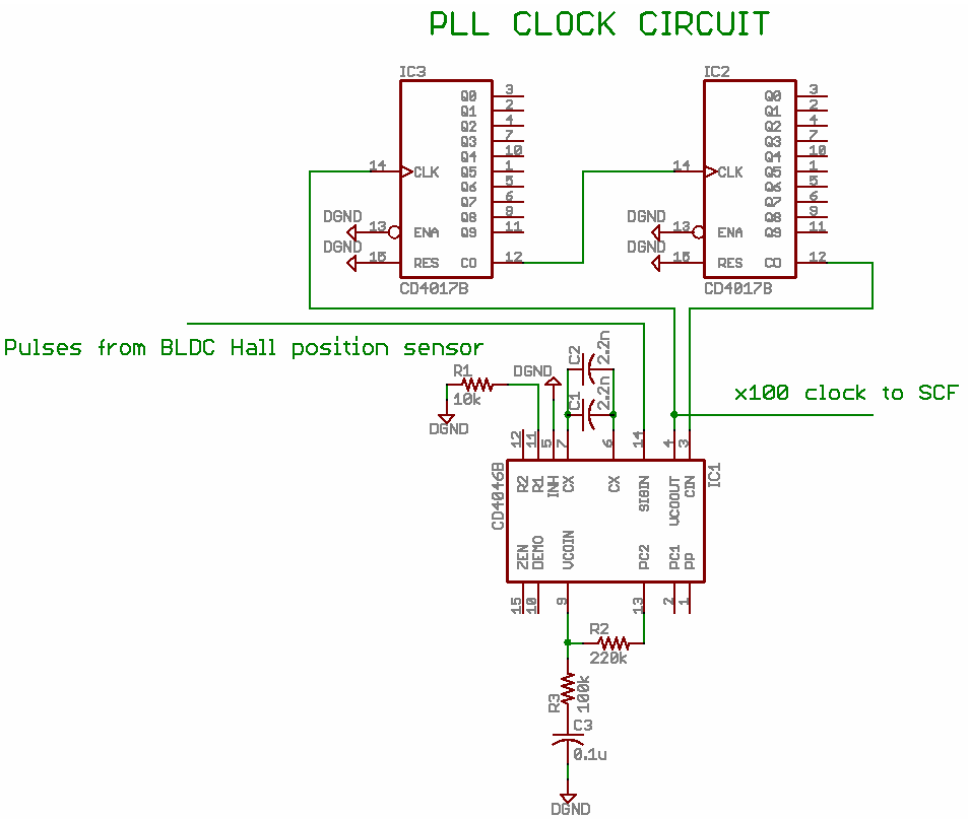

Figure 7.9: Circuit diagram of the digital PLL clock.

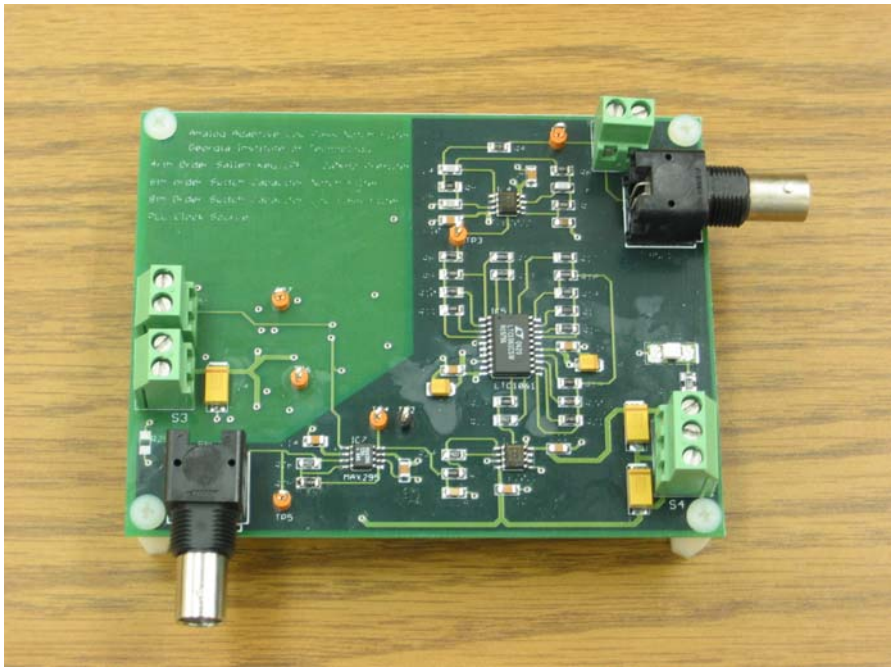

Figure 7.10: Analog tracking filter ATF2 designed at Georgia Institute of Technology.

7.7 Experimental Results

7.7.1 Mechanically Unbalanced Rotor – 3 Hz Sinusoidal Speed Reference

Mechanically unbalanced rotors are usually caused by misaligned load. This unbalance causes some dynamic eccentricity and motor vibration, eventually leading to a motor bearing failure. A mechanically unbalanced rotor is implemented by mounting a slotted disk on the shaft of the motor (Figure 7.3). The ATF1 with 30 dB notch attenuation is used in this experiment to remove the fundamental frequency and all frequencies above the second harmonic. A dc generator load is used for the BLDC motor. This provides full load to the BLDC motor at rated speed. The full load for the BLDC motor used in the experiments corresponds to 20 A.

A Gaussian window of length 0.25 seconds is used to compute the spectrogram using (7.3). This length is chosen through trial and error to obtain the best compromise between frequency- and time-resolution. The stator current of a mechanically unbalanced BLDC motor (with a bolt in one of the disc slots) operating with a 3 Hz sinusoidal speed reference and sampled at 2 kHz is shown in Figure 7.11. The corresponding spectrogram of the filtered stator current calculated using (7.3) is also shown in Figure 7.11. The fault frequencies are still not distinctly visible as the spectrogram extracts all spectral components including noise from the filtered current. The instantaneous fault frequencies or fault ridges are now extracted from the local maxima of the spectrogram by testing all the extracted maxima for stationary phase using (7.5). Thus, only the fault ridges (instantaneous fault frequencies) are extracted from the filtered current and are shown in Figure 7.12. A fundamental component is also present in the extracted ridges of Figure 7.12, as the 30dB test ATF used here does not remove the fundamental

frequency component completely. A color chart is provided in all the t-f plots that depict the relative magnitude of the amplitude of the frequency components.

The bolt on the disc is now removed to obtain a mechanically balanced motor and the experiment is repeated again with the same 3 Hz sinusoidal speed reference. The windowed Fourier ridges of the filtered current for this case are shown in Figure 7.13. The segment of the stator current analyzed in Figure 7.13 is selected to be similar to the one used in Figure 7.11. A fundamental component is again present in Figure 7.13 because of the reasons mentioned earlier. The disk, even without the bolt, comprises a slight unbalance by itself. This produces some fault harmonic frequencies even in the balanced rotor case, which are smaller than the case with a bolt on the disc, as shown previously in Figure 7.12.

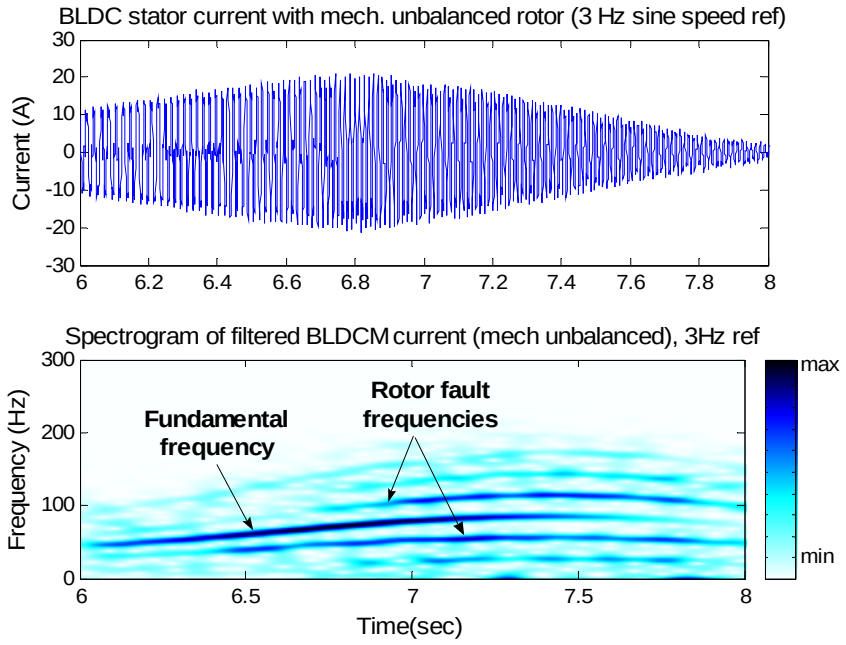

Figure 7.11: Non-stationary BLDC motor stator current and the spectrogram of the corresponding filtered BLDC motor (with mechanically unbalanced rotor) stator current with 3 Hz sine speed reference.

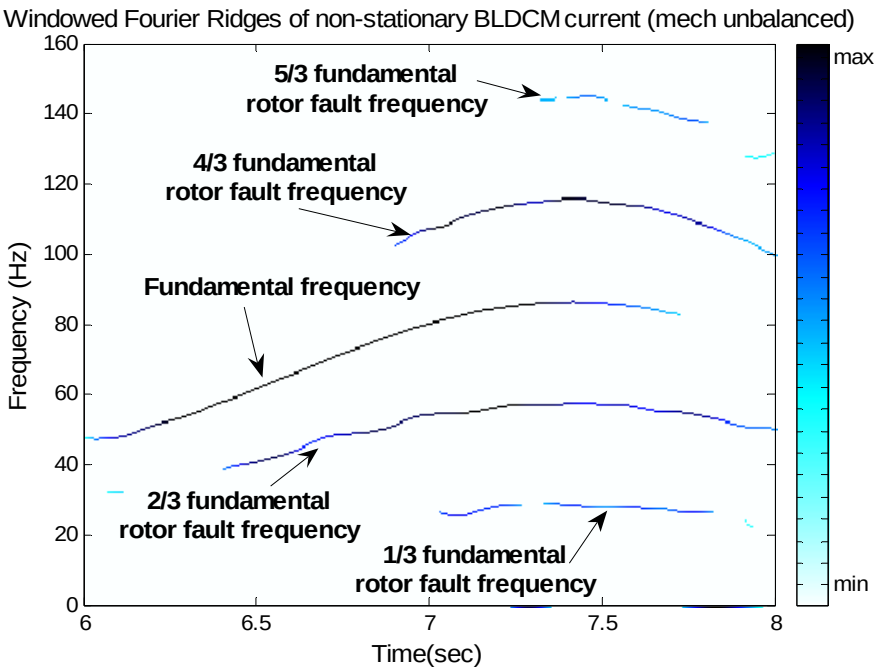

Figure 7.12: Windowed Fourier ridges of filtered BLDC motor (with mech. unbalanced rotor) stator current and 3 Hz sine speed reference.

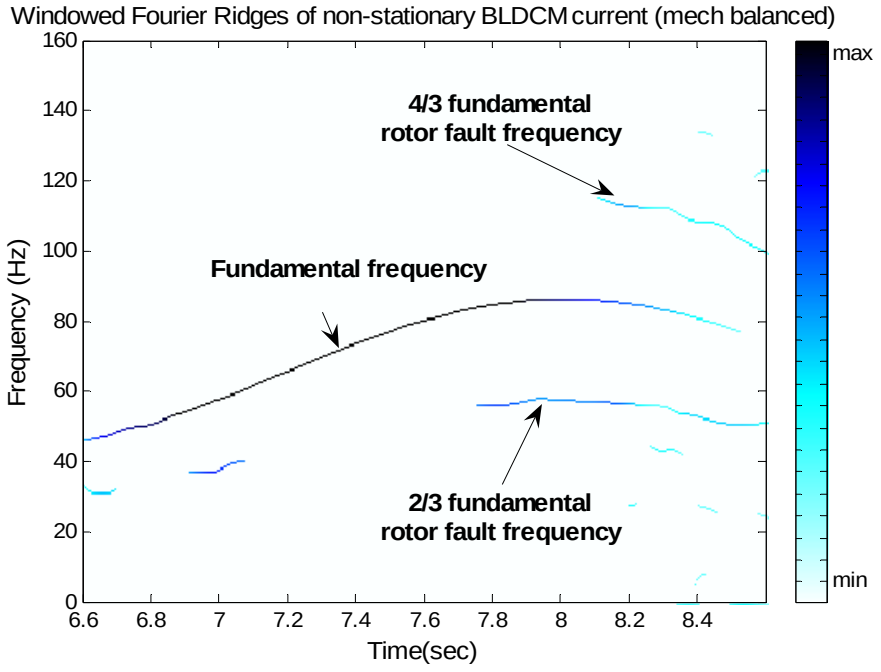

Figure 7.13: Windowed Fourier ridges of filtered BLDC motor (with mech. balanced rotor) stator current and 3 Hz sine speed reference.

7.7.2 Dynamic Eccentricity – 3 Hz And 6 Hz Sinusoidal Speed Reference

As mentioned earlier, in a dynamic eccentricity, the center of the rotor is not at the center of the stator and the position of minimum air gap rotates with the rotor. This misalignment may be caused by several factors such as misalignment of bearings, mechanical resonance at critical speeds, a bent rotor shaft, or wear of bearings. An actual dynamic eccentricity with the rotor moved by 32% of the air-gap length is implemented in the laboratory as explained in Chapter 4.

The stator current is again sampled at 2 kHz and the load conditions remain exactly the same, as in the previous experiment. The windowed Fourier ridges (instantaneous fault frequencies) of the filtered stator current of a motor with dynamic eccentricity and operating with a 3 Hz sinusoidal speed reference are shown in Figure 7.14. These Fourier ridges are extracted from the spectrogram of the filtered current signal using (7.3). The 56 dB ATF2 explained in detail in section 7.6 is now used in this experiment. The Fourier ridges in Figure 7.14 are determined to be the fault frequencies at $2/3^{rd}$ and $4/3^{rd}$ the fundamental frequency by comparing them with the Fourier ridge of the unfiltered signal that predominantly consists of only the fundamental component (Figure 7.15) as the fault frequencies are ignored as noise in relation to the fundamental component by the ridge algorithm. As the fundamental has been almost completely suppressed, the ridge algorithm detects and tracks only the fault frequencies. Again a Gaussian window of length 0.25 seconds is used in the experiments. The data is processed offline in MATLAB using the Wavelab802 toolbox. The fault frequencies are seen to be tracked over time. The windowed Fourier ridges for a faulty BLDC motor

operating with a 6 Hz sinusoidal speed reference is shown in Figure 7.16. Again, the fault frequencies are distinctly tracked over time.

7.7.3 Dynamic Eccentricity – 8 Hz Triangular Speed Reference

A triangular speed reference is also used in the experiments as a triangular speed variation causes more transient motor behavior than a sinusoidal speed reference which causes a smooth speed variation. Again, a Gaussian window of length 0.25 seconds is used to compute the Fourier ridges. The load condition remains the same as in the previous experiments. The windowed Fourier ridges for a faulty BLDC motor operating with an 8 Hz triangular speed reference is shown in Figure 7.17. The fault frequencies corresponding to a dynamic eccentricity can be seen to be distinctly tracked over time.

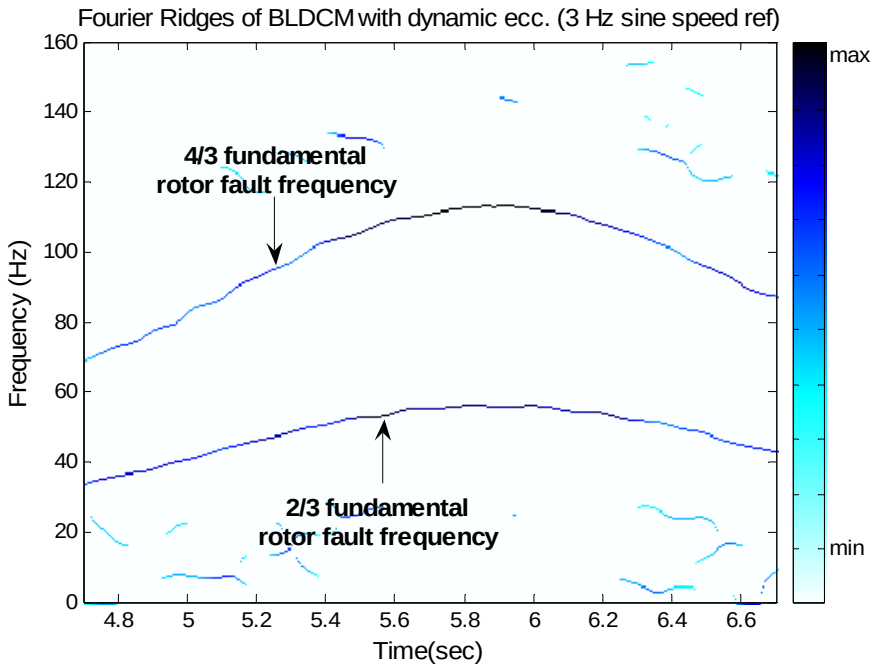

Figure 7.14: Windowed Fourier ridges of filtered BLDC motor (with dynamic eccentricity) stator current and 3 Hz sine speed reference.

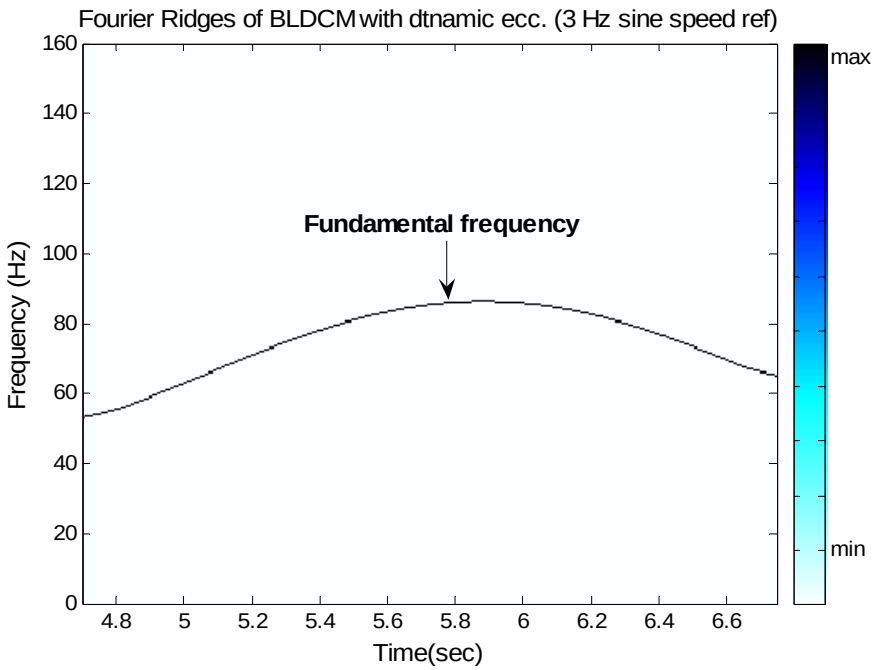

Figure 7.15: Windowed Fourier ridges of unfiltered BLDC motor (with dynamic eccentricity) stator current and 3 Hz sine speed reference.

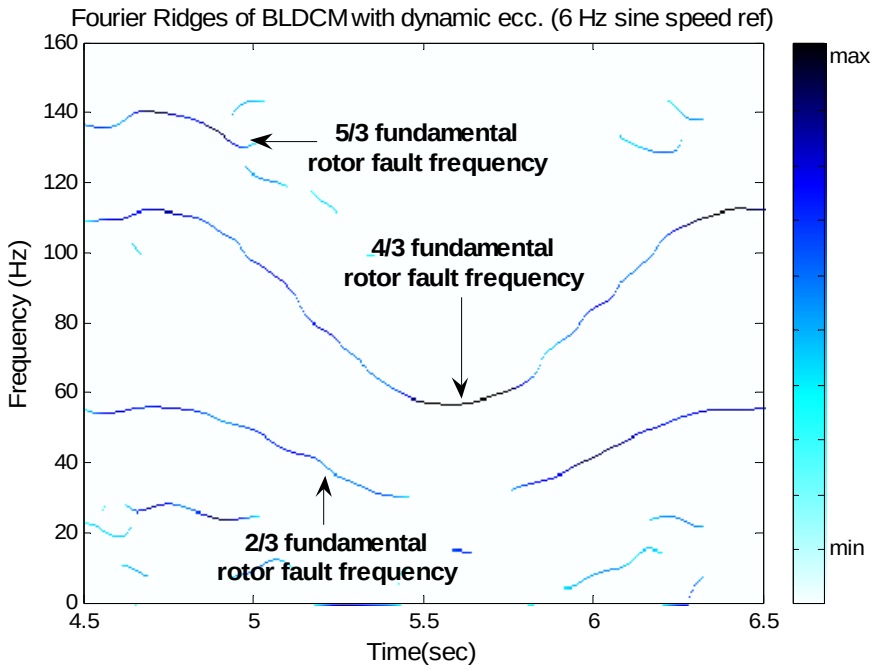

Figure 7.16: Windowed Fourier ridges of filtered BLDC motor (with dynamic eccentricity) stator current and 6 Hz sine speed reference.

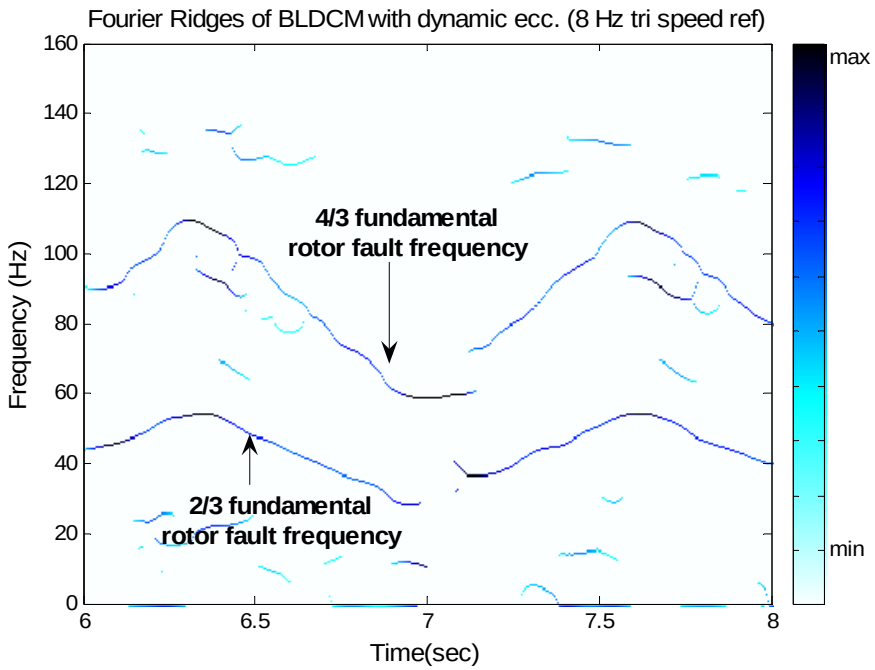

Figure 7.17: Windowed Fourier ridges of filtered BLDC motor (with dynamic eccentricity) stator current and 8 Hz triangular speed reference.

7.7.4 Dynamic Eccentricity – Random Speed Reference

To validate the effectiveness of the algorithm, the BLDC motor with dynamic eccentricity is now operated with a speed reference signal that changes randomly. Again the load conditions remain the same. The load on the motor is similar to the one used I the previous experiments. A Gaussian window of length 0.25 seconds is chosen to compute the windowed Fourier transform. The non-stationary stator current and the spectrogram of the filtered stator current, computed using (7.3), are shown in Figure 7.18. The spectrogram does not clearly depict the instantaneous fault frequencies in the filtered current signal. The windowed Fourier ridges (Figure 7.19) are then extracted from the local maxima of the spectrogram. Figure 7.19 shows that the fault frequencies are distinctly detected over time. The ridges in Figures 7.16, 7.17 and 7.19 are identified as

BLDC motor fault frequencies from the Fourier ridges of the corresponding unfiltered current waveforms as explained previously for the case of the 3 Hz sinusoidal speed variation. The random changes in the frequencies of the signal are now clearly visible in Figure 7.19. This demonstrates the effectiveness of the windowed Fourier ridge algorithm to track faults during all types of non-stationary conditions.

7.8 Comments on the Use of Windowed Fourier Ridges

7.8.1 Non-Stationarity Range of Operation

During the experiments, it is noted that the ridge algorithm is able to extract frequencies from the motor stator current up to a sinusoidal speed reference of 15 Hz and a triangular speed reference of 10 Hz. Beyond these speed reference rates, the current is

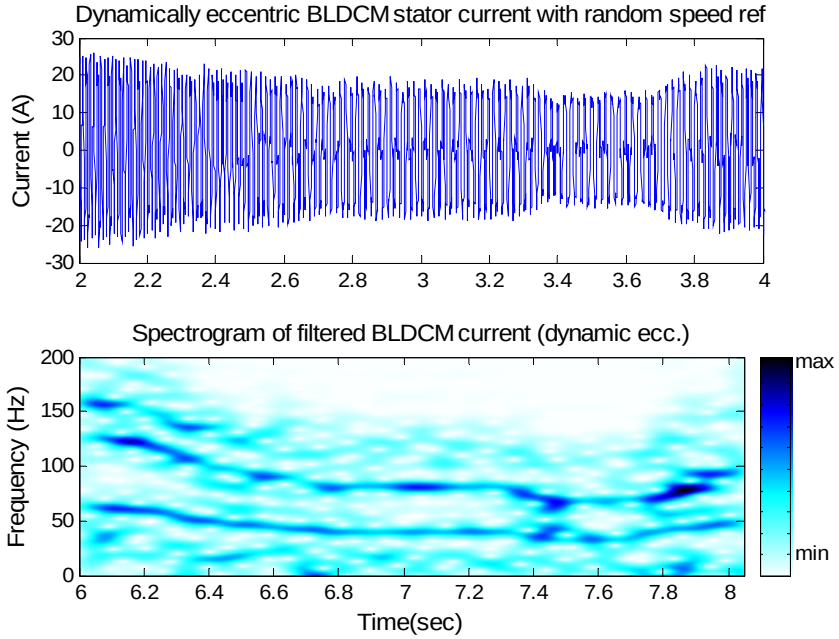

Figure 7.18: Non-stationary BLDC motor stator current and the spectrogram of the corresponding filtered BLDC motor (with dynamic eccentricity) stator current with random speed reference.

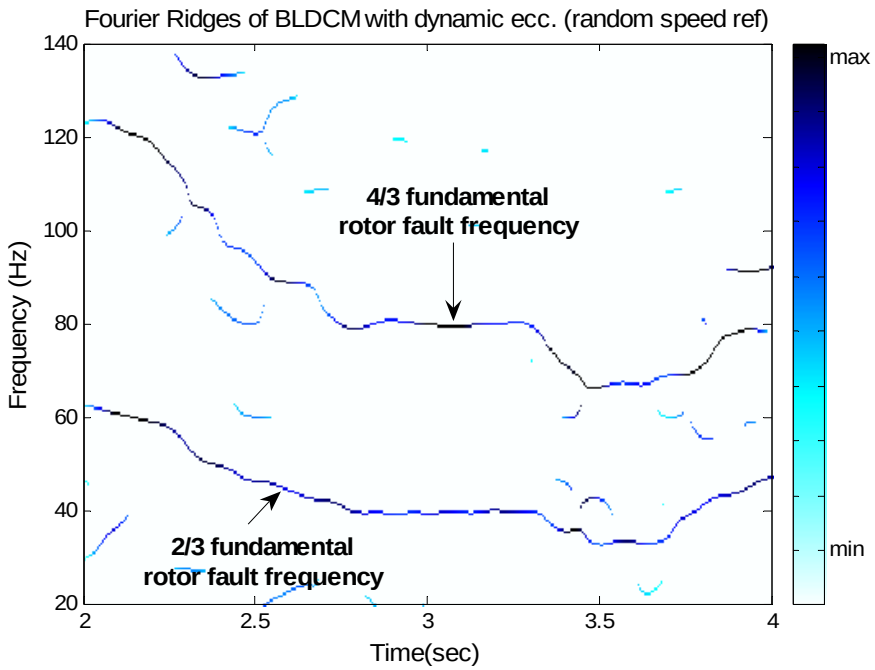

Figure 7.19: Windowed Fourier ridges of filtered BLDC motor (with dynamic eccentricity) stator current and random speed reference.

extremely non-stationary (especially with a triangular reference) and no longer possess any instantaneous frequency. However, such non-stationarity does not commonly occur in motor applications and any non-stationary fault-detection method based on the windowed. Another possible reason for the absence of frequency information in such extreme non-stationary signals could be the limitation on the slew rate of the PLL, which could result in the PLL not able to follow such dynamically changing frequencies. A commercial implementation of the Fourier ridge algorithm should take into account the severity of the non-stationary behavior that may be encountered.

7.8.2 Frequency Resolution, Sampling Frequency, and Window Length

The windowed Fourier ridge algorithm strongly depends on the size and type of window. At low frequencies, the frequency resolution may be poor because of the fixed

length of the window used in the algorithm. Hence the choice of length of the window is a critical aspect of the windowed Fourier ridge algorithm. The frequency resolution depends on the sampling frequency and on the amount of samples used for the transformation, that is, if the number of samples multiplied by the sampling frequency is 1 the frequency resolution is 1Hz, if the product is 2 the resolution is 0.5 Hz and so on. The sampling frequency and the number of samples are thus chosen as a trade-off between the desired frequency resolution for a particular diagnostics problem and the computational capability available with the digital signal processor (DSP).

The length of the chosen window is critical. For example, in this chapter, the Gaussian window length is chosen as 0.25 seconds. This window length depends on the desired frequency resolution, which in turn depends on the dynamic range of operation of the motor. The selection of this window length is a challenge. An initial length can be first chosen, and can then be adjusted to obtain the best time and frequency resolution depending on the non-stationarity encountered. A modified short-time Fourier transform with an adaptive window is also available in literature and can be used to improve the performance of the proposed algorithm [89]. However, this remains to be investigated.

7.8.3 Influence of Inverter Noise

The inverter switching frequency noise does not have an impact on the performance of the algorithm as this noise is more than a decade above the fundamental frequency, and is filtered out using the ATF prior to application of the algorithm.

7.9 Conclusions

The problem and solution to diagnosing rotor faults in BLDC motors operating under continuous non-stationary operation has been presented. The windowed Fourier

ridge algorithm is proposed as a novel solution. The windowed Fourier ridges are the local maxima computed from the spectrogram of a non-stationary signal. The Fourier ridges can be detected for maxima of comparable magnitude in multi-component signals. The method is not limited to BLDC motors but can be applied to other motors as well.

The ability of the method to track BLDC motor rotor faults such as unbalanced rotors and dynamic eccentricities in various cases of non-stationarity has been demonstrated. The windowed Fourier ridge algorithm unfortunately depends on the type and length of the data window as it has to be chosen as a trade off between time and frequency resolution. However, the method is simple to implement in real-time as will be shown in Chapter 10.

The WFT is a mathematically linear time-frequency distribution. The linearity can be seen in (7.1), where the Fourier transform is obtained from the product of the signal, *s(t)*, and the window, *g(t)*. There are also quadratic time-frequency distributions, where a second order function of the signal, *s(t)*, is used. These are not limited by restrictions of the window and are investigated as a possible alternative to the WFT in Chapter 8.

CHAPTER 8

NON-STATIONARY ROTOR FAULT DETECTION USING QUADRATIC TIME-FREQUENCY REPRESENTATIONS

While Chapter 7 successfully investigated the use of windowed Fourier transform (WFT) as a tool for motor fault detection in non-stationary operation, several significant issues impede its use in a variety of non-stationary operating environments. Foremost among its limitations, are its dependence on the size and the type of window used. This window is selected carefully to obtain a good time-frequency representation that can distinctly separate fault frequencies when the motor is operating at low speeds (low-frequency operation). While the WFT is a linear time-frequency representation (TFR), there is also available another class of quadratic time-frequency representations that are more suitable to non-stationary signal analysis. This chapter discusses some of these quadratic time-frequency representations as a possible enhancement to more accurate transient motor fault detection.

8.1 Generalized T-F Distributions

Time-frequency analysis is the three-dimensional time, frequency, and amplitude representation of a signal, which is inherently suited to indicate transient events in a signal. They thus combine time-domain and frequency-domain analysis to yield a more revealing picture of the temporal localization of a signal's spectral component. A special class of distributions, commonly referred to as Generalized Time Frequency distributions (GTFRDs) or members of the Cohen class have been recently reported in literature [64].

These distributions can be used for the analysis of non-stationary signals without any underlying assumptions. The Cohen class of distributions for a signal, *s(t)*, are given by

$$\rho(t,\omega) = \frac{1}{4\pi^2}\iiint e^{j\theta(u-t)}\chi(\theta,\tau)s^*\left(u-\frac{\tau}{2}\right)s\left(u+\frac{\tau}{2}\right)e^{-j\omega\tau}d\theta du d\tau\,, \tag{8.1}$$

where $\chi(\theta,\tau)$ is an arbitrary function called the kernel. Setting the kernel $\chi(\theta,\tau) = 1$ yields the well-known Wigner-Ville distribution. Table 8.1 lists some commonly used TFRs and their respective kernels, where $h(\tau)$ is a time window (Gaussian, Hamming,…). Equation (8.1) is called a quadratic TFR as a result of the second order time-shifted product of the signal, *s(t)*, with itself. However, the biggest drawback of quadratic distributions such as the WVD is the introduction of non-negligible cross-term artifacts in the time-frequency plot of the signal. The cross-term can be suppressed by using more complicated kernels such as the PWVD (Pseudo WVD), the CWD (Choi-Williams distribution), or the ZAM (Zhao-Atlas-Marks distribution), but at the cost of frequency resolution. These issues are explained for each of these distributions in detail in the following sections of this chapter.

8.2 Wigner-Ville Distributions (WVD) and Its Variants

The Wigner distribution and its various permutations is an analysis technique that has been widely used in the diagnostics of faults in mechanical systems, the most common being the gear train. The Wigner-Ville distribution (WVD) is derived by generalizing the relationship between the power spectrum and the autocorrelation function for non-stationary time-variant processes. The Wigner-Ville distribution of a signal, *s(t)*, is given by [64, 90, 91]

$$W(t,\omega)=\frac{1}{2\pi}\int_{-\infty}^{\infty}e^{-j\omega\tau}s^{*}\left(t-\frac{\tau}{2}\right)s\left(t+\frac{\tau}{2}\right)d\tau\,, \tag{8.2}$$

where s^* is the conjugate of $s(t)$, t is the fixed time of interest, τ is the "running time" and ω is the angular frequency (corresponding to $\omega=2\pi f$ where f is the instantaneous frequency). The frequency ω is similar to the instantaneous frequency ξ of Chapter 7, but has been given a different symbol to differentiate the fact that ξ is obtained from the positive phase derivative. The WVD is a high-resolution technique that offers much better frequency resolution than the STFT [65]. Moreover, the distribution can be used for the analysis of non-stationary signals without any underlying assumptions [65].

Table 8.1: Selected TFRs and their kernels

TFR	**Kernel: $\chi(\theta,\tau)$**
WVD	1
PWVD (Windowed WVD)	$h(\tau)$
CWD	$e^{-\theta^2\tau^2}/\sigma$
ZAM	$\frac{\sin\left(2\pi\theta\lvert\tau\rvert/a\right)}{\pi\theta};\ a=1$
Spectrogram	$\int h^{*}\left(u-\frac{\tau}{2}\right)e^{j2\pi\theta u}h\left(u+\frac{\tau}{2}\right)du$

The WVD is a bi-quadratic distribution that produces large undesirable frequency components called cross-terms that can hamper the interpretation of the distribution. To elaborate on this, a signal, *s(t)*, that is a sum of two sinusoids is considered [65],

$$s(t) = A_1 e^{j2p_1 t} + A_2 e^{j2\pi p_2 t}, \tag{8.3}$$

where A_1 and A_2 are the amplitudes of two sinusoids with frequencies p_1 and p_2 respectively. The WVD of (8.3) derived using (8.2) is [65]

$$\begin{aligned} W(t,p) = {} & A_1^2 \delta(p - p_1) + A_2^2 \delta(p - p_2) \\ & + 2A_1 A_2 \delta\left(p - \frac{1}{2}(p_1 + p_2)\right) \cos\left(2\pi(p_2 - p_1)t\right) \end{aligned}. \tag{8.4}$$

Thus, the WVD of the sum of two signals is not only the sum of the WVD of each individual signal, but there also exists an extra term at the frequency ½(p_1 + p_2). This extra term is called the "cross-term".

Ghosts and artifacts are also produced. However, they are usually smaller in magnitude and can be removed by thresholding. The cross-terms on the other hand are significantly larger in amplitude when compared to the actual spectral components (also called as auto-terms) in the signal. Several variants of the WVD that attempt to suppress these cross-terms and the two prominent ones are

1. Pseudo-Wigner Ville distribution (PWVD) or the Windowed Wigner distribution, and
2. Smoothed Pseudo Wigner-Ville distribution (SPWVD).

The PWVD is the windowed version of the Wigner-Ville distribution. The PWVD may be defined in the time domain or in the frequency domain, though the former

is more common. The PWVD has a much better resolution than the STFT [65] and is defined in (8.5), where $h(\tau)$ is the time smoothing window.

$$W_P(t,\omega) = \frac{1}{2\pi}\int_{-\infty}^{\infty} e^{-j\omega\tau} h(\tau) s^*\left(t-\frac{\tau}{2}\right) s\left(t+\frac{\tau}{2}\right) d\tau\,, \tag{8.5}$$

The smoothed WVD (SPWVD) uses a function that smoothes the distribution in both the time and frequency planes. The SPWVD offers better cross-term suppression than the PWVD, though at the cost of frequency resolution and is given by [64]

$$W_S(t,\omega) = \int_{-\infty}^{\infty} L(t-t',\omega-\omega') W(t',\omega')\, dt' d\omega'\,, \tag{8.6}$$

where L is the chosen smoothing window (usually Gaussian) applied to the Wigner-Ville distribution $W(t,\omega)$. t' and ω' are time and frequency variables respectively over which the smoothing is carried out. The most commonly used smoothing function used is a Gaussian function,

$$L(t,\omega) = \frac{1}{\alpha\beta} e^{-\frac{t^2}{\alpha}-\frac{\omega^2}{\beta}}\,, \tag{8.7}$$

and it has been known in quantum literature that for certain values of α and β, a positive distribution is obtained with many of the artifacts suppressed [64]. The condition to be satisfied is that

$$\alpha\beta \geq 1. \tag{8.8}$$

Other general windows such as the Hamming window also produce a good time-frequency resolution that is similar to the Gaussian window.

8.3 Choi-Williams Distributions (CWD)

The CWD is an exponential kernel that effectively suppresses cross-terms, and the kernel is given in Table 8.1 where the parameter σ determines the trade-off between the cross-term suppression and the frequency resolution [92]. A larger suppression of the cross-term results in a poorer frequency resolution, which is still better than that of the WVD and its variants [65]. Unlike the spectrogram (WFT), windows play no fundamental role here, and are required only because signals have limited durations.

If σ is taken to be large, then the kernel is effectively one and results in the WVD. A smaller σ on the other hand enhances the actual frequency components in the signal (also termed as auto-terms) while suppressing the cross terms. However, Choi and Williams have proved that there is some loss of frequency resolution in the auto terms when the value of σ becomes small (<0.1) [92].

8.4 Zhao-Atlas-Marks Distributions (ZAM)

The ZAM distribution is a relatively new distribution [93]. While the emphasis on development of distributions such as the CWD is to meet marginal conditions and other properties that usually characterize the quadratic TFRs [66], the development of the ZAM "cone-kernel' is aimed at introducing finite time-support and reducing the cross-terms [93]. The kernel to be used in (8.1) to obtain a ZAM distribution is

$$\chi(\theta,\tau) = \chi_1(\tau)\frac{\sin\left(2\pi\theta|\tau|/a\right)}{\pi\theta}, \tag{8.9}$$

where $\chi_1(\tau)$ is a function to be specified (usually taken to be equal to one) and a is greater than or equal to two.

8.5 Comparison of Various TFRs

A hypothetical test signal, i_a, approximating a rotor fault scenario and having a fundamental of amplitude 0.05 A (corresponding to a filtered stator current) with two rotor fault sidebands of amplitude 0.07 A is generated using (8.10). The three frequencies in (8.8) are the fundamental frequency *p(t)* and the two rotor fault frequencies at 2/3rd and 4/3rd of the fundamental frequency *p(t)*.

$$i_a = 0.05\cos\left(2\pi p(t)t\right) + 0.07\cos\left(4\pi p(t)t/3\right) + 0.07\cos\left(8\pi p(t)t/3\right). \quad (8.10)$$

The amplitudes in (8.10) are chosen arbitrarily to imitate a rotor fault scenario as close as possible. The frequency, *p(t)*, is varied sinusoidally between 0 and 120 Hz. The window, *h(τ)*, of the spectrogram in Table 8.1 is chosen as a Gaussian window of length 0.25 seconds. A one second record with 2048 samples is used for comparing the various TFRs.

Figure 8.1 shows the two-dimensional time-frequency plot of the spectrogram (WFT) of the test signal computed using (8.10). The time-frequency (t-f) plot of Figure 8.1 describes the variation of the three frequencies (y-axis) in the signal i_a over time (x-axis).The rotor fault frequencies at 2/3rd and 4/3rd of the fundamental frequency, along with the fundamental itself, are seen to be distinctly tracked over time in Figure 8.1, except in the low frequency region of 0 to 50 Hz. The frequency resolution is reduced at low frequencies and this is expected as a result of the relatively short window length. The Rice University Time-Frequency Analysis toolbox [94] for MATLAB is used to compute the Wigner distributions for the simulated motor current signal. This toolbox has specific functions tailor-made for time-frequency analysis.

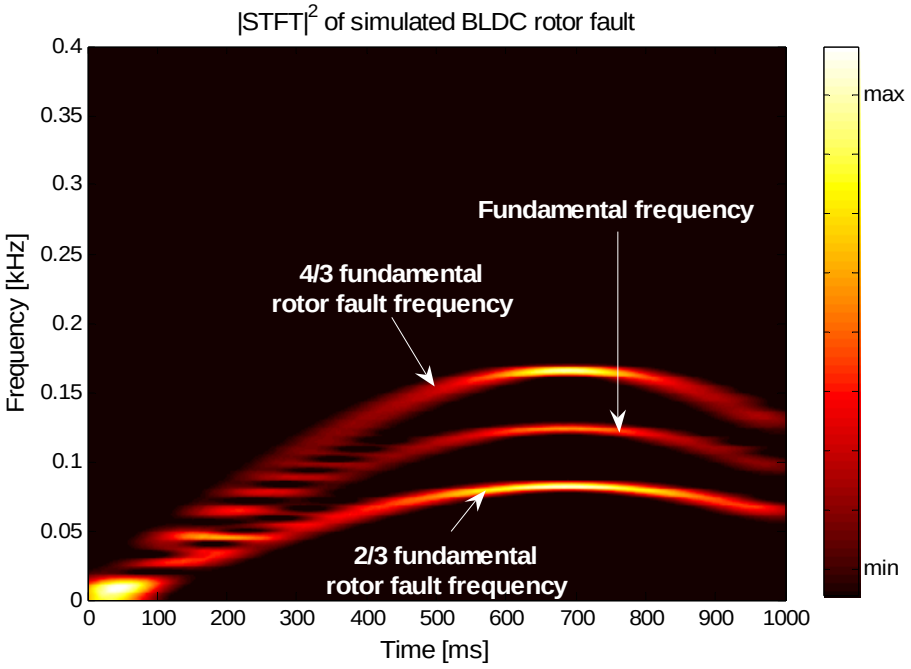

Figure 8.1: WFT of a simulated BLDC rotor fault using a hypothetical test signal i_a.

However, two significant problems arise when applying the WVD or its variants to diagnose rotor faults in BLDC motors:

1. Interaction between the fundamental frequency and the fault frequencies in (8.8) produce cross-terms at the same values as some fault frequencies produced by (3.10). These cross-terms may be difficult to suppress even using the PWVD or the SPWVD. This is because of large cross-terms that arise resulting from the fundamental frequency that is several orders of magnitude larger than the fault components.
2. The WVD spectrum of a real-valued signal has both a positive and a negative frequency part in the WVD spectrum and this produces cross-terms between the negative and the positive frequencies. The stator current being a real-valued signal, suffers from this problem. These cross-terms can be eliminated by eliminating the negative-frequency terms.

The problem of reducing cross-terms can be solved by adaptively filtering the fundamental and other inverter harmonics. In motors with large numbers of poles, certain harmonics may be selectively filtered (using an adaptive comb filter) prior to any signal processing. Thus, the cross-terms that may occur at the motor fault frequencies can be avoided. The PWVD or the SPWVD can then be used to suppress any remaining cross-terms that are produced as a result of the interaction with the filtered fundamental component.

The negative-frequency terms that are mentioned in (2) as well as other artifacts can be removed by converting the real-valued signal to an analytic version of the same. This transformation is done using the Hilbert transform. The use of the analytic signal also eliminates the need to sample the signal at twice the Nyquist rate [65]. The analytic signal of a real-valued signal, *s(t)*, can be defined as

$$s_A(t) = s(t) + js_H(t), \tag{8.11}$$

where $s_H(t)$ is the Hilbert transform of the signal, *s(t)*, and is given by

$$H\left[s(t)\right] = s_H(t) = \frac{1}{\pi}\int_{-\infty}^{\infty} s(\tau)\frac{1}{t-\tau}d\tau\,. \tag{8.12}$$

The Fourier transform, $S_A(f)$, of the analytic signal in (8.11) does not possess negative-frequency components as can be seen from (8.13), where *S(f)* is the Fourier transform of *s(t)* and $S_H(f)$ is the Fourier transform of $s_H(t)$.

$$S_A(f) = S(f) + jS_H(f) = S(f) + \text{sgn}\, f \; S(f)$$
$$= \begin{cases} 0, & if \;\; f \langle 0 \\ S(f), & if \; f = 0 \\ 2S(f), & if \;\; f \rangle 0 \end{cases} \tag{8.13}$$

Figure 8.2 is a t-f plot that shows the WVD of the signal of (8.10), obtained using (8.2). The PWVD and the SPWVD of the signal of (8.10) obtained using (8.5) and (8.6) respectively, are shown in the t-f plots of Figures 8.3 and 8.4. The t-f plots show the variation of the multiple frequency components of the signal, i_a, over time. A Gaussian window of length 0.25 seconds is again used for both the PWVD and the SPWVD to facilitate a fair comparison with the WFT. The WVD, the PWVD, and the SPWVD are calculated for the analytic version of the real-valued motor current signal. The analytic signal is obtained from the real-valued current signal, i_a, in (8.10) using (8.11) and (8.12). It can be seen from Figures 8.1 and 8.2 that the WVD provides better frequency resolution than the WFT at lower frequencies, but suffers from a large number of ghosts and artifacts. The PWVD (Figure 8.3) of the Hilbert transformed signal shows that much of the interference is removed, thus offering excellent tracking of the fault signals. Nevertheless, some cross-terms are still present.

On the other hand, the SPWVD in Figure 8.4 offers almost complete suppression of cross-terms while still offering better frequency resolution than the WFT of Figure 8.1. Figure 8.1 also shows that the spectral components produced by the WFT are smeared in the frequency domain. Hence the fault frequencies are not localized but spread over a frequency range. The PWVD and the SPWVD t-f plots in Figures 8.3 and 8.4 show a much better concentration of energy in the frequency domain. This allows the PWVD

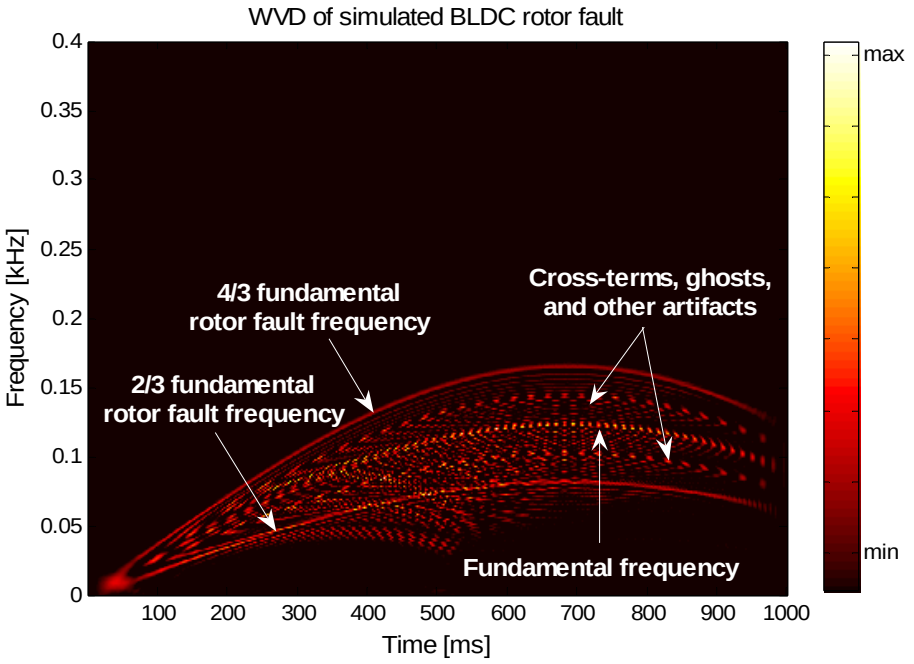

Figure 8.2: WVD of a simulated BLDC rotor fault using a hypothetical test signal i_a.

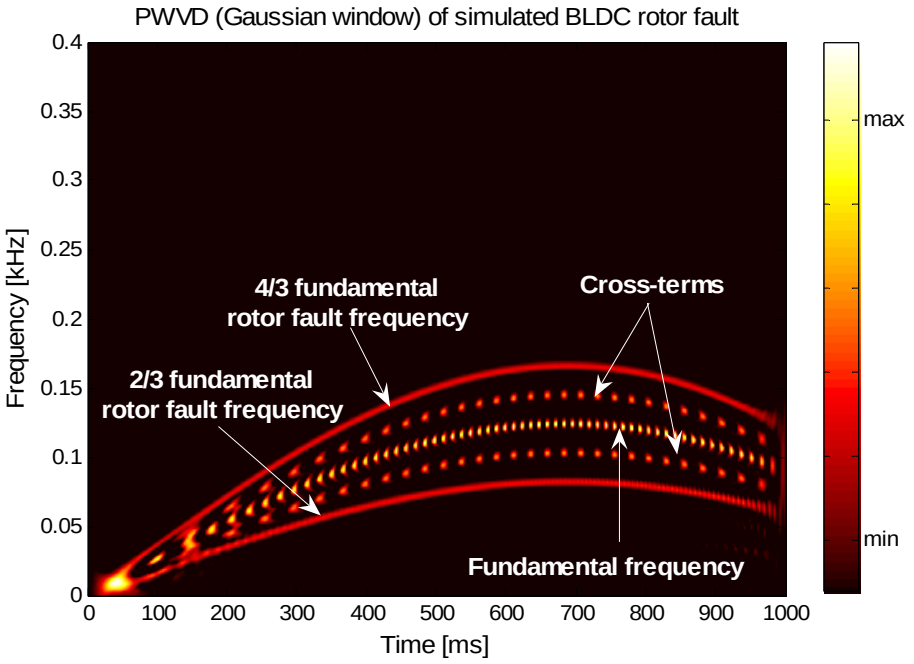

Figure 8.3: PWVD of a simulated BLDC rotor fault using a hypothetical test signal i_a.

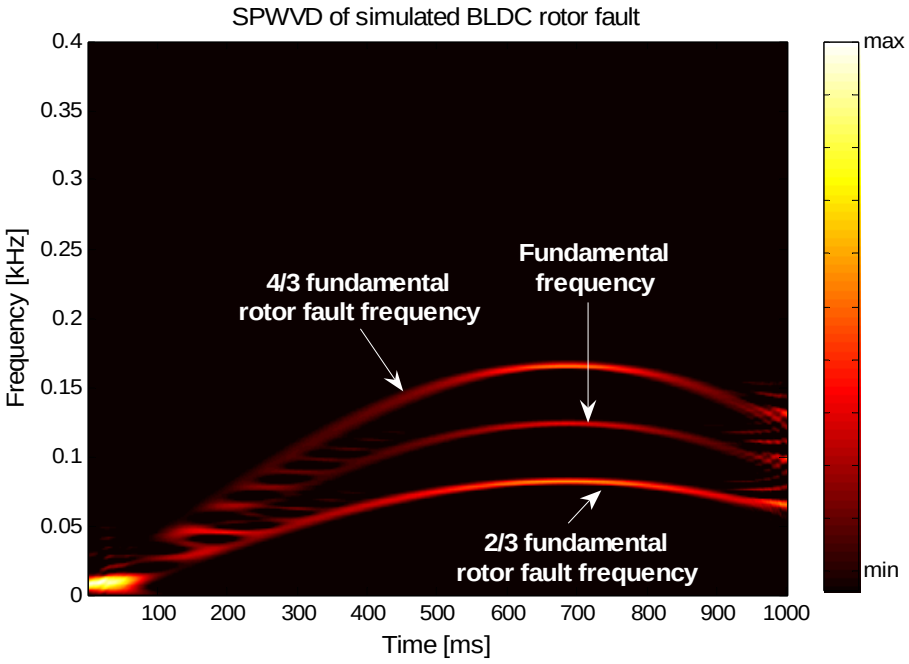

Figure 8.4: SPWVD of a simulated BLDC rotor fault using a hypothetical test signal i_a.

and the SPWVD to provide more accurate indication of the fault harmonic amplitudes, when compared to the WFT.

Similarly, the t-f plots of a CWD and a ZAM distribution for the signal of (8.10) are shown in Figures 8.5 and 8.6. Again, the signal of (8.10) is Hilbert transformed into an analytic signal prior to the application of the CWD and the ZAM distributions. The CWD in Figure 8.5 (σ =1) has better energy concentration than the STFT, but the frequency resolution in the low-frequency region (below 50 Hz) is compromised to obtain good cross-term suppression. This performance of the CWD is therefore similar to that of the SPWVD. However, the ZAM distribution in Figure 8.6 shows a strong energy concentration (low frequency smear), excellent cross-term suppression, and a good frequency resolution, all of which are better than even the SPWVD.

8.6 Proposed Fault-Detection Algorithm based on Quadratic TFRs

The previous sections have demonstrated that quadratic time-frequency distributions are suitable for non-stationary fault diagnostics, and even offer superior frequency resolution and energy concentration than the WFT. A quadratic TFR based fault-detection algorithm is now proposed to detect rotor faults in BLDC motors that operate under non-stationary conditions.

A block diagram of the proposed scheme is shown in Figure 8.7. The acquired BLDC stator current is first filtered adaptively to remove the fundamental frequency and other inverter harmonics. This filtering serves two purposes. Firstly, the filtering removes the fundamental and all inverter harmonics which are several orders in magnitude larger than the fault frequency components. Secondly, the removal of all unwanted harmonics decreases the number and magnitude of the cross terms and other artifacts that are typically created by quadratic TFRs. The filtering thus helps the TFRs to create a clean time-frequency representation of the BLDC motor current signal.

The filtered stator current is then converted into an analytic signal using the Hilbert transformation explained in the previous section. The analytic signal further improves the time-frequency representation of the BLDC motor current signal by removing negative-frequency components and its associated cross-terms. This is done by calculating the Hilbert transform of the motor current signal using (8.12). This term is phase shifted by 90 degrees and added on to the original signal as in (8.11) to create the analytic signal.

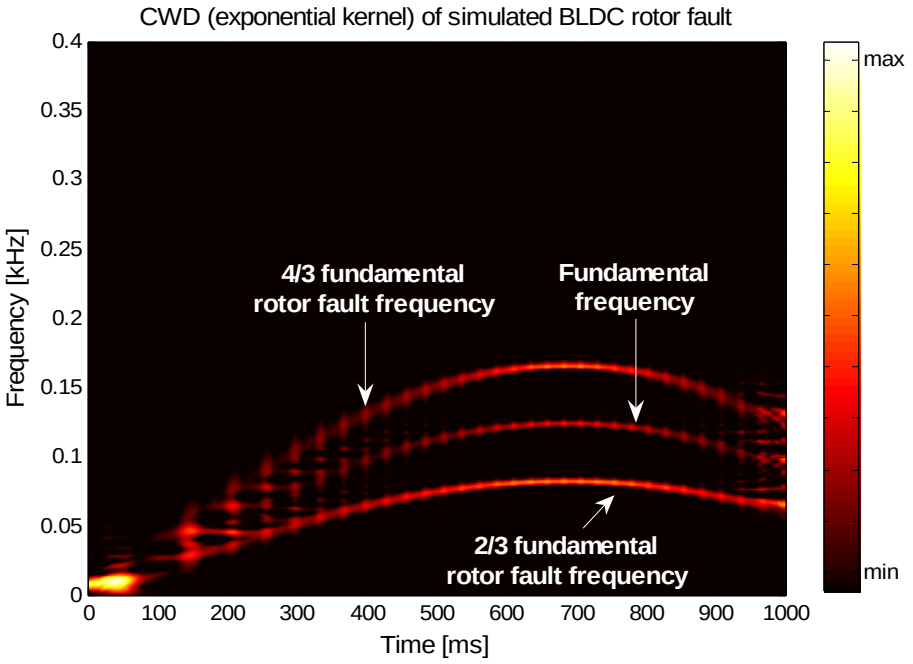

Figure 8.5: CWD of a simulated BLDC rotor fault using a hypothetical test signal i_a.

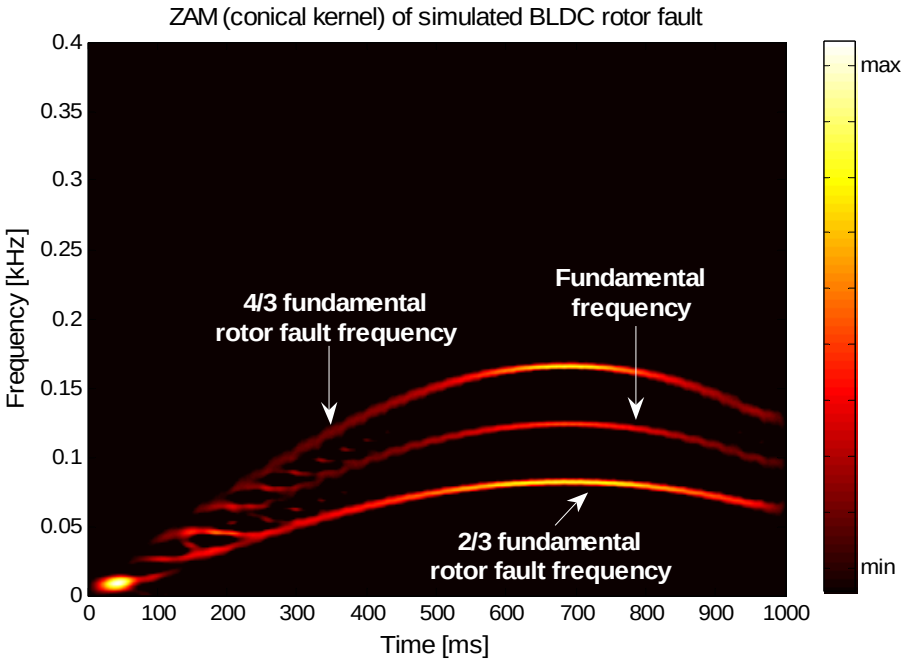

Figure 8.6: ZAM of a simulated BLDC rotor fault using a hypothetical test signal i_a.

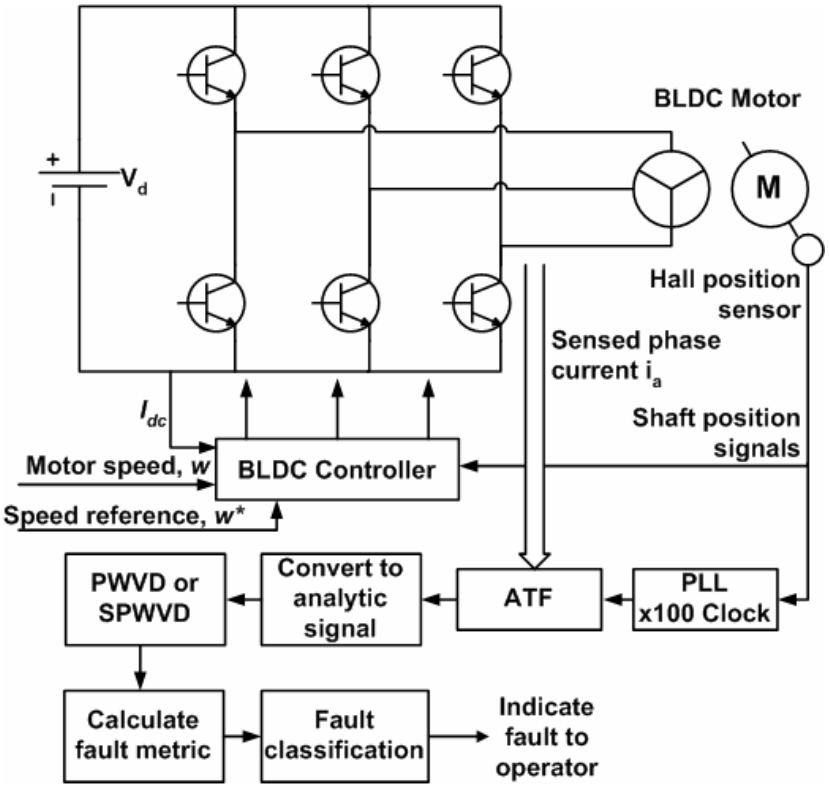

Figure 8.7: Quadratic TFR based BLDC rotor fault detection.

The TFR is then calculated for a time-slice of predetermined length using any of the kernels shown in Table 8.1. In the case of an SPWVD, for example, (8.4) is used to calculate the time-frequency representation of the filtered analytic BLDC stator current. The fault frequencies obtained from the TFR calculation are then used to compute a fault metric that indicates the health of the motor. The non-stationary motor operation is implemented as explained in section 7.5 of Chapter 7.

8.7 Experimental Results

The proposed fault-detection algorithm is implemented on a motor with a dynamic eccentricity as in Chapter 7. This motor has its rotor displaced from the center by 32% of the air-gap length. The stator current of the motor is again sampled at 2 kHz

after being filtered using the adaptive tracking filter ATF2. A DC generator is used in the load similar to the experiments in Chapter 7. This provides dynamic load, where the load torque on the BLDC motor changes directly in proportion to the instantaneous motor speed. An SPWVD/CWD is then calculated for the analytic signal using pre-built MATLAB functions available as part of the Rice University Time Frequency Analysis toolbox [94]. A color chart is provided in all the t-f plots that depicts the relative magnitude of the amplitude of the frequency components. The length of the data sample is usually a power of two, to facilitate fast computation [94]. In the experiments, a data comprising of 4096 (2^{12}) samples is used. Both the SPWVD/CWD is computed with a Hamming window as the smoothing functions. The length of the time-smoothing Hamming window is 411 samples and the length of the frequency smoothing Hamming window is 513 samples. These lengths are determined through trial and error to obtain the best possible time-frequency representation.

8.7.1 Dynamic Eccentricity Detection Using SPWVD – 5 Hz Sinusoidal Speed Reference

Figure 8.8 shows the t-f plot of the SPWVD of the analytic filtered stator current of a dynamically eccentric motor operating with a 5 Hz sinusoidal speed reference rate ($f_{ref} = 5$ in (7.8)). The two dynamic eccentricity fault frequencies at 2/3rd and 4/3rd the fundamental frequency are tracked over time, indicating excellent frequency tracking with all cross-terms suppressed. The fundamental is completely absent because of the high attenuation of the ATF2. A relative comparison of the magnitude of the harmonics can be assessed from the color chart provided in the t-f plot.

8.7.2 Dynamic Eccentricity Detection Using ZAM – 5 Hz Triangular Speed Reference

Figure 8.9 shows the ZAM distribution of the filtered stator current of the same dynamically eccentric BLDC motor, now operating with a 5 Hz triangular speed reference. Again, the ZAM distribution tracks the fault frequencies distinctly over time. Unlike the WFT, no assumption of local stationarity is needed for the SPWVD and ZAM distributions. These distributions are inherently suited for analyzing non-stationary signals, and do not suffer from the problems of window type and size as in the WFT. The amplitude of the extracted fault frequencies can be monitored to detect the severity of a rotor fault.

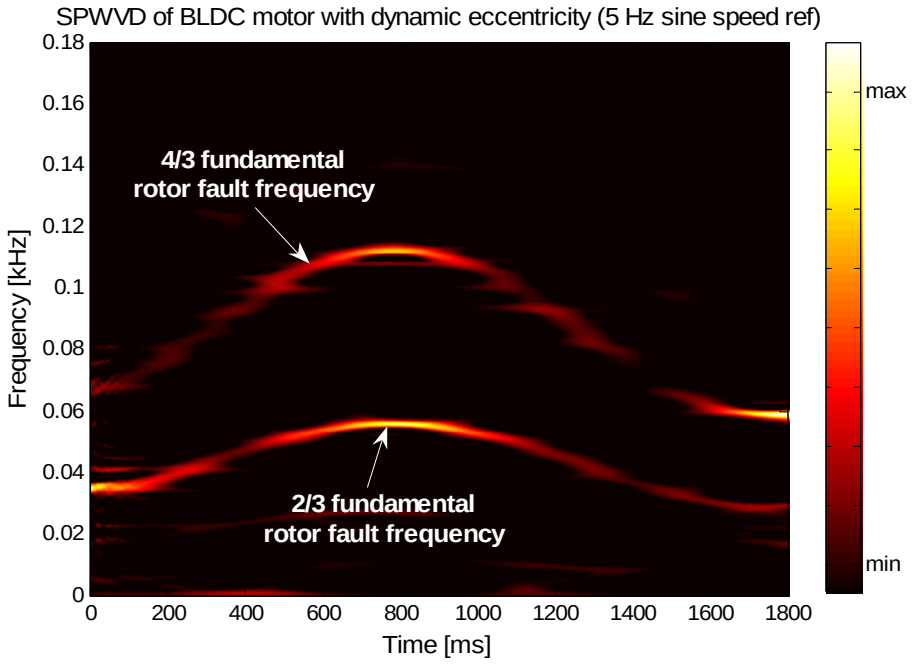

Figure 8.8: SPWVD of BLDC motor with dynamic eccentricity (5 Hz sinusoidal speed reference).

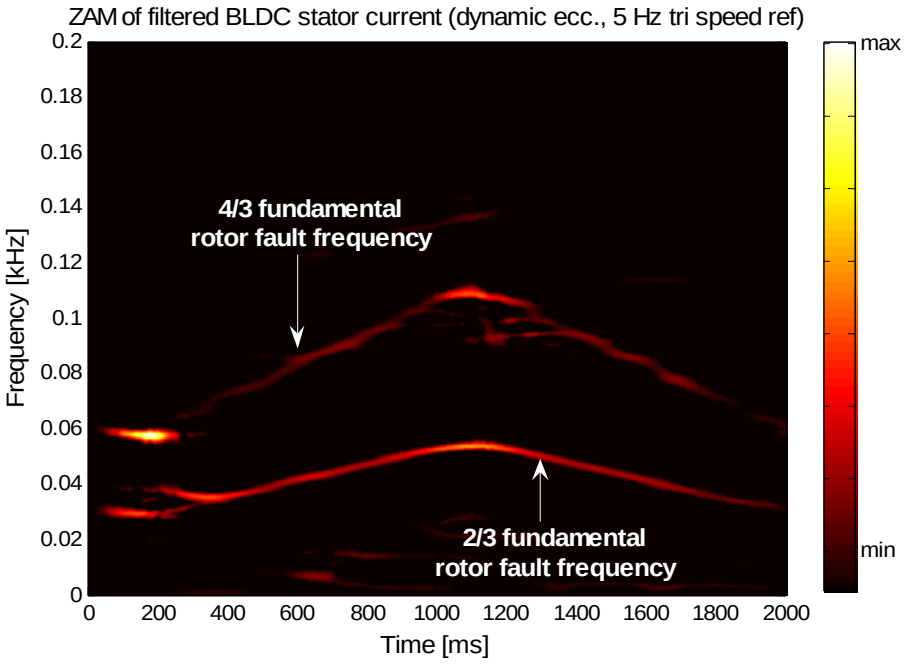

Figure 8.9: ZAM of filtered BLDC motor (with dynamic eccentricity) stator current and 5 Hz triangular speed reference.

8.8 Conclusions

The use of time-frequency distributions is suggested as an improved alternative to the windowed Fourier ridges, for the tracking of rotor faults in electric motors operating under continuous non-stationary conditions. It is again assumed that the BLDC stator current may contain unique fault frequency components that can identify the type of rotor defect. The quadratic TFRs provide much better frequency resolution and localization of energy than linear TFRs like the WFT. The ZAM distribution exhibits the best performance. The cross-terms and other artifacts can be suppressed by selective prefiltering of the current, and using the Hilbert transformed version of the real-valued stator current signal.

However, the need to provide high frequency resolution along with good cross-term suppression leads to complicated kernels, requiring large amounts of processing power as will be shown later in Chapter 10. The biggest advantage of using quadratic TFRs is their non-dependence on any window function, which on the other hand is one of the biggest limitations of the WFT. The use of time-scale methods for non-stationary motor fault detection will be explored next in Chapter 9.

CHAPTER 9

NON-STATIONARY ROTOR FAULT DETECTION USING ANALYTIC WAVELET TRANSFORMS

While Chapters 7 and 8 investigated the use of time-frequency distributions, the possibility of using wavelets for motor fault detection in non-stationary operating conditions is explored in this chapter. The challenges in using the wavelets for motor fault detection are investigated. A novel Analytic Wavelet Transform (AWT) based detector for tracking the rotor faults such as dynamic eccentricity in BLDC motors is proposed. The proposed method extracts the rotor fault frequencies from the stator current of the BLDC motor using the AWT. A ridge detector is then applied to track the maxima of the wavelet-extracted fault frequencies over time, thus providing a method to detect rotor faults in motors operating under dynamic conditions.

9.1 Introduction to Wavelets

In wavelet analysis, a signal is analyzed at different scales or resolutions: a large window is used to look at the approximate stationarity of the signal and a small window is simultaneously used to look for transients. This multi-resolution or multi-scale view of the signal is the essence of wavelet analysis [67]. The wavelet analysis is performed using a single prototype function called a wavelet. This function is analogous to the sine function used in Fourier transforms, but is structured to suit transient applications. Fine temporal analysis is performed using the compressed version (high-frequency) of the wavelet, while fine frequency analysis uses dilated versions (low-frequency) of the

wavelet [67]. The wavelet transform decomposes signals using scaled and translated (time-shifted) wavelets. A wavelet is a function ψ with a zero average [68]

$$\int_{-\infty}^{+\infty} \psi(\tau)\, d\tau = 0 . \tag{9.1}$$

It is normalized $||\psi|| = 1$, and centered in the neighborhood of $\tau = 0$. A family of time-frequency atoms is obtained by scaling ψ by m and translating it by t:

$$\psi_{t,m}(\tau) = \frac{1}{\sqrt{m}} \psi\left(\frac{\tau - t}{m}\right), \tag{9.2}$$

The wavelet transform of a signal *s(t)* at time t and scale m is given by

$$Wf(t,m) = \left\langle s, \psi_{t,m} \right\rangle = \int_{-\infty}^{+\infty} s(\tau) \frac{1}{\sqrt{m}} \psi^*\left(\frac{\tau - t}{m}\right) d\tau , \tag{9.3}$$

The energy density of the signal is represented by the scalogram, $P_W f$, given by [68]

$$P_W f(t,\xi) = \left| Wf(t,m) \right|^2 , \tag{9.4}$$

where $\xi = \eta/m$ is the center frequency of the scaled wavelet, $\psi_{t,m}$, and η is the center frequency of the original mother wavelet, ψ.

9.2 Choice of Wavelet

Choosing an appropriate wavelet is similar to choosing a window in the STFT. A real wavelet does not possess separate phase information, and hence, is suitable only for detecting sharp transients [68]. However, a complex analytic wavelet can separate amplitude and phase components from a signal, and is commonly used to measure the

instantaneous frequencies [69]. As measurement of the instantaneous frequency is a critical aspect of the proposed fault-detection algorithm, the analytic wavelet is chosen for this application. An analytic wavelet, $\psi(\tau)$, can be constructed by modulating the frequency ($exp(i\eta\tau)$) with a real and symmetric window, $g(\tau)$

$$\psi(\tau) = g(\tau) e^{i\eta\tau}. \tag{9.5}$$

In addition, the fault frequency is not an impulse shaped signal, but is spread over the sample window. Hence, sharp wavelets such as the Daubechies that are more suited to pick up sharp transients, will not be able to pick up rotor fault frequencies that are spread throughout the signal. A smoother window that can approximate the spread of the fault frequency in the current signal has to be chosen.

A common smooth analytic wavelet is the Gabor wavelet. It is obtained by frequency modulating a Gaussian window, $g(\tau)$

$$g(\tau) = \frac{1}{\left(\sigma^2\pi\right)^{1/4}} e^{-\frac{\tau^2}{2\sigma^2}}, \tag{9.6}$$

where σ^2 is the variance. The Fourier transform of this window is

$$\hat{g}(\omega) = \left(4\pi\sigma^2\right)^{1/4} e^{-\frac{\sigma^2\omega^2}{2}}, \tag{9.7}$$

where ω is the instantaneous frequency. If $\sigma^2\eta^2 \gg 1$ then $\hat{g}(\omega) \sim 0$ for $|\omega| > \eta$. Such Gabor wavelets are thus considered to be approximately analytic [68].

9.3 Analytic Wavelet Ridges

An AWT is calculated by using an analytic wavelet, ψ, in (9.5). Such an analytic wavelet could be the Gabor wavelet explained in the previous section. Its time-frequency resolution depends on the time-frequency spread of the wavelet atoms, $\psi_{t,m}$.

The instantaneous frequencies in the signal, *s*, are measured from the ridges (local maxima) of the normalized form of the scalogram, $P_W f$, computed using the analytic wavelet. The instantaneous frequency is defined as a positive derivative, $\varphi'(t)$, of the phase, $\varphi(t)$, of the respective spectral component. The normalized scalogram is

$$\frac{\xi}{\eta} P_W f(t,\xi) = \frac{\left|Wf(t,m)\right|^2}{m} \tag{9.8}$$

for $\xi = \eta/m$. It can be shown that the scalogram is utmost at [68]

$$\frac{\eta}{m(t)} = \xi(t) = \varphi'(t), \tag{9.9}$$

The corresponding points, $(t,\xi(t))$, are called wavelet ridges. Thus, the ridges are the local maxima of the scalogram. In multi-component signals that have more than one frequency, the instantaneous frequencies can be discriminated as long as the bandwidth relations (9.10) and (9.11) are satisfied [68].

$$\frac{\left|\varphi_i'(t) - \varphi_j'(t)\right|}{\varphi_i'(t)} \geq \frac{\Delta\omega}{\eta}. \tag{9.10}$$

$$\frac{\left|\varphi_i'(t) - \varphi_j'(t)\right|}{\varphi_j'(t)} \geq \frac{\Delta\omega}{\eta}. \tag{9.11}$$

In (9.10) and (9.11), $\Delta\omega$ is the bandwidth of $\hat{g}(\omega)$, φ_i and φ_j are the phases of any two frequency components in the given signal. Equations (9.10) and (9.11) are used to select the bandwidth and the number of scales for the wavelet. The AWT can be practically implemented in real-time, and integrated into a motor drive system using a simple and fast method based on the well known Fast Fourier Transformation (FFT) [69].

9.4 Analytic Wavelet Ridges Based Fault-Detection Algorithm

The AWT ridge based BLDC fault-detection strategy for detecting dynamic eccentricities in a BLDC motor is shown in Figure 9.1. The sampled stator current is adaptively filtered to remove the fundamental and all harmonics above two, exactly as in the previous two chapters, leaving behind only the fault frequency components in the BLDC motor current signal.

The AWT ridge extraction is shown in more detail in Figure 9.2. The AWT $Wf(t,m)$ with Gabor wavelet is then used to compute the scalogram of the current signal using (9.3). The scalogram, which is similar to the spectrogram of the WFT, is then calculated from the $Wf(t,m)$ using (9.4) as shown in Figure 9.2. A discrete version of the AWT is used as it is difficult to calculate the continuous AWT of (9.3). The computation of the continuous AWT in (9.3) assumes that the AWT is calculated for all values of the scale m from zero to infinity. However, this is not possible practically. In practice, the AWT is calculated for a range of predetermined scales, m. For example, the discrete wavelet transform (AWT computed at discrete scale intervals of m) is usually computed at scales $m = a^k$, with $a=2^{1/v}$, which provides v intermediate scales in each octave [2^k, 2^{k+1}) [68]. The instantaneous fault frequencies are then extracted from the scalogram by using the wavelet ridge algorithm. To achieve this, all the local maxima of the scalogram

are obtained by detecting the peaks of the scalogram. These local maxima are the ridges of the AWT. The amplitudes of the extracted ridges can be monitored to estimate the health of the BLDC motor.

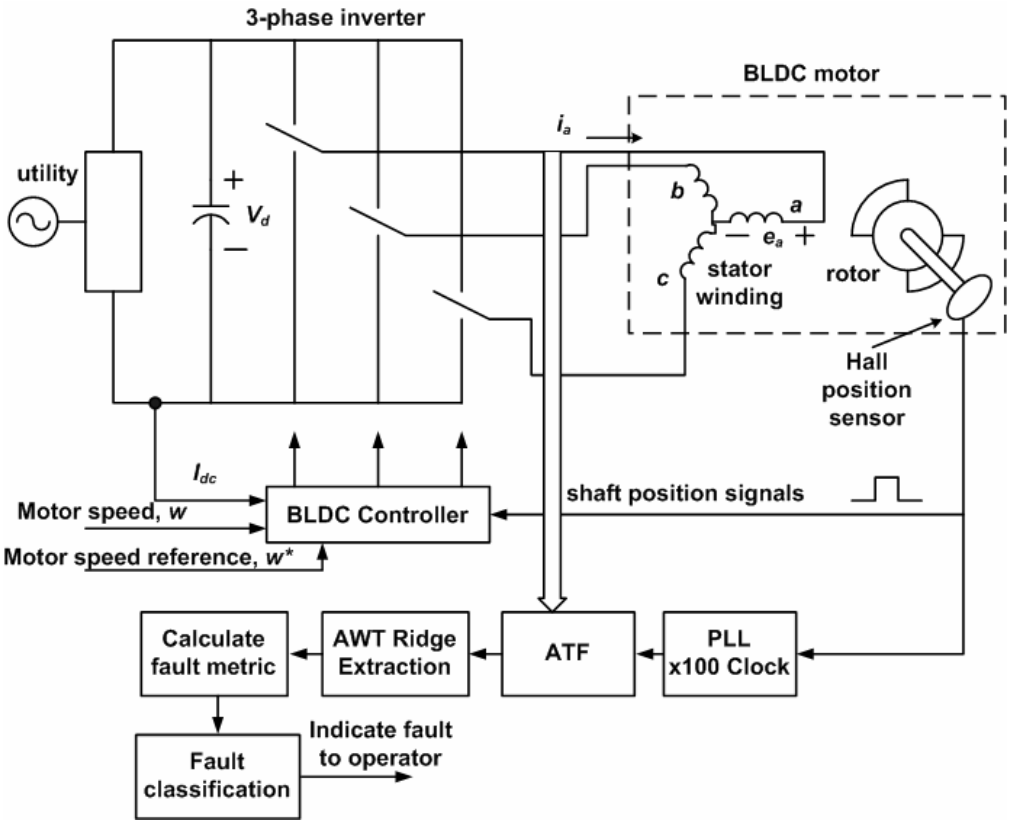

Figure 9.1: AWT ridge based BLDC rotor fault detector.

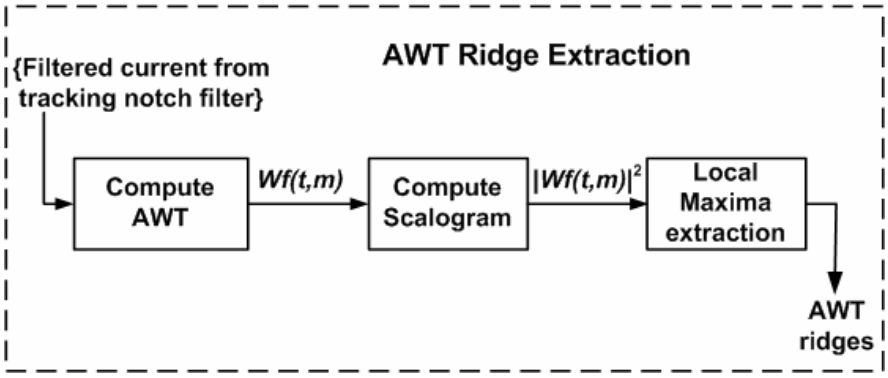

Figure 9.2: AWT ridge detection algorithm.

9.5 Experimental Results

The same experimental arrangement explained in Chapter 7 is used here. A six-pole, 12 V, 1 kW BLDC motor is used to implement dynamic eccentricity. Rapid time-varying motor operation is obtained by varying the speed reference. Experiments are conducted with sinusoidal, triangular, and randomly changing speed references. The sinusoidal and triangular references vary over a range of 0 to 10 Hz, representing most practically occurring applications. For a six-pole BLDC motor, the rotor fault frequencies occur at $1/3^{rd}$, $2/3^{rd}$, $4/3^{rd}$, and $5/3^{rd}$ times the fundamental frequency (3.10). The load conditions are again exactly the same as in the previous experiments and the stator current is sampled at 2 kHz.

The AWT ridge algorithm is implemented in MATLAB using the Wavelab802 toolbox from Stanford University [83]. The discrete wavelet version of the AWT is computed at eight scales selected as powers of two, $m^{-1} = \{2,4,8,16,32,64,128,256\}$. Twelve intermediate scales are also computed in between each scale.

Two important parameters of the Gabor wavelet play an important role in determining the quality of the method's time and frequency resolutions, namely, the variance, σ^2, and the wavelet center frequency parameter, η. Both these parameters need to be tuned to obtain the best performance. However, for the purpose of demonstrating the proposed AWT based fault-detection algorithm, the variance, σ^2, of the analytic Gabor wavelet is initially chosen as one. The frequency parameter, η, is then varied arbitrarily to obtain a good frequency resolution with as little interference terms as possible. A η of 14 is found to offer a good frequency resolution while also maintaining

good time resolution. The effect of both the variance and the center frequency will be further illustrated in section 9.6.b.

9.5.1 Dynamic Eccentricity – 5 Hz And 8 Hz Triangular Speed Reference

The stator current of the dynamically eccentric BLDC motor operating at a 5 Hz triangular speed reference and the scalogram ($|Wf(t,m)|^2$ in Figure 9.2) of the filtered stator current are shown in Figure 9.3. Darker zones in the scalogram represent higher amplitudes. The local maximas (also called as the AWT ridges) are computed from the scalogram as previously explained in Figure 9.2. These AWT ridges are the instantaneous frequencies of the signal. The instantaneous fault frequencies (AWT ridges) in the filtered stator current of Figure 9.3 are shown in Figure 9.4. The two dynamic eccentricity frequencies at $2/3^{rd}$ and $4/3^{rd}$ times the fundamental frequencies are distinctly seen to vary over time. The ridge algorithm efficiently extracts only the fault frequencies, while suppressing noise and other artifacts. The amplitude of these AWT ridges can be used to measure the health of the motor. The AWT ridges of the filtered stator current of a dynamically eccentric BLDC motor, now operating with an 8 Hz triangular speed, reference are shown in Figure 9.5. Again the AWT ridges are extracted from the scalogram (not shown here for this case) of the filtered stator current as explained in Figure 9.2.

9.5.2 Dynamic Eccentricity – Random Speed Reference

Similarly, the AWT fault ridges of the filtered stator current of a dynamically eccentric BLDC motor operating with a random speed reference are shown in Figure 9.6. Some interference terms are seen to be present in Figure 9.6. These interference terms arise as the frequency resolution conditions (9.10) and (9.11) are not satisfied for the

value of η, chosen here to be 14. However, these components are small and do not affect the rotor fault classification. The interference terms can be removed by carefully fine tuning the value of η. The fault ridges are tracked distinctly over time, thus confirming that AWT is a suitable tool for detecting faults in motors operating under rapidly varying speed conditions.

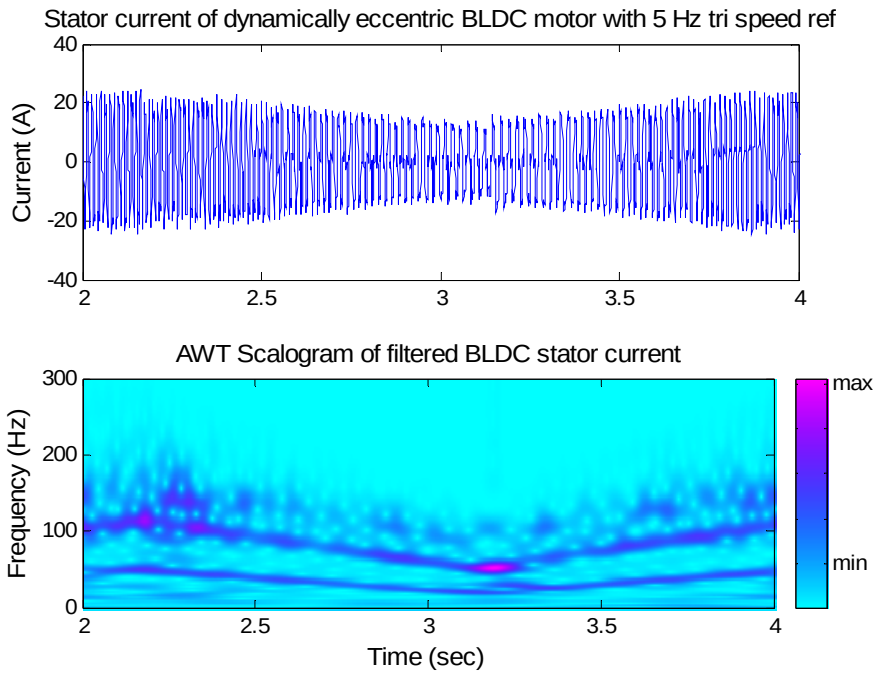

Figure 9.3: AWT scalogram of filtered BLDC motor (with dynamic eccentricity) stator current with 5 Hz triangular speed reference.

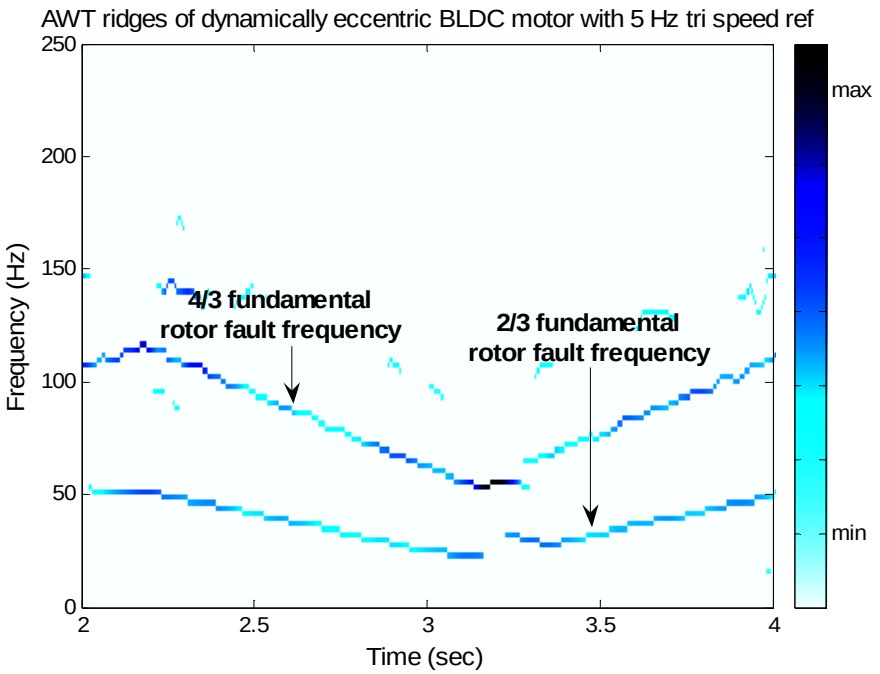

Figure 9.4: AWT ridge extraction from filtered stator current scalogram in BLDC motor operating with 5 Hz triangular speed reference.

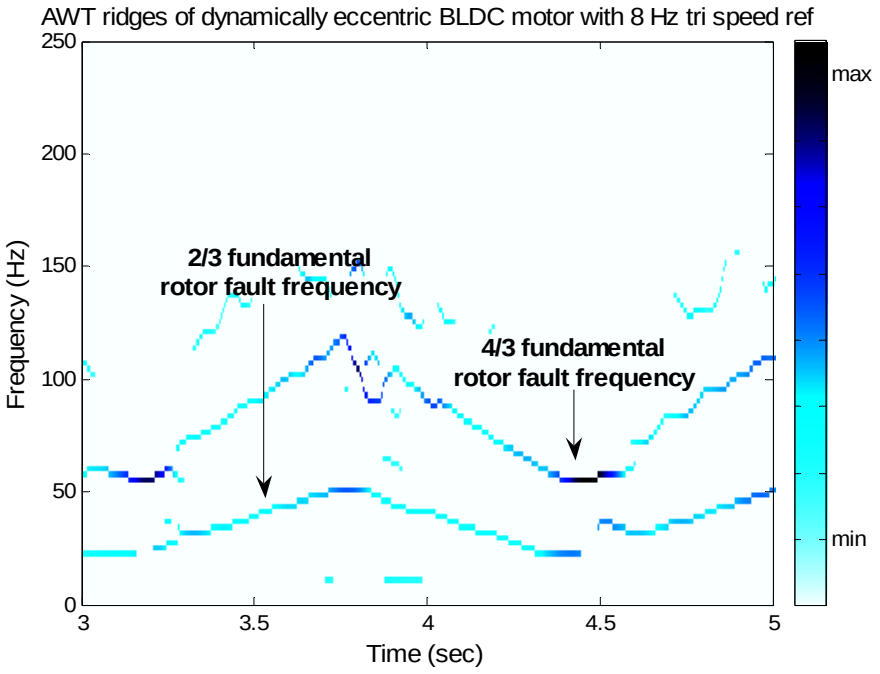

Figure 9.5: AWT ridges of filtered stator current in BLDC motor operating with 8 Hz triangular speed reference.

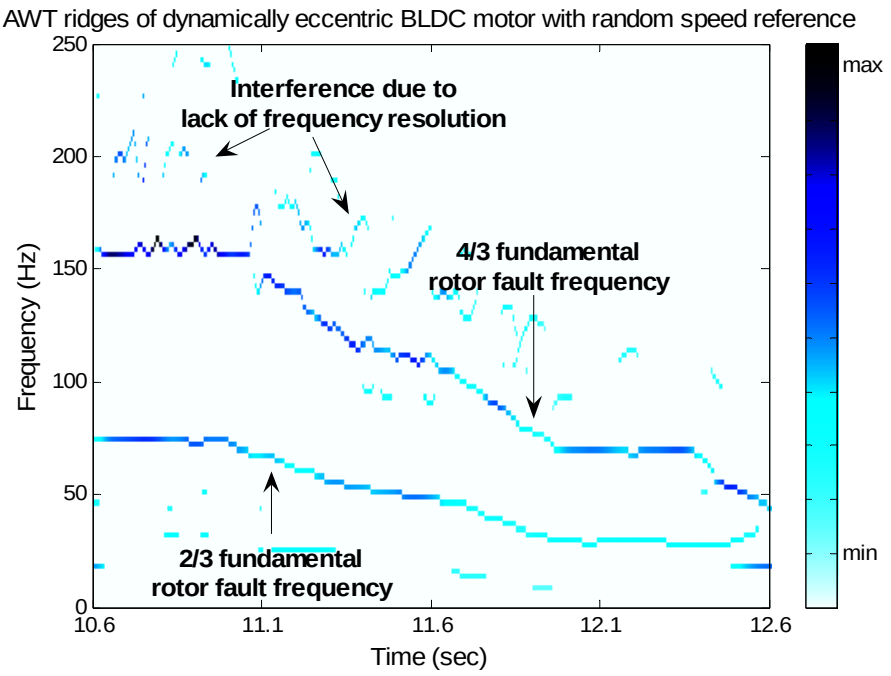

Figure 9.6: AWT scalogram of filtered BLDC motor (with dynamic eccentricity) stator current with random speed reference.

9.6 Limitations on Using Wavelets for Motor Fault Detection

9.6.1 Choice of Wavelets

The choice of the wavelet affects the fault detection process significantly. As the rotor faults are low-frequency sinusoidal quantities, smooth wavelets are needed to approximate these components. As a result, sharp discrete wavelets such as the Daubechies cannot be used for good accuracy. Smooth continuous wavelets are needed, but these wavelets cannot be easily implemented in practice as discrete versions for many of them are not available. The AWT offers a good compromise and is one of the few wavelets that can be used for motor fault detection. The small choice of suitable wavelets restricts their widespread use in motor fault diagnostics.

9.6.2 Frequency Discrimination

The wavelet ridge algorithm is subject to frequency resolution as is the WFT explained in Chapter 7. The frequency resolution of the Gabor analytic wavelet ridge algorithm is dependent on the parameters of the wavelet function, namely, the variance, σ^2, and the wavelet center frequency, η. The influence of the wavelet center frequency, η, is first investigated. The bandwidth conditions (9.10) and (9.11) have to be satisfied for good frequency resolution. This means that the AWT ridge method strongly depends on the parameter, η, which is the center frequency of the mother wavelet. This parameter must be carefully chosen and is usually selected through trial and error. In the experimental results of the previous section, η was carefully tuned to 14 to obtain a good performance (the value of σ^2 is still assumed as 1). Figure 9.7 shows the AWT for the same experimental result of Figure 9.4, but now for a η of value 6 ($\sigma^2 = 1$). The frequency discrimination in Figure 9.7 is poor and there are many interference terms. This illustrates the importance of carefully selecting η.

The Gaussian parameter, σ, is the standard deviation or the width of the Gaussian. Hence, this parameter directly controls the shape of the wavelet, thereby directly affecting the wavelet transform's time and frequency resolution. For example, the previous case of the AWT with $\eta = 6$ is again considered for analysis. The standard deviation, σ, is now increased to 2 ($\sigma^2 = 4$). Figure 9.8 now shows the AWT for the same experimental result of Figure 9.7, but with the new parameters. The interference terms are almost absent, and the resolution in both the time and frequency is much better. This demonstrates the importance of carefully selecting the standard deviation (or variance) in a Gaussian (Gabor) analytic wavelet.

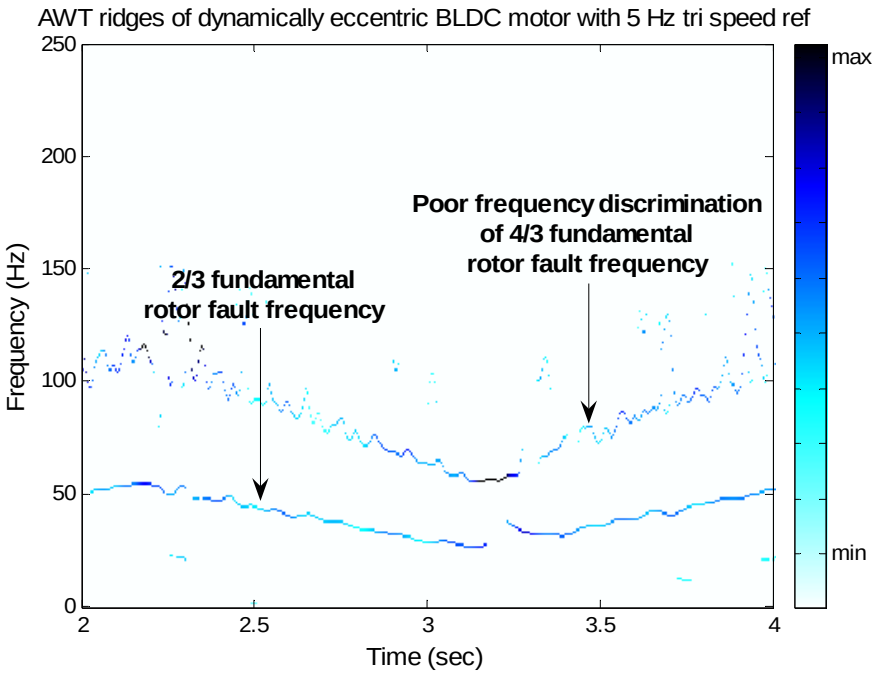

Figure 9.7: AWT scalogram of filtered BLDC motor (with dynamic eccentricity) stator current with 5 Hz triangular speed reference ($\eta = 6$, $\sigma = 1$) depicting poor frequency discrimination.

9.7 Conclusions

Assuming that BLDC rotor faults could be detected from the motor's stator current, a novel analytic wavelet transform based detector has been proposed for detection of dynamic eccentricity in BLDC motors operating under never steady-state conditions. The method does not need assumptions of local stationarity in the signal, as wavelets are multi-resolution tools developed for the analysis of non-stationary signals. Experimental results have shown that the AWT ridge method can track dynamic eccentricity frequencies under various types of non-stationary motor operation. The proposed method may also be used for the detection of other faults such as bearing faults. The method can also be used for rotor fault detection in other types of motors such as induction motors besides BLDC motors.

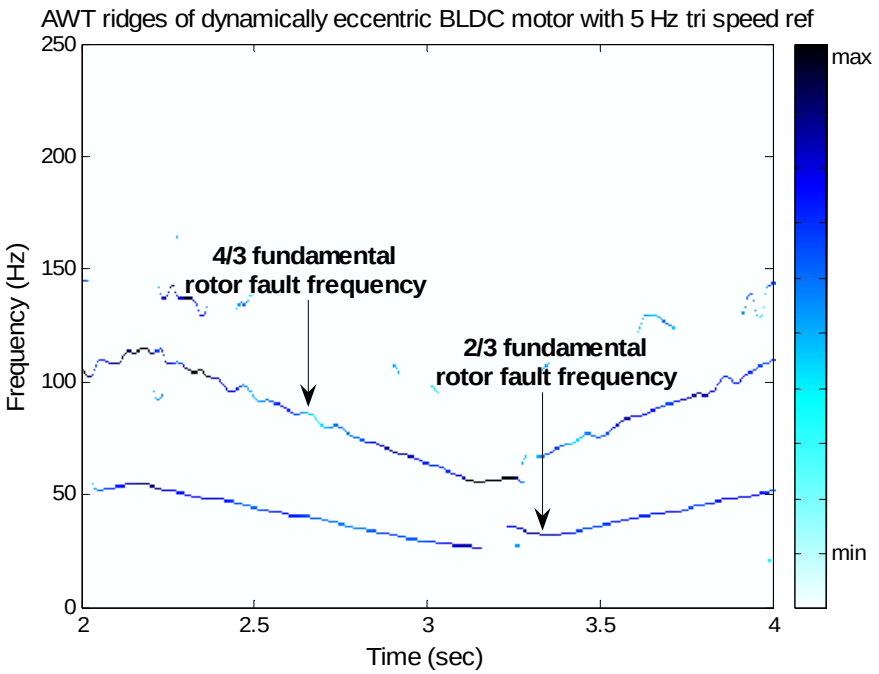

Figure 9.8: AWT scalogram of filtered BLDC motor (with dynamic eccentricity) stator current with 5 Hz triangular speed reference ($\eta = 6$, $\sigma = 2$) depicting good frequency discrimination.

However, the AWT has a strong dependence on the choice and center frequency of the mother wavelet. A careful selection of the wavelet and its frequency is essential for a good performance from this algorithm. If the chosen wavelet is Gaussian, the performance of the AWT also depends on the variance of the Gaussian function. These limitations, along with the increased computational complexity needed to implement the wavelets in real-time, greatly limits their use in online motor fault diagnostics.

A performance comparison of all the three methods proposed in Chapters 7 – 9 is presented in the next chapter, Chapter 10. The commercial implementation of these algorithms, and a comprehensive rotor condition monitoring method, will also be investigated.

CHAPTER 10

COMPREHENSIVE CONDITION MONITORING SCHEME

Chapters 7 - 9 investigated the use of time-frequency distributions and wavelets to detect rotor faults in motors operating under non-stationary conditions. This chapter compares the advantages and the disadvantages of the proposed methods. Selected time-frequency representations (TFRs) are implemented on a digital signal processor (DSP), and their computational time are compared in order to determine their suitability for implementation in a real system. An important aspect of any condition monitoring scheme is the fault classifier that eventually discriminates between a good motor and a faulty motor. This chapter presents a simple fault classifier that is developed for detecting rotor faults in BLDC motors. Finally, a comprehensive condition monitoring scheme is suggested, which not only diagnoses the health of the motor but also identifies the origin of the fault.

10.1 Real-Time Implementation and Computational Load

The most important factor in designing any real-time condition monitoring scheme is the computational load. The WFT, PWVD, and the CWD are compared for their suitability for implementation in a commercial system. To this effect, the three algorithms are implemented on an ADSP-21061-SHARC DSP operating with a 50 MHz clock and capable of 150 MFLOPS [95]. The ADSP-21061 is a 32-bit floating point processor optimized for high performance DSP applications. The algorithms are first written in C language using the Analog Devices Visual Studio environment [96].

A flag is inserted in the C code that provides an output pulse at one of the ADSP-210161's data ports, every time a time slice of data is processed. This pulse is observed on an oscilloscope and the time between two pulses is measured. This time is the time taken by the ADSP-21061 processor to compute one time-slice of data. The discrete implementation of the three selected signal processing techniques is explained in this section.

10.1.1 Discrete Implementation of the WFT

The WFT is implemented using a simple FFT. A pre-built FFT function in the ADSP-21061 software library is used to calculate the WFT. The FFT is a fast algorithm to solve the discrete Fourier transform (DFT), which is the discrete version of the WFT. The DFT of Q samples of a signal s ($s_0, \ldots s_{Q-1}$)is given as

$$S_k = \sum_{n=0}^{Q-1} s_n e^{-\frac{2\pi i}{Q} kn}, \quad k = 0, \ldots, Q-1 \tag{10.1}$$

where S_k is the k^{th} frequency component of the signal, s.

10.1.2 Discrete Implementation of the PWVD

For practical implementation of distributions of the Cohen's class described in Chapter 8, the generalized discrete-time discrete-frequency distribution (GDTDFD) is defined as [97, 98]

$$\hat{\mathrm{P}}\left(l, \theta; \hat{\Phi}\right) = \sum_{n=-\infty}^{+\infty} R_l\left(n\right) e^{-j2n\theta}, \tag{10.2}$$

where l is the instantaneous time (position), θ is the instantaneous frequency and is $\hat{\Phi}$ the discrete kernel of a quadratic TFR. The auto-correlation sequence R_l is

$$R_l(n) = \sum_{m=-\infty}^{+\infty} s(l+m+n)\, s^*(l+m-n)\, \hat{\Phi}(m, 2n). \tag{10.3}$$

$\hat{\Phi}(m, 2n)$ is the discrete-domain kernel that defines the time-frequency representation [99]. In practice, only a finite span in time of the signal is available. This can be represented by applying a sliding window of length 2N+1 over the signal under analysis, so that equations (10.2) and (10.3) can be rewritten as

$$\hat{\mathrm{P}}(l, \theta; \hat{\Phi}) = \sum_{n=-N}^{+N} R_l(n)\, e^{-j2n\theta} \tag{10.4}$$

and

$$R_l(n) = \sum_{m=-N}^{+N} s(l+m+n)\, s^*(l+m-n)\, \hat{\Phi}(m, 2n). \tag{10.5}$$

For the Wigner distribution, the discrete-domain kernel is given by

$$\hat{\Phi}(m, 2n) = \delta(m). \tag{10.6}$$

Substituting (10.5) in (10.6) yields the auto-correlation sequence,

$$R_l^{WD} = s(l+n)\, s^*(l-n). \tag{10.7}$$

The auto-correlation sequence is first computed. The discrete Fourier transform (DFT) of the auto-correlation sequence is then computed to obtain the DWVD of the sequence. The DWVD can be efficiently computed using standard Fast Fourier

transform (FFT) algorithms. The computation is further optimized by evaluating two successive R_l sequences together [99]

$$R_{comb}^{WD} = R_{l1}(n) + j\, R_{l2}(n). \tag{10.8}$$

Thus, the discrete Fourier transform (DFT) of the individual sequences can be evaluated using a single DFT for the combined kernel, thereby halving the number of final FFTs used. The Hilbert transform is implemented as a 79-tap finite impulse response (FIR) filter [99].

10.1.3 Discrete Implementation of the CWD

Here, the exponential CWD kernel (Table 10) is selected in the original domain, and then a Fourier transform is performed along one of its axes to get the kernel in the ambiguity domain. Thus a new correlation vector is constructed, and from there the same algorithm used previously in the WVD, is applied.

10.1.4 Comparing Load Computations

A signal sample comprising of two fault frequencies and length 1024 samples is used to evaluate the load computations. The TFRs are calculated using a 512-point FFT. The load computations for one time slice of data processed is measured on an oscilloscope and is compared in Table 10.1, which shows that the load computations increase as more complex kernels such as the CWD are used. The WFT is implemented using a Gaussian window of length of 0.0625 seconds. The length of the window is chosen heuristically to best fit this application. While the WVD takes almost 4 times the computation time of the spectrogram, more sophisticated distributions like the CWD take about 50 times the computational time of the spectrogram. However, the WVD and

CWD yield better frequency resolution and localization and do not suffer from the problems related to the type and size of the window as in the WFT.

Table 10.1: Computational time for selected TFR kernels

TFR	Computation time per time slice (μ-sec)
WFT	0.46
WVD	2.02
CWD	27.93

10.2 Comparison of Non-Stationary Motor Fault-Detection Algorithms

Chapters 7 – 9 investigated three signal processing techniques that could be used for fault detection in motors operating under non-stationary conditions. The advantages and disadvantages of all the proposed methods are summarized in Table 10.2.

Among the three methods, the WFR is the simplest to implement and is widely used. Hence, it is recommended as the first choice in non-stationary motor fault diagnostics. This technique can be used for most of the non-stationary operation cases where high frequency resolution is not needed over a wide speed range. As the WFR uses a window of fixed length to look closely for non-stationarity in the signal, the frequency resolution is fixed. Hence this frequency resolution may be optimum only over a small range of motor speeds and may not be suitable at other ranges (usually at low frequency). The size of the window has to be optimized for every application. The

performance of the WFR also depends on the type of window. The choice of window can affect the amplitude of the extracted fault frequencies because of the Gibb's phenomenon as explained in Chapter 7. The dependence of the WFR on the choice and length of the window is its greatest disadvantage, but the method can be implemented quickly and has a low computational time.

In cases where more computational power is available, the quadratic TFRs could be used to obtain better performance. The non-dependence of the quadratic TFRs on any window, and their inherent suitability to non-stationary signal analysis, make them an attractive choice for non-stationary motor fault diagnostics. The increased computational load is the price paid if a better frequency resolution and good localization of energy is needed. In spite of the increased complexity involved, the computation time of a CWD is still in the order of a few tens of micro-seconds, and hence is amenable to implementation in real-time. This computational time can be further decreased by paralleling several micro-programmed systems, and using more optimized software routines. Newer processors run at much higher speeds and can decrease the computation time by as much as ten times. Moreover, as motor diagnostics is performed over relatively long intervals of time, the computation time may not be critical, and hence most of the quadratic TFRs can be effectively used.

While the analytic wavelets have been demonstrated to be effective in tracking the fault frequency components, the dependence of the method on the type and the centre frequency of the wavelet is a major limitation, especially considering the fact that these methods are complex to implement in practice. Even though this method is promising, the wavelets take the last priority among all the evaluated signal processing conditions.

More work is eventually needed to develop a wavelet that is uniquely suitable for motor fault diagnostics. Methods to simplify its practical implementation have to be explored further before the wavelets could be considered as a practically suitable condition monitoring scheme.

Table 10.2: Comparison of non-stationary fault-detection algorithms

	WFR	**Quadratic TFR**	**AWT**
Frequency Resolution	Good	Excellent	Good
Dependence	Window type/length	None	Wavelet type/center frequency
Computational Complexity	Low	High	High
Suitability to non-stationary signal analysis	Good	Excellent	Excellent
Artifact creation	Low	Medium	Medium

10.3 Fault Classification - Root Mean Square (RMS) Fault Metric Based Threshold Classifier

Chapters 7 – 9 explain the process of fault feature extraction. Once the fault frequencies are computed, the next step is to use the extracted frequency information to monitor the health of the motor. This can be done by either using a simple RMS fault metric that monitors the magnitude of the fault frequencies over time, or by using more sophisticated fault classifiers such as artificial neural networks (ANN). A simple RMS-based fault classifiers is explained in more detail in this section.

Every motor has some small abnormality from the time of manufacture. For example, typical eccentricity tolerances during manufacture are indicated by total indicative roundness (TIR) by motor manufacturers and are usually in the range from 5% to 20% [100]. The purpose of a fault classifier is to learn the behavior of a good motor and observe / track the deviation in the fault frequency components over time. This learning process cannot be generalized for families of electric motors and must be performed for every individual motor whose health is to be diagnosed. A large deviation in the magnitude of these fault frequencies, from what should have been the normal amplitudes for a good motor, is indicative of a progressing fault.

A simple RMS fault metric that could be used to monitor the health of the motor is calculated from the RMS of the instantaneous amplitudes of the extracted fault frequencies and is given by

$$RMS\ Fault\ Metric = \sqrt{\frac{1}{N_r}\sum_{i=1}^{i=N_r} f_i^2(t)}, \tag{10.9}$$

where $f_i(t)$ is the amplitude of the instantaneous rotor fault frequencies extracted from the spectrogram of the filtered current using the ridge algorithm. The N_r in (10.9) corresponds to the number of Fourier ridge frequencies extracted at any given time. This metric is used to indicate a developing rotor fault and the proposed scheme is shown in Figure 10.1.

As the motor's operating condition, namely the speed and the load, vary continuously over time, the amplitudes of the fault frequency components vary too. For this reason, a threshold that can adapt to instantaneous operating conditions is needed for fault discrimination in motors operating under non-stationary conditions.

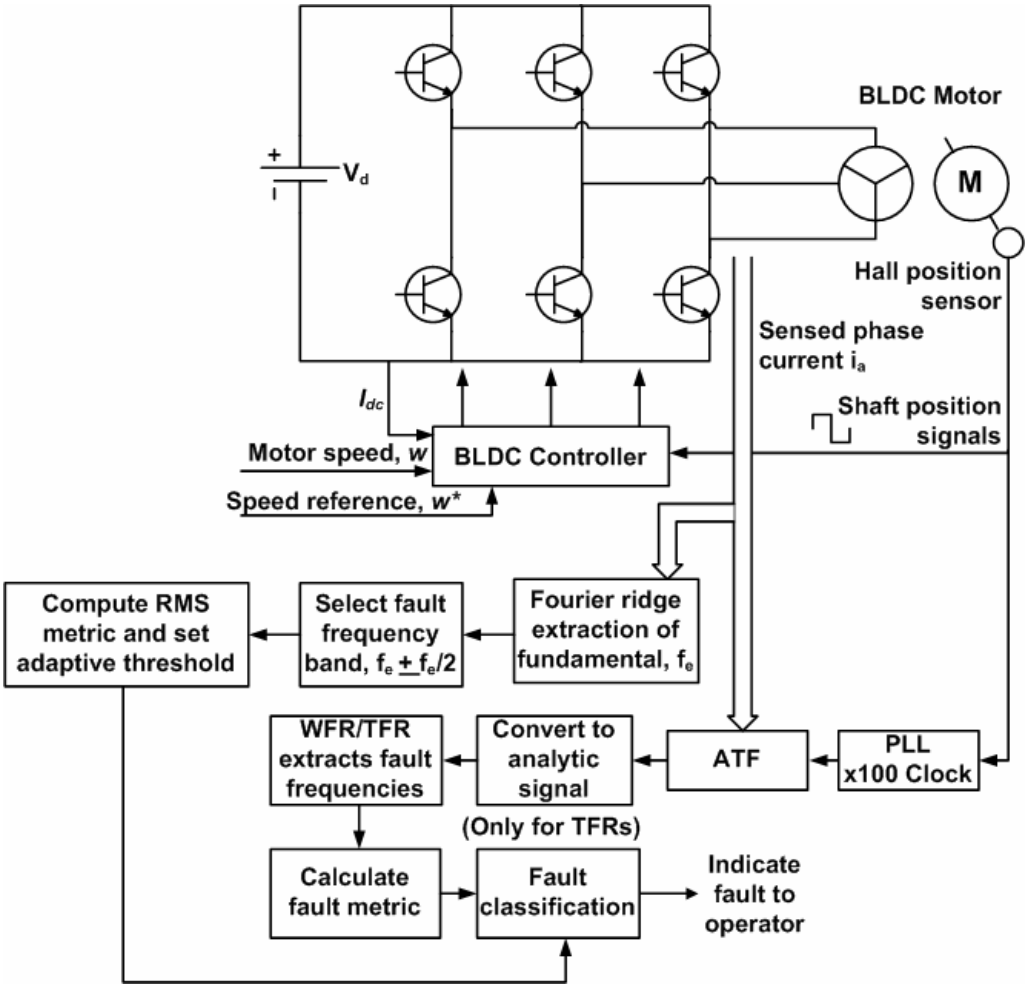

Figure 10.1: RMS fault classifier for BLDC motor fault detection.

Figure 10.2 demonstrates the fault metrics calculated using (10.9) for a mechanically balanced and an unbalanced motor, using the instantaneous RMS of the WFR fault ridge amplitudes extracted from the spectrogram of the filtered stator current. The BLDC motor in this case is operating in a transient state, with a speed reference that is changing sinusoidally at a rate of 3 Hz. A clear change can be seen in the fault metric of the mechanically unbalanced motor indicating a fault condition. This fault metric can be used along with a predetermined threshold as an indicator for automatic detection of rotor faults in BLDC motors.

Similarly, Figure 10.3 shows the RMS fault metric computed using (10.9) for fault frequencies extracted from the stator current of a dynamically eccentric BLDC motor operating with a 5 Hz triangular speed reference. The RMS fault metric of the defective BLDC motor can be seen to be much higher than the RMS fault metric of a good motor.

The fault metric computed for a motor with dynamic eccentricity and a good motor are shown for two different time segments in Figures 10.4 and 10.5. The time scales have been normalized to obtain a common base for comparison, and hence represent a time from 0 to 2 seconds. The dynamically eccentric motor in this case is again operating with a sinusoidal speed reference of 3 Hz and the fault frequencies are extracted using the WFR algorithm. A significant difference in the fault metrics of the good and the faulty motor cases can be seen. The fault can be automatically detected by setting a threshold. An adaptive heuristic threshold that varies as 2% of the amplitude of the fundamental frequency component (Figures 10.4 and 10.5) is used to discriminate between the good and the bad motor.

The amplitude of the fundamental frequency is obtained from the TFR/analytic wavelet computed on the unfiltered BLDC motor current signal. This is done by computing the RMS metric of (10.9) for a small present band of frequencies around the fundamental (Figure 10.1). Several individual bands with their respective RMS metrics can be computed to separate multiple fault frequencies. This would help classify the actual defect in the BLDC-load system.

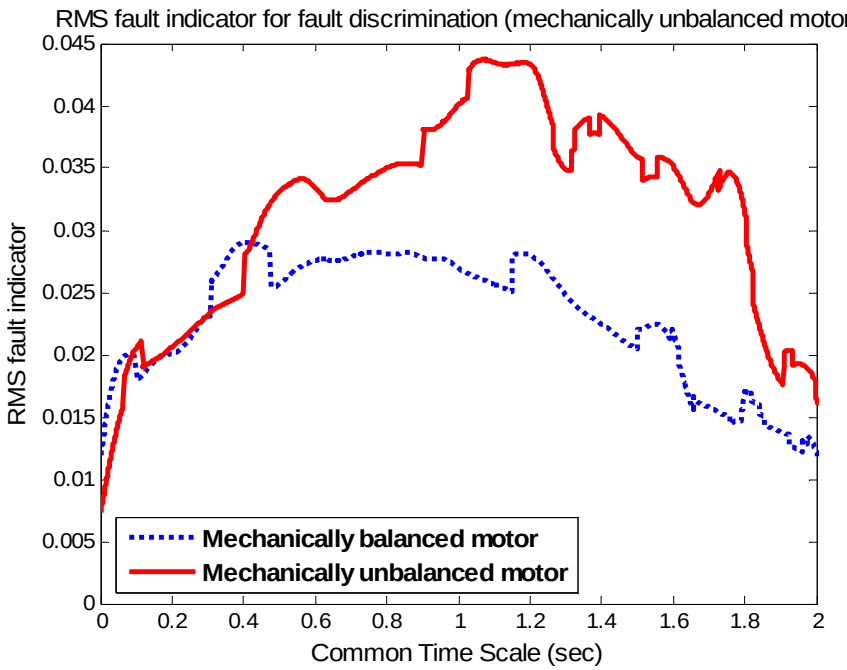

Figure 10.2: RMS fault indicator computed from WFR discriminates BLDC rotor unbalance (3 Hz sine speed ref); Measurement Error = $\pm$ 10%.

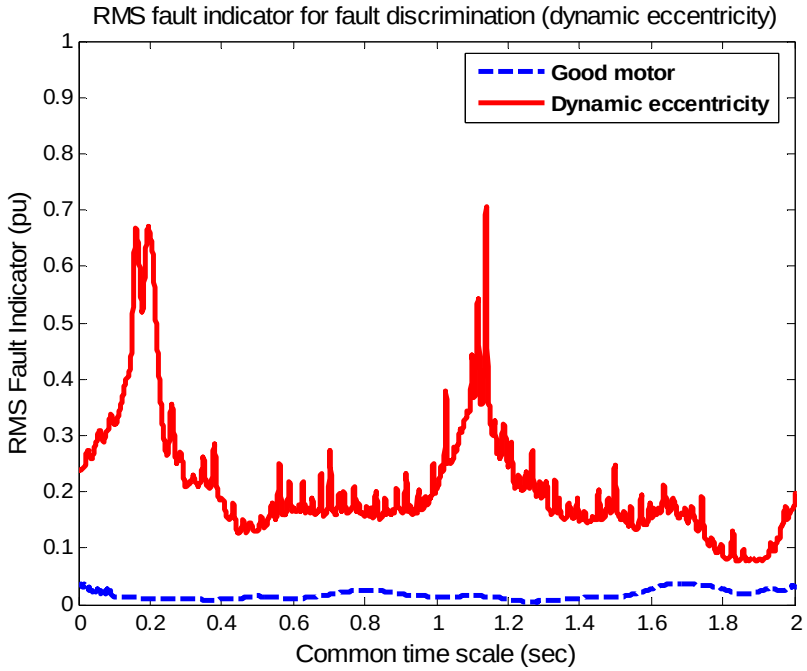

Figure 10.3: RMS fault indicator computed from the CWD discriminates BLDC dynamic eccentricity (5 Hz triangular speed ref); Measurement Error = $\pm$ 10%.

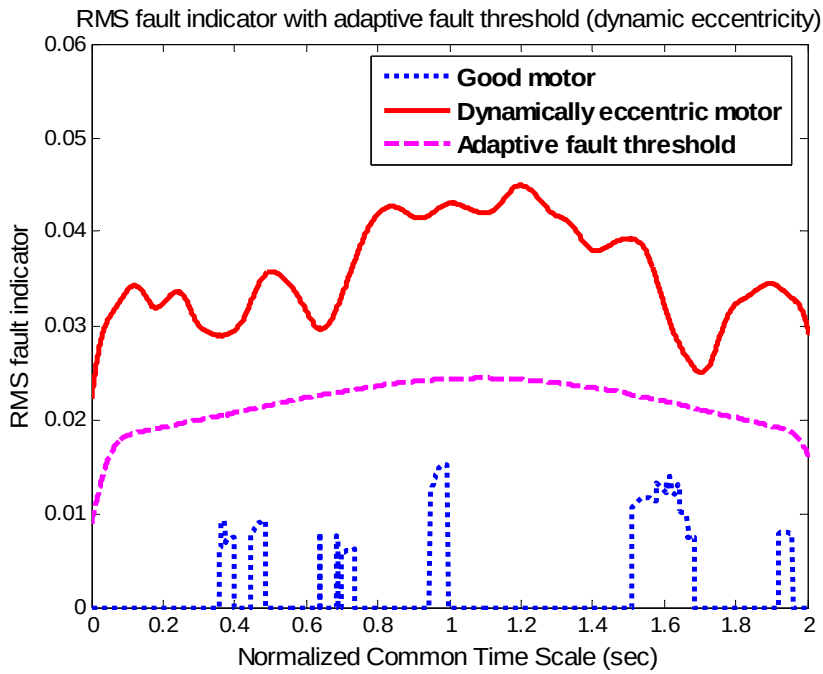

Figure 10.4: Discriminating dynamic eccentricity with adaptive threshold set at 2% of fundamental amplitude (3 Hz sine speed reference); Measurement Error = $\pm$ 10%.

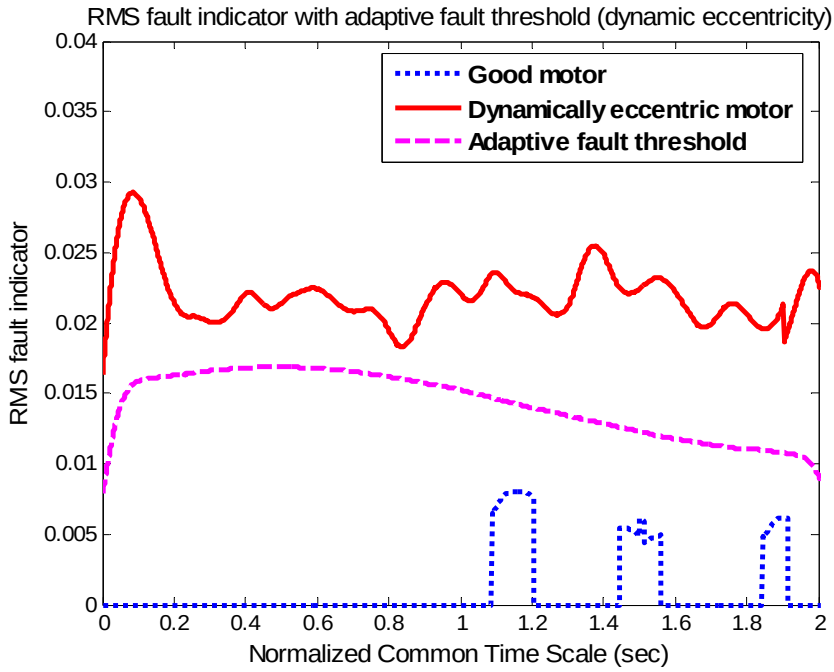

Figure 10.5: Discriminating dynamic eccentricity with adaptive threshold set at 2% of fundamental (3 Hz sine speed reference) for time segment different from Figure 10.4.

10.4 Comprehensive Rotor/Load Condition Monitoring Scheme

Based on the information generated in this research, a comprehensive rotor/load condition monitoring scheme for BLDC motors is suggested. A flow chart of this proposed scheme for a six-pole BLDC motor is shown in Figure 10.6. The suggested scheme monitors the magnitude of several fault frequencies (3.10) in the instantaneous spectra of the filtered BLDC motor current. Additionally, the BLDC torque constant, Kt, can also be monitored simultaneously. A significant change in the torque constant usually indicates a damaged rotor magnet fault [36]. The presented algorithm is intended to not only track and determine a BLDC motor fault, but also accurately indicate the origin of the detected fault.

The good motor is first operated under a variety of operating conditions prior to commissioning, in order to create a data base of fault frequency amplitudes as a function of motor speed and load. This data base can be updated using intelligent fault classifiers like ANNs if needed.

The condition monitoring scheme starts monitoring the BLDC motor health as soon as the motor is commissioned. A significant change in both the stator current fault frequency magnitudes and the motor torque constant may indicate trouble in the BLDC motor magnets (possible demagnetization or cracks). A change in only the stator current fault frequencies may indicate an eccentricity fault or misaligned couplings. Similarly a change in gear fault frequencies may indicate trouble in the gear arrangement.

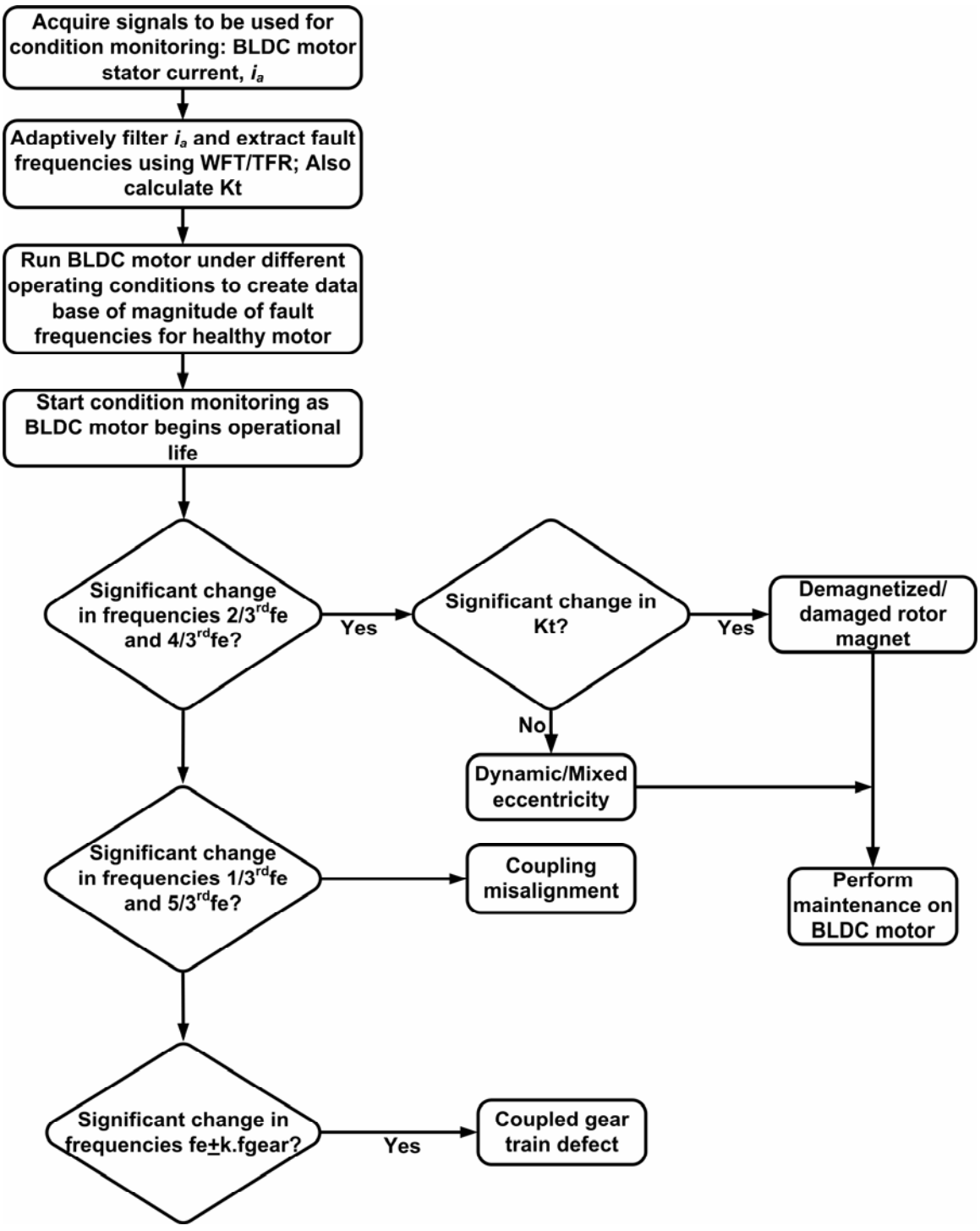

Figure 10.6: Comprehensive BLDC motor rotor/load fault condition monitoring scheme.

Static eccentricity is not included, as it is difficult to detect especially in surface mount magnet BLDC motors. This is because static eccentricity is typically detected using the magnitude of the principle slot harmonics which are absent in the smooth rotors of PM machines. Detection of static eccentricity through negative sequence components is also difficult, as static eccentricity induced unbalance is miniscule because of the large air-gap and the magnet which almost behaves like air ($\mu_r = 1.09$).

10.5 Conclusions

This chapter has compared the performance of all the condition monitoring algorithms developed for non-stationary motor fault diagnostics. Some of the important TFRs have been implemented on a DSP platform. and their suitability for commercial implementation has been demonstrated. A simple RMS based fault classifier with an adaptive fault thresholding scheme has been presented that can discriminate faults in non-stationary motor operating conditions. Finally, a comprehensive rotor/load fault monitoring scheme has been suggested that may not only detect developing motor faults, but can also accurately point to the origin of the fault.

The conclusions and contributions of this research, and the recommendations for future research, are presented in the next chapter, Chapter 11.

CHAPTER 11

CONCLUSIONS, CONTRIBUTIONS, AND RECOMMENDATIONS

11.1 Summary and Conclusions

The purpose of this research is to advance the field of rotor and load fault diagnosis in BLDC machines operating in a variety of operating conditions ranging from constant speed to continuous transient operation. The fast growth in applications of the BLDC motor in sensitive applications has increased the need for continuous condition monitoring of their health. Diagnostics of rotor and load faults related to the BLDC motor are the focus of this research.

11.1.1 Conclusions of Research Phase 1: Experimental Study of BLDC Faults Under Constant Speed Operation

The fundamentals of BLDC operation and the production of rotor faults are reviewed. A detailed literature survey is presented to summarize state of the art techniques that are pertinent to the methods proposed in this research. The present research is organized into three phases. The first phase of this research consists of experimental characterization of rotor faults in BLDC motors operating at constant speed. Rotor faults in BLDC motors operating at constant speed may be detected by monitoring certain characteristic fault frequencies in the motor current spectrum. Every motor has some small abnormality from the time of manufacture and it has some of the fault frequency components. Hence, in all the condition monitoring algorithms, base measurements are taken for a good motor at the time of commissioning. Once commissioned the fault algorithm monitors the amplitudes of the fault frequencies and

tracks changes in their amplitudes over time. A significant change in the amplitudes indicates a developing fault.

Three rotor faults (dynamic eccentricity, unbalanced rotors, and damaged rotor magnet) are practically implemented and their effects on the motor voltage and current are studied. As a six-pole BLDC motor is used, the significant fault harmonics of interest in the motor stator current occur at $2/3^{rd}$ and $4/3^{rd}$ times the fundamental frequency. In all the three rotor faults, these harmonics show a significant increase when faults are applied. The measurement accuracy in the experiments is about $\pm$ 10%. For example, in the case of a dynamically eccentricity BLDC motor operating at light load (30% full load) and with its rotor shifted by 33% of the air-gap length; the $2/3^{rd}$ fundamental frequency harmonic increases from 40 mA to 274 mA (good motor to bad motor) and the $4/3^{rd}$ fundamental frequency harmonic increases from 45 mA to 148 mA (good motor to bad motor). Under full load conditions, these harmonics are a bit more damped because of the coupling between the load and the motor stiffens; nevertheless a strongly measurable change is still noticeable. For example, under full load the $2/3^{rd}$ fundamental frequency harmonic increases from 86 mA to 332 mA (good motor to bad motor) and the $4/3^{rd}$ fundamental frequency harmonic increases from 58 mA to 76 mA (good motor to bad motor). A similar behavior is noticeable in the other two fault cases of unbalanced rotor and damaged rotor magnet fault. It has also been demonstrated through simulations that static eccentricity may be more challenging and difficult to detect. This is because, a smooth rotor motors lacks the principle slot harmonics that are usually used to detect the static eccentricity.

The role of pulsating loads (reciprocating compressors) in stator current based motor fault diagnostics is also investigated in this research. It is demonstrated that large pulsating loads produce harmonics that may mask rotor fault components in the current frequency spectrum. Therefore, the separation of pulsating load from a rotor fault is essential for reliable condition monitoring. For example, in the case of a pulsating load with an oscillating component that oscillates at the rotor speed, the $2/3^{rd}$ and the $4/3^{rd}$ times fundamental frequency fault harmonic in the motor stator current are measured to be 694 mA (30% full load) which is an order of magnitude higher than the BLDC motor with a dynamic eccentricity.

11.1.2 Conclusions of Research Phase 2: Detection of Load and Coupling Faults in BLDC Motors Under Constant Speed Operation

The second phase of this research proposes methods for detection of faults in loads, particularly gears coupled to BLDC motor using the stator current. This offers an inexpensive alternative when compared to vibration based monitoring that use expensive accelerometers to sense the machine vibrations. It is shown that various gear faults appear as different load perturbations to the electric motor and result in unique frequency patterns in the stator current spectrum. Such frequency patterns are produced by amplitude modulation in the stator current signal. Three gear defects are implemented in the laboratory: broken teeth defect, loss of lubrication, and debris in the gear. Depending on the fault, the stator current harmonics indicate different patterns of fault harmonics. By way of an example, a worm gear (66 teeth and gear ratio of 22:1) with two damaged teeth and operated by a BLDC motor with a torque control, generates a rich spectrum of harmonics in the stator current spectrum spaced 2.8 Hz apart on both sides of the

fundamental frequency (180 Hz). The 2.8 Hz (= 180/66) corresponds to the rotational frequency of the reduced speed gear. A loss of lubrication on the other hand produces just two sidebands at 170.9 Hz and 176.1 Hz, one on each side of the fundamental frequency (173.5 Hz). These harmonics are spaced at 2.6 Hz around the fundamental frequency and the 2.6 Hz happens to be the rotating frequency of the reduced speed worm gear. These frequency sidebands can be used to identify a gear defect, its type and its severity (based on the change in harmonic magnitude from a good gear to bad gear).

The gear fault frequencies noticed in the BLDC stator current are also noticeable in the line-to-line stator voltage and this can be used to improve fault detection in torque (current) controlled motors such as the one used in the experiments during this research. In theory, a current controlled motor should have no stator current harmonics as the motor current is controlled and corrected to follow the reference value. Hence the abnormality should completely appear in the stator voltage. However, in practice this is not completely true. If the load torque perturbation occurs at a low frequency especially a frequency that is smaller than the current controller bandwidth, then the perturbation goes through the controller, although attenuated to some extent (i.e. in this case the current controller is not able to completely filter off the perturbation). This results in the perturbation being transferred to the stator current, which results in the fault harmonics appearing in the motor stator current spectrum. As the current controller only partially attenuates or tries to correct the perturbation (abnormality) by varying the voltage, the same harmonics are also observable in the voltage. The magnitude of the harmonics in both the current and the voltage eventually depends on the current controller bandwidth.

However, the knowledge of fault harmonics in the motor stator voltage provides an additional tool for fault detection that can make the diagnostic scheme more reliable.

As a part of the second phase of this research, coupling defects have also been analyzed. Coupling misalignments develop fault frequencies in the motor stator current at $1/3^{rd}$ and $5/3^{rd}$ the fundamental frequency in six-pole motors. An angular coupling misalignment is recreated in the laboratory and this yielded a $1/3^{rd}$ fundamental frequency component change from 206 mA to 520 mA (good coupling to misaligned coupling) and a $5/3^{rd}$ fundamental frequency component change from 135 mA to 464 mA (good coupling to misaligned coupling), under 60% full load condition. This again demonstrates that coupling defects may be uniquely distinguished from other rotor and load defects.

11.1.3 Conclusions of Research Phase 3: Non-stationary BLDC Motor Fault Detection

The third and the most significant phase of this research is the diagnosis of rotor faults in BLDC motors operating in non-stationary conditions. Diagnostics of motor health in transient operating conditions is challenging because of the fact that the well known Fourier transformation no longer applies to non-stationary signals. This is particularly more challenging in a BLDC motor as the current is a square-wave that contains a large number of inverter harmonics besides the fundamental and rotor fault frequencies. Three methods are proposed in this research to track rotor faults in non-stationary motor operating:

1. Method 1: Windowed Fourier ridges based fault detection.
2. Method 2: Quadratic time-frequency distribution based fault detection.

3. Method 3: Analytic wavelet based fault detection.

11.1.3.1 Method 1: Windowed Fourier Ridges Based Fault Detection

Windowed Fourier ridges are local maximas computed from the spectrogram of a non-stationary signal. The Fourier ridges can be detected for maximas of comparable magnitude in multi-component signals. Experimental results have been conducted to reproduce several cases of non-stationarity. Rapid time-varying motor operation is obtained by varying the speed reference. Experiments are conducted with sinusoidal, triangular, and randomly changing speed references. The sinusoidal speed variation is the least severe of the three types of non-stationarity implemented, with the triangular speed variation as the next more severe, and the continuous random speed variation being the worst case scenario. The frequencies of these variations selected for these experiments are 3 Hz, 5 Hz, 8 Hz, 10 Hz, 12 Hz, and 15 Hz and they represent the range of most practically occurring scenarios. During the experiments it is noted that the ridge algorithm is able to extract frequencies from the motor stator current up to a sinusoidal speed reference of 15 Hz and a triangular speed reference of 10 Hz. Beyond these speed reference rates, the current is extremely non-stationary (especially with a triangular reference) and no longer possess any instantaneous frequency. However, such non-stationarity does not commonly occur in motor applications, and any non-stationary fault detection methods based on the windowed Fourier ridge algorithm should take into account the severity of the non-stationary behavior that may be encountered. Moreover, the frequency resolution of the windowed Fourier ridge algorithm depends on the size and type of the window which has to be chosen carefully to obtain the best performance. Another limitation is the fundamental frequency tracking range of the adaptive tracking

filter (ATF) which in this case is from 30 Hz to 200 Hz. The windowed Fourier ridge algorithm is not able to extract anything meaningful beyond these ranges as the performance of the filter deteriorates.

11.1.3.2 Method 2: Quadratic Time-Frequency Distribution Based Fault Detection

The second proposed method, method 2, involves the use of quadratic time-frequency distributions. Wigner-Ville distributions and its variants, namely the smoothed pseudo Wigner-Ville distributions are the basic examples of this kind of distribution. The feasibility of using more sophisticated time-frequency methods such as the Choi-Williams distribution or the Zhao-Atlas-Marks distribution has also been demonstrated. This method, method 2, has particular advantages in fault detection at lower operating frequencies because of its better frequency resolution; its most important advantage is its non-dependence on any window type or length. Experiments and simulations have again been used to demonstrate the validity of this method. The third method uses analytic wavelets to track and detect faults. The quadratic TFRs however provide much better frequency resolution and localization of energy with the ZAM distribution exhibiting the best performance. During the experiments, it is again noted that these algorithms are able to extract frequencies from the motor stator current up to a sinusoidal speed reference of about 15 Hz and a triangular speed reference of 10 Hz, beyond which the motor current no longer possesses any useful frequency information.

11.1.3.3 Method 3: Analytic Wavelet Based Fault Detection

Finally, the use of wavelets, method 3, in non-stationary motor fault diagnostics has also been explored. Wavelets, especially discrete wavelets, such as the Daubechies, are not suitable for motor fault diagnostics as these are sharp wavelets and cannot

approximate the smooth sinusoidal rotor fault frequency components. However, there is a special class of smooth wavelets called the Gaussian (Gabor) analytic wavelets that possess both frequency and magnitude information and could be potentially suitable for motor fault diagnostics. This has indeed been seen in this research when the wavelets were put to test on the same data used for the previous two methods resulting in good frequency extraction and tracking. However, these wavelets suffer from a frequency resolution problem that is similar to the windowed Fourier ridges. The performance of the analytic wavelet in discriminating the fault frequencies depends on the choice of the centre frequency of the mother wavelet. For example, in the present case of dynamic eccentricity, the analytic wavelet transform loses its frequency resolution as the centre frequency parameter, η,of the Gaussian function changes from 14 to 6. The latter case generates many interference terms that mask or diminish the actual rotor fault frequency components. In addition to the centre frequency, the frequency resolution of the analytic wavelet also depends on the value of the variance (σ^2), if the chosen wavelet is a Gaussian wavelet. By way of an example, a change of variance from 1 to 4 with a wavelet center frequency of 6 Hz, significantly improves the frequency resolution.

11.1.3.4 Commercial Implementation and Comparison of the Proposed Non-Stationary Fault-Detection Techniques

As a part of the third phase of this research, some of the signals processing schemes are implemented on a DSP. One common myth has been that the quadratic time-frequency distributions are not suitable for commercial implementation. This research has addresses this issue in detail. The computational loads of some of the quadratic time-frequency distributions are studied. For example, it is measured that a

PWVD takes about 2.02 μs to compute one slice of time information containing about 1024 samples sampled at 2 kHz. This computational load is much larger for more sophisticated kernels such as the CWD which took 27.93 μs to compute the same time slice but provides much sharper frequency resolution. It is thus demonstrated that the proposed signal processing methods can be used for real-time fault diagnostics since condition monitoring in electric motors n is performed only over long intervals of time, usually every 30 minutes or an hour.

A comparison of the three proposed fault detection methods, leads to the conclusion that quadratic time-frequency methods are the best suited for motor fault diagnostics. However all these methods assume that the extracted non-stationary motor current has time dependent frequency information which is true only to a certain limit of non-stationary operation (15 Hz of sinusoidal speed reference and 10 Hz of triangular speed reference). Even though this range represents most practical cases of motor operation, there are still applications that work outside this envelope. Beyond this envelope, the motor current no longer has any meaningful time-dependent frequency information. In such cases, other techniques that are based only on time may have to be used.

11.1.3.5 Fault Classification and Comprehensive BLDC Condition Monitoring Scheme

Once the fault frequencies are computed, the next step is to use the extracted frequency information to monitor the health of the motor. A simple root mean square (RMS) fault metric that could be used to monitor the health of the motor, is calculated by computing the root mean square value of the instantaneous amplitudes of the extracted fault frequencies. This measure allows the motor operator to evaluate the health of the

motor over time. As the motor's operating condition, namely the speed and the load vary continuously over time, the amplitudes of the fault frequency components vary too. For this reason, a threshold that can adapt to instantaneous operating conditions is needed for fault discrimination in motors operating under non-stationary conditions. In the present research, an adaptive heuristic threshold that varies at 2.5% of the amplitude of the fundamental frequency is able to effectively discriminate a good motor from a bad one. This threshold depends on the individual motor and varies from motor to motor.

The experience and information obtained in this research has also been put to use to finally suggest a comprehensive condition monitoring scheme that can both detect and identify specific rotor or load faults in BLDC motors. Though the proposed methods are not perfect, they can be improved and fine tuned for commercial implementation.

11.1.4 Commercial Viability of Using Motor Current Signature Analysis (MCSA) for BLDC Rotor Fault Detection

The measurement accuracy in the experiments conducted as part of this research is about $\pm$10%. Significant statistical data is needed to conclusively say that MCSA is a viable and robust fault detection technique for BLDC rotor fault detection. This statistical viability is defined in terms of Type I and Type II errors. A false positive, also called a Type I error, exists when a test incorrectly reports that it has found a positive (i.e. significant) result where none actually exists [101]. A false negative, also called a Type II error or miss, exists when a test incorrectly reports that a result was not detected, when it was really present [102]. A large amount of statistical data is needed to derive these error percentages, and has not been done in this research as the focus is to demonstrate new BLDC stator current based fault detection algorithms, assuming that the motor

current is an effective tool to detect faults. This assumption is made because of the widespread use of MCSA in motor fault detection for more than two decades [11, 13, and 33]. However, it is suggested that these statistical errors be evaluated before commercializing the algorithms proposed in this research for BLDC rotor fault detection.

11.1.5 Cost Trade-Offs in Electrical Diagnostics vs. Vibration-Based Diagnostics

Electrical-based fault detection of BLDC motors using either the stator current or voltage is suggested in this research as an attractive alternative to vibration-based diagnostics. Although vibration-based motor fault detection is reliable, it suffers from the following important limitations:

1. Accelerometers that are used to sense vibrations along with their wiring can be expensive. Good accelerometers may cost about a couple of hundred dollars.
2. The location of the accelerometer on the BLDC motor has to be carefully chosen so as to obtain the vibration signal. This path of least resistance between the origin of the vibration and the place of mounting of the accelerometer has to be chosen carefully.
3. Moreover, mounting a separate accelerometer on the motor may not be convenient in many applications.

Electrical-based diagnostics on the other hand, may not need an extra sensor. Most BLDC inverters have current and voltage sensors already built into them. The signal acquired by these sensors can be used for motor diagnostics. These inverters also have microprocessors or DSPs for motion control. The fault detection algorithm can be easily integrated into these pre-existing processors. In non-stationary motor fault detection, an adaptive filter such as a switch capacitor filter may be needed. However, these filters are inexpensive to implement. For example, a good switch capacitor filter would cost less

than five dollars. This cost can also be avoided, by implementing the adaptive filter digitally in the BLDC inverter's microprocessor/DSP. Therefore, electrical-based motor diagnostics typically do not need any additional components and could be much cheaper than vibration diagnostics.

11.2 Contributions

A paper titled "*Diagnosis of potential rotor faults in BLDC motors*" has been presented at the *Second Power Electronic, Machines and Drives Conference (PEMD)* in March 2004 in Edinburgh, UK [59]. This paper has also been submitted for review to the *IEEE Transaction on Power Electronics* and reports the research explained in Chapter 4.

Based on the research in Chapter 5, a paper titled "*Current/voltage based detection of faults in gears coupled to Brushless DC (BLDC) motors*" has been presented at the *International Electric Machines and Drives Conference* [103]. This paper has since been accepted for publication in the *IEEE Transactions on Industry Applications*.

The research of Chapters 7 - 9 has been presented or is in the process of publication through five conference papers [104-108]. This work has also been accepted for journal publication in the *IEEE Transaction on Industry Applications* [109]. One other paper has also been submitted for review to the *IEEE Transaction on Industrial Electronics* [107].

A summary paper on rotor fault diagnostics in permanent magnet machines titled "*On the detection of rotor faults in permanent magnet machines*" has been presented at the *Electric Machine Technology Symposium 2004* in Philadelphia, USA [110]. Similarly, the application of the work done as a part of this research, for monitoring faults

in electric drive train components in hybrid electric vehicles, has been presented at the 2006 SAE World Congress sponsored by the Society of Automotive Engineers [111].

The main contributions of this research to the field of electric machine condition monitoring are summarized as follows:

- An experimental study of the effect of BLDC rotor faults on motor terminal quantities namely, the stator current and the stator voltage, has been conducted.
- A method to detect gear faults and misalignments from the frequency spectrum of the BLDC current has been proposed.
    - A theoretical explanation for the occurrence of gear fault harmonics in motor current has been developed.
    - Practical gear faults such as damaged teeth and scoring have been implemented in the laboratory.
- Three algorithms for detecting rotor faults in BLDC motors operating in non-stationary conditions have been proposed. These methods are:
    - A windowed Fourier ridge (spectrogram) based fault-detection algorithm.
    - A quadratic TFR based fault-detection algorithm that has better frequency resolution than the spectrogram.
    - An analytic wavelet based fault-detection algorithm that can detect faults in non-stationary environments.
- The viability of using selected signal processing techniques for commercial implementation through a DSP development platform has been demonstrated.

- A simple RMS based metric for automatic fault-detection using an adaptive thresholding scheme has been developed.
- A smart fault classifier scheme using ANNs has been suggested for more accurate fault classification.
- Finally, a comprehensive rotor/load fault condition monitoring scheme for BLDC motors operating under both stationary and non-stationary conditions has been suggested.

11.3 Recommendations for Future Research

The purpose of a dissertation is to advance the science in a given field. After this objective is achieved, there is generally still much work remaining to implement this new knowledge into widespread application. Nevertheless, there is still additional work required to poise these new condition monitoring schemes for application in industry. Some of this work that could initiate interesting research in the future is as follows:

11.3.1 Investigating Different Kinds of Non-Stationary Operation

The non-stationary operation in this research is still rotational in nature, in other words the motor is rotating although with continuously changing speed and load conditions. This results in some amount of frequency information being preserved over time that can be extracted using time-frequency/time-scale techniques. But, what if the non-stationary is oscillating in nature or if the application is a servo motor (robotic) where the motor stops, spins partially, and works in extremely short bursts of operation. In the first case, there may be no meaningful fault frequency information and techniques such as wavelets or pattern recognition techniques such as ANNs may have to be used to learn and characterize the deviation of a faulty motor from a good one. In the latter case,

it may be impossible to use any frequency based technique as the time sample of operation may be too small to provide fine frequency resolution. Time-series techniques may be an option here. These are interesting cases and should be looked into more detail.

11.3.2 Non-Stationary Fault Diagnostics in other Permanent Magnet Motors

The research in this paper has been limited to BLDC motors with surface mount magnets. However, there are several other different kinds of permanent magnet motors which may result in different fault frequency characteristics in the stator current spectrum. For example, permanent magnet motors in hard disk drives have a permanent magnet stator with a wound rotor. Then, there are interior permanent magnet motors that represent non-salient rotor structures. The fault diagnostics in this case may be possible by monitoring the d- and q- axis currents instead of the abc currents. Other kinds of unique permanent magnet structures are pancake (axial-flux) motors, and even permanent magnet synchronous motors (PMSMs) with sinusoidally induced voltage waveforms.

11.3.3 Developing Voltage-Based Condition Monitoring

During the research into load fault detection in current controlled motors, it has been observed that these faults also generate harmonics in the stator voltage, and this could serve as an additional resource in fault detection in current (torque) control motors. This subject has to be investigated in detail. The mathematical relationships between the current and the voltage harmonics have to be developed. Both these harmonics are complimentary, in the sense that, in voltage source drives, the current harmonics dominate and in current source drives, voltage harmonics may dominate. Hence, diagnostic schemes that utilize the fault information in both the current and voltage may provide a more reliable indication of motor fault and should be investigated further.

11.3.4 Smart Non-Stationary Fault Classifiers

Fault classification is as important as fault feature extraction. In this research, a simple RMS based fault classifier with a heuristic adaptive threshold has been used to classify motor faults in non-stationary operating conditions. This may not be accurate, as the magnitudes of the fault components depend on both the instantaneous speed as well as the instantaneous load conditions. Under these circumstances, intelligent classifiers are needed that adapt the fault discriminating threshold based on the instantaneous load and speed conditions, thereby providing a more accurate fault classification.

Moreover, such classifiers can intelligently learn the characteristics of a good motor and track the deviation in the fault frequency amplitudes to monitor the motor health. Such intelligent fault classifiers are possible using techniques such as artificial neural networks (ANNs) and self-organizing maps [112, 113]. One possible scheme for using ANNs as a fault classifier for non-stationary BLDC motor fault diagnostics is shown in Figure 11.1. Typically such a classifier is organized as follows:

11.3.4.1 ANN Model and Offline Training

The first step in using an ANN classifier for motor fault diagnostics is to select an ANN model and its inputs. For performing diagnostics on a BLDC motor, these inputs could be selected as the inverter's DC link current (I_{dc}) which is directly proportional to load torque and the speed (w). Based on these inputs, the ANN is trained offline, such that the output of the ANN estimates the RMS metric of the instantaneous fault frequencies of a good motor. Commonly used training algorithms such as back propagation can be used. The number of neurons and the number of inner layers needed are typically chosen through trial and error.

11.3.4.2 ANN Fault Classification and Online Adaptation

The output of the ANN trained in the previous step is continuously compared to the actual RMS metric of the instantaneous fault frequencies in real-time. A significant deviation indicates a progressing fault on the BLDC motor. As it is almost impossible to train an ANN offline for every possible speed and load operating points, the ANN must be able to adapt and learn the characteristics of the motor online in real-time. Hence, online training of the ANN is needed to update the model in real-time as new load and speed conditions are encountered.

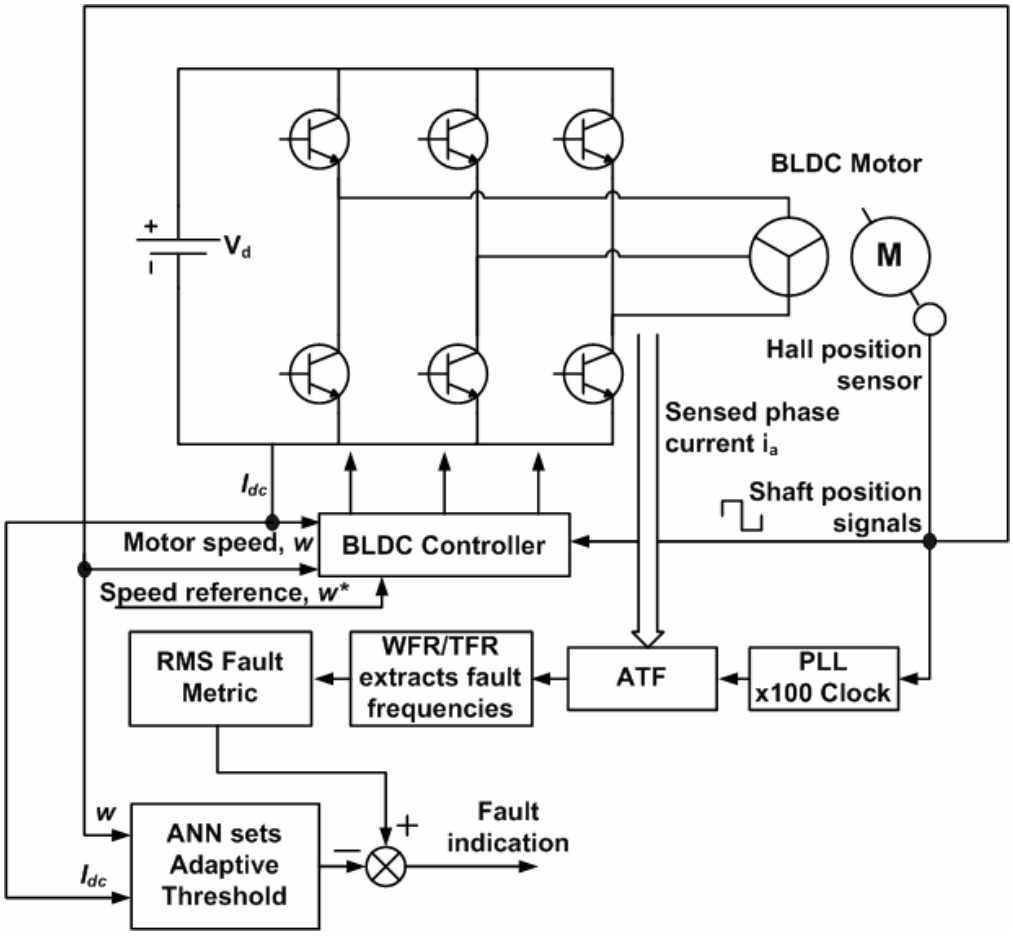

Figure 11.1: ANN based fault classifier for BLDC motor fault detection.

11.3.5 Expansion to Other Faults

The non-stationary fault-detection schemes can be extended to other kinds of faults, both rotor as well as stator. In permanent magnet rotor faults, damaged rotor magnets and bearing defects are other significant faults. In induction motors, broken rotor bars are common and develop fault frequencies close to the fundamental frequency. This requires high frequency resolution, which conventional time-frequency techniques such as windowed Fourier transforms may not be able to detect. High frequency non-stationary signal analysis techniques such as newer quadratic time-frequency methods like the Zhao-Atlas-Marks distributions or adaptive filtering techniques may have to be used. Non-stationary stator winding fault-detection is another open topic. Artificial neural networks may be used to learn the pattern of the negative sequence components in stator currents in this case.

11.3.6 Non-stationary Motor Fault Detection Using Synchronous Reference Frame Transformation

The digital PLL developed in Chapter 7 produces 100 pulses for every 120 degree rotation of the rotor. This in effect produces about 300 pulses per motor revolution. This high resolution instantaneous frequency information can be used to transform the motor fault frequencies to a synchronous reference frame. For example, in a six-pole BLDC motor with dynamic eccentricity, the fault frequencies are given by $2f_e/3$ and $4f_e/3$, where f_e is the fundamental frequency. As the fundamental frequency is tracked by the PLL, the $2f_e/3$ and $4f_e/3$ fault frequencies are known accurately. The phase currents of the BLDC motor can then be transformed to two synchronous frames, one rotating at $2f_e/3$ and the other rotating at $4f_e/3$. The effect of the synchronous frame transformation is that the

fault frequencies $2f_e/3$ and $4f_e/3$ are transformed to dc components in their respective synchronous frames. Monitoring the amplitude of the dc component can then indicate the health of the BLDC motor. This method is promising as it has the potential to replace the complicated t-f distributions proposed in this research with a simple alternative. The practical issues regarding the implementation of this method have to be looked into in detail.

APPENDIX A

ANALOG SPEED CONTROLLER

The analog speed controller is designed to complement the BLDC motor controller provided by Delphi Inc., and is used in this research. The BLDC controller incorporates an inverter and a current controller, but lacks a speed controller. The analog speed controller is built around the voltage-to-frequency converter integrated circuit, VFC 32 [114]. The square-wave output from a 1000 ppr optical encoder is used as an input to the VFC 32. The VFC 32 converts the frequency of the encoder's pulse output into a voltage signal. This voltage signal is then used as an input to an operational amplifier based analog proportional-integral (PI) controller. The Delphi BLDC controller needs two inputs from the speed controller for interfacing:

T1 = BLDC control signal 1 (< 2.5 V)

T2 = BLDC control signal 2 (5 – T1 V)

These signals are provided using operational amplifiers. The circuit schematic of the analog speed controller is shown in Figure A.1. The connection diagram is shown in Figure A.2. The speed reference signal is set through a potentiometer in the circuit.

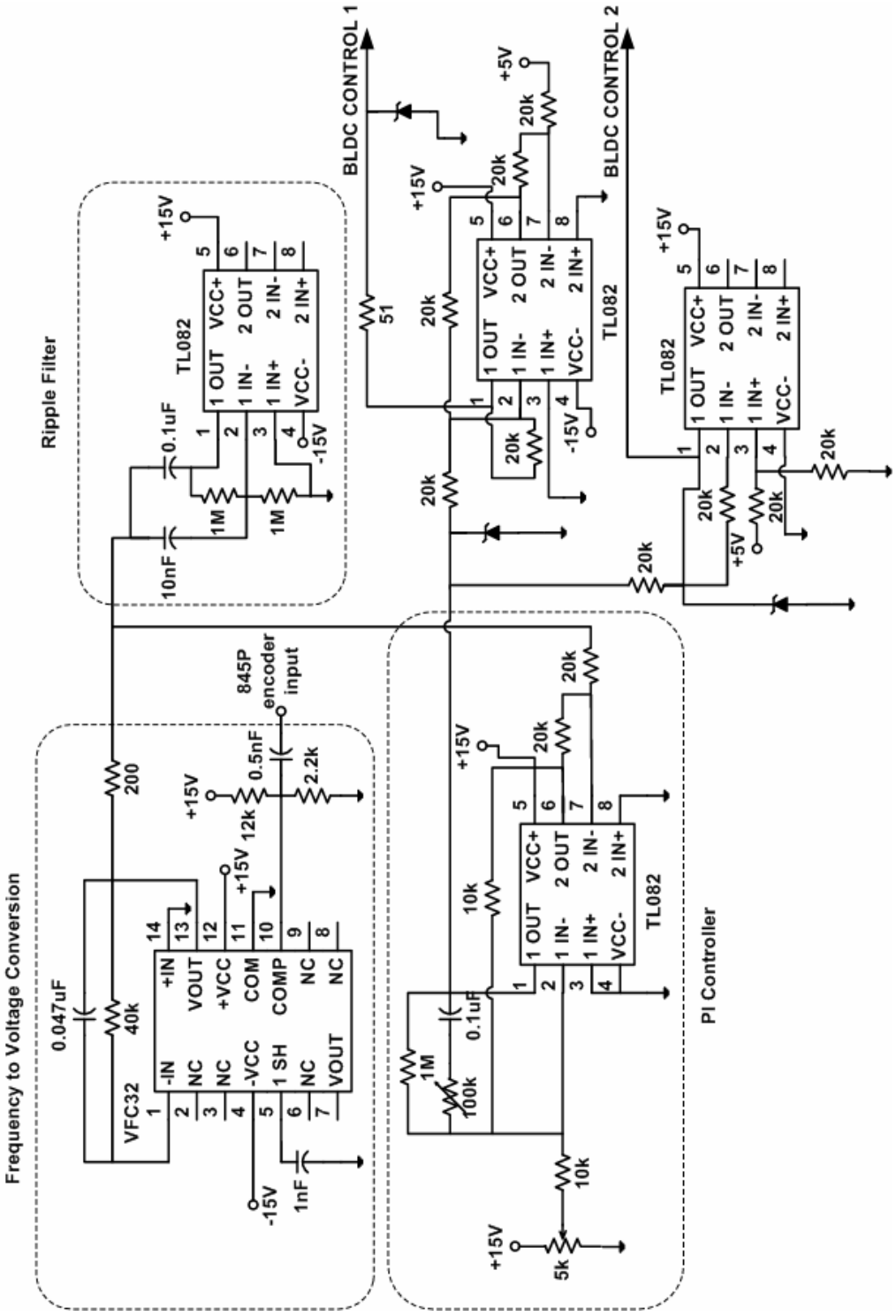

Figure A.1: Circuit schematic of analog speed controller.

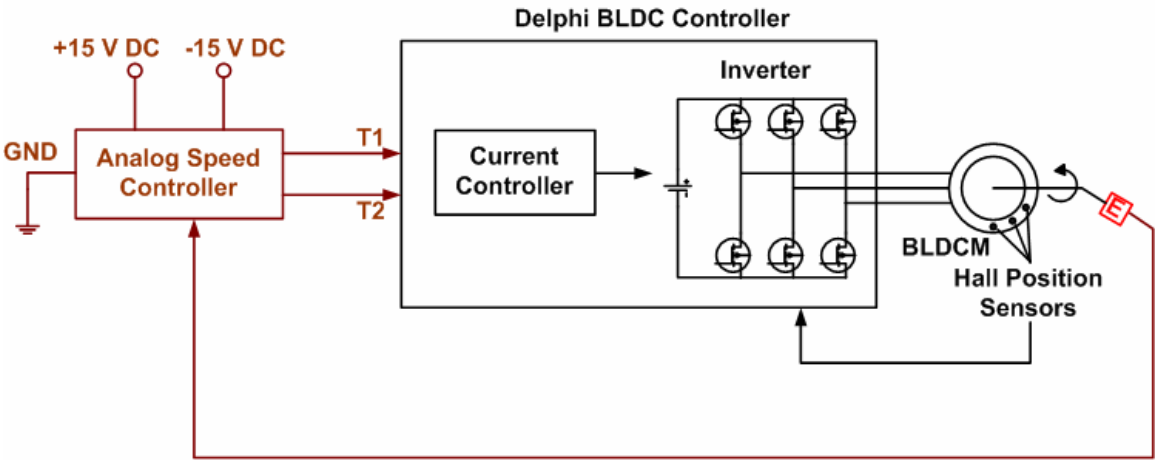

Figure A.2: Analog speed controller connection diagram.

APPENDIX B

QUANTIFYING PULSATING LOAD POWER

There are several ways a pulsating load can be quantified. They can be described in terms of the load torque ripple or in percentage of pulsating power. The latter approach is used here and is explained as follows. It is assumed that V is the terminal dyno voltage. With reference to Figure 4.9, R_{fload} is the fixed resistance, and R_{pload} is the pulsating resistor switching at 50% duty cycle.

The total DC load power ($P_{DCpower}$) output by the dyno is

$$P_{DCpower} = \frac{V^2}{R_{fload}} + \frac{V^2}{4R_{pload}}. \tag{B.1}$$

The pulsating power of the load is contributed by the pulsating AC component because of the switching R_{pload} and is calculated as

$$P_{pulse} = \frac{V_{rmspulse}^2}{R_{pload}} = \frac{2V^2}{\pi^2 R_{pload}} \quad . \tag{B.2}$$
$$as\ V_{rmspulse} = \frac{\sqrt{2}V}{\pi}\ for\ a\ square\ wave$$

The percentage of the pulsating AC power to the total DC power is then calculated as

$$\%\ pulsed\ power = \frac{P_{pulse}}{P_{DCpower}} = \frac{8R_{fload}}{\pi^2\left(4R_{pload} + R_{fload}\right)}. \tag{B.3}$$

The load torque can be optionally calculated as follows:

The total power output by DC generator is

$$P_{gen} = P_{DCpower} + P_{pulse}. \tag{B.4}$$

Assuming fixed armature output voltage (reasonable assumption), the armature current of DC gen is

$$I_a = \frac{P_{gen}}{E_f}, \tag{B.5}$$

where E_f is the open-circuit armature terminal voltage. Thepulsed current and the DC generator current are given by,

$$I_{gen\_pulsed} = \frac{P_{pulse}}{E_f} \ and \ I_{gen\_DC} = \frac{P_{DCpower}}{E_f}. \tag{B.6}$$

Now, E_f is calculated as in (B.7)

$$E_f = K * I_f * \omega, \tag{B.7}$$

where ω is the speed (rad/s) and I_f is the field amps. TheDC motor torque constant, K, can be calculated from open-circuit measurements. Also, the torque is

$$T = K * I_f * I_a. \tag{B.8}$$

The pulsed and DC torque can be calculated from

$$T_{pulsed} = K * I_f * I_{gen\_pulsed} \ and \ T_{DC} = K * I_f * I_{gen\_DC}. \tag{B.9}$$

The total torque output by BLDC motor is therefore given by

$$T_{BLDC} = T_{pulsed} + T_{DC}\,. \tag{B.10}$$

Therefore, by varying R_{fload} and R_{pload}, any amount of desired torque pulsation can be obtained.

APPENDIX C

WINDOWED FOURIER RIDGE THEOREM

The WFR algorithm is based on the following theorem which relates $Sf(t,\xi)$ to the instantaneous frequency of s [68]

Theorem. *Let* $s(t) = a(t)\cos\varphi(t)$. *If* $\xi \geq 0$ *then*

$$\left\langle f, g_{s_l,t,\xi} \right\rangle = \frac{\sqrt{s_l}}{2} a(t) \exp\left(i\left[\varphi(t) - \xi t\right]\right)\left(\hat{g}\left(s_l\left[\xi - \varphi'(t)\right]\right) + \varepsilon(t,\xi)\right). \tag{C.1}$$

The corrective term satisfies

$$\left|\varepsilon(t,\xi)\right| \leq \varepsilon_{a,1} + \varepsilon_{a,2} + \varepsilon_{\varphi,2} + \sup_{|\omega| \geq s_l \varphi'(\tau)} \left|g'(\omega)\right|. \tag{C.2}$$

with

$$\varepsilon_{a,1} \leq \frac{s_l \left|a'(t)\right|}{\left|a(t)\right|}, \quad \varepsilon_{a,2} \leq \sup_{|\tau - t| \leq s_l/2} \frac{s_l^2 \left|a''(\tau)\right|}{a(t)}. \tag{C.3}$$

And if $s_l \left|a'(t)\right| \left|a(t)\right|^{-1} \leq 1$, *then*

$$\varepsilon_{\varphi,2} \leq \sup_{|\tau - t| \leq s_l/2} s_l^2 \left|\varphi''(\tau)\right|. \tag{C.4}$$

If $\xi = \varphi'(t)$ *then*

$$\varepsilon_{a,1} \le \frac{s_l \left|a'(t)\right|}{\left|a(t)\right|} \left|\hat{g}'\left(2s_l \varphi'(t)\right)\right|. \tag{C.5}$$

where $g(\tau)$ *is a real symmetric window with a Fourier transform of* $\hat{g}$ *and* $g_s(\tau)=s_l^{-1/2} g(\tau/s_l)$ *with a support of size* **s** *and a norm of unity.*

Expressions (C.3) and (C.4) show that the three corrective terms $\varepsilon_{a,1}$, $\varepsilon_{a,2}$, and $\varepsilon_{\varphi,1}$ are small if *a(t)* and *φ'(t)* have small relative variations over the support of the window g_s. The term $\sup_{|\omega| \ge s_l \varphi'(t)} \left|g'(\omega)\right|$ is negligible if $\varphi'(t) \ge \frac{\Delta\omega}{s_l}$, where $\Delta\omega$ is the bandwidth of the window $\hat{g}$.

Thus the corrective term $\varepsilon(t,\xi)$ can be neglected in (C.1). Since $\left|\hat{g}(\omega)\right|$ is a maximum at $\omega = 0$, (C.4) shows that for each *u* the spectrogram $\left|Sf(t,\xi)\right|^2 = \left|\left\langle s, g_{s_l,t,\xi} \right\rangle\right|^2$ is a maximum at $\xi = \varphi'(t)$. *The corresponding time-frequency points (t,* ξ(t)) are called ***ridges***. The ridge frequency gives the instantaneous frequency $\xi(t) = \varphi'(t)$ and the amplitude is then calculated as follows

$$a(t) = \frac{2\left|Sf(t,\xi(t))\right|}{\sqrt{s_l}\left|\hat{g}(0)\right|}. \tag{C.6}$$

If $\Phi_S(t,\xi)$ is the complex phase of $Sf(t,\xi)$, then it can be proven from [68] that the ridge points are points of stationary phase:

$$\frac{\partial \Phi_S(t,\xi)}{\partial t} = \varphi'(t) - \xi = 0. \tag{C.7}$$

APPENDIX D

ANALOG TRACKING FILTER

The switch capacitor filter and the PLL circuit are integrated onto a single printed circuit board (PCB) to obtain the best performance. This is necessary, as filter circuits are susceptible to parasitic capacitances and inductances. Surface mount components are used to minimize the trace lengths. The PCB is a four-layer board, designed using the software Eagle, and is fabricated at PCBExpress (www.pcbexpress.com). Two isolated non-overlapping ground planes are used, one for the digital circuit comprising the PLL, and the other for the analog filter circuits. The two planes are connected at a single point. Adequate decoupling is provided using 0.1 μF ceramic capacitors at all the power points in every integrated circuit package. Additional 1 μF and 10 μF Tantalum capacitors are also provided for good power supply regulation. The analog filter circuit and the PLL clock circuit are placed on opposite sides of the PCB to ensure the shortest possible clock trace. One-percent resistors and NPO ceramic capacitors are used for accuracy and temperature stability. The schematic of the complete circuit is shown in Figure D.1. The top and bottom sides of the PCB are shown in Figures D.2 and D.3. The filter provides 56 dB notch attenuation. The harmonics that are greater than the second are attenuated by more than 80 dB. The PLL circuit tracks the fundamental frequency from about 35 Hz to 210 Hz.

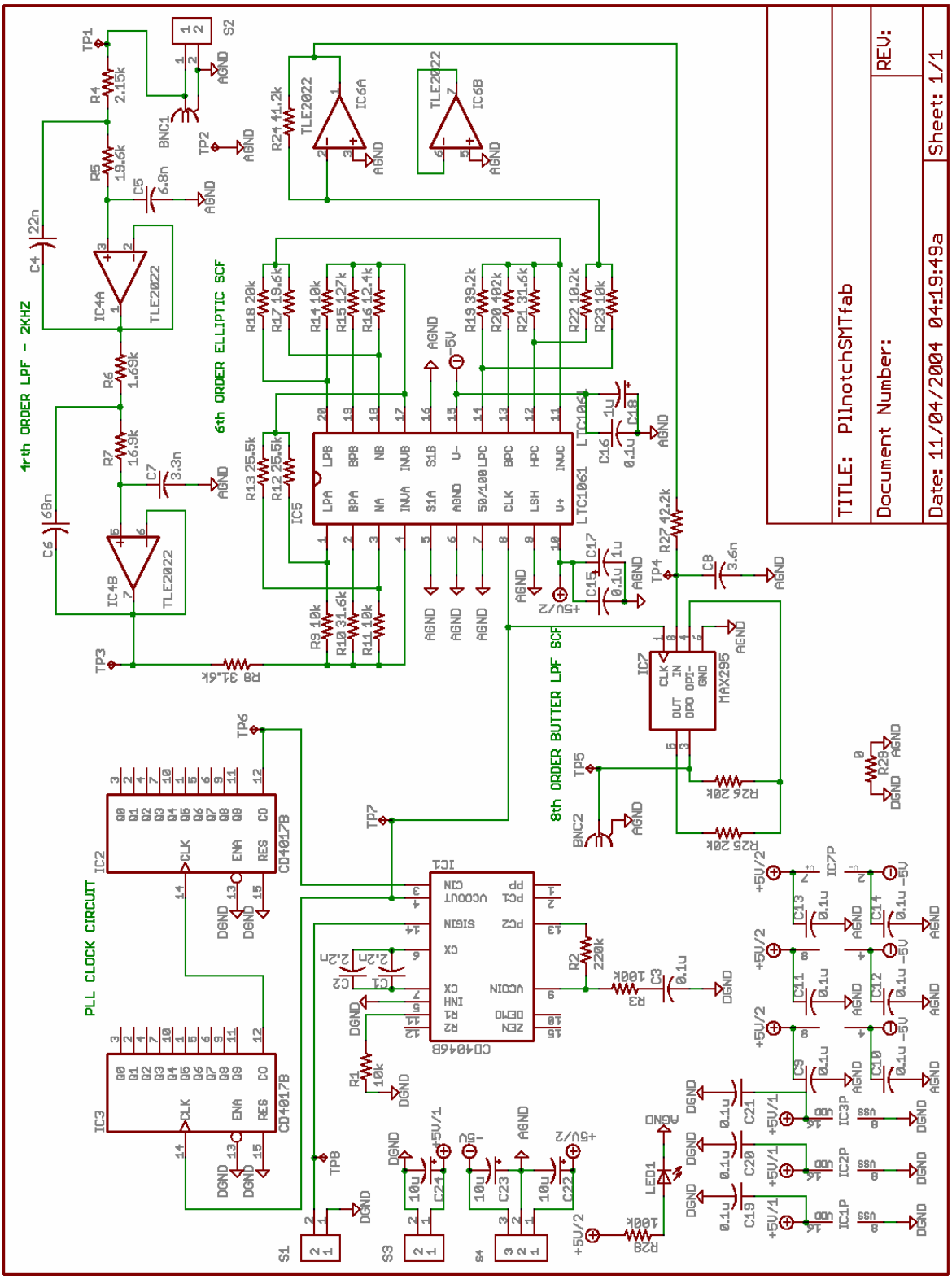

Figure D.1: Circuit schematic of ATF.

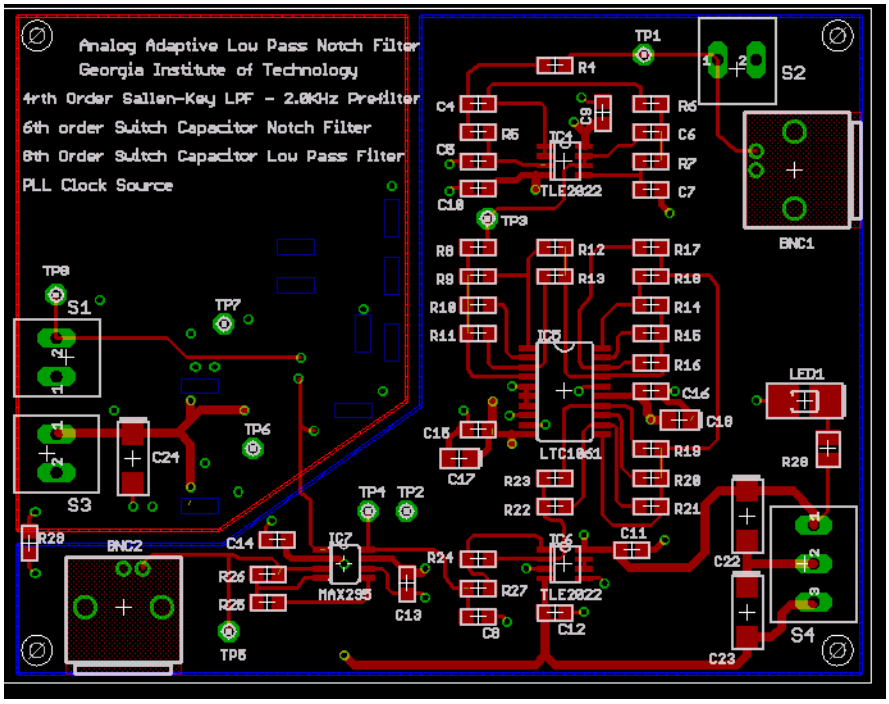

Figure D.2: ATF printed circuit board layout (Top side).

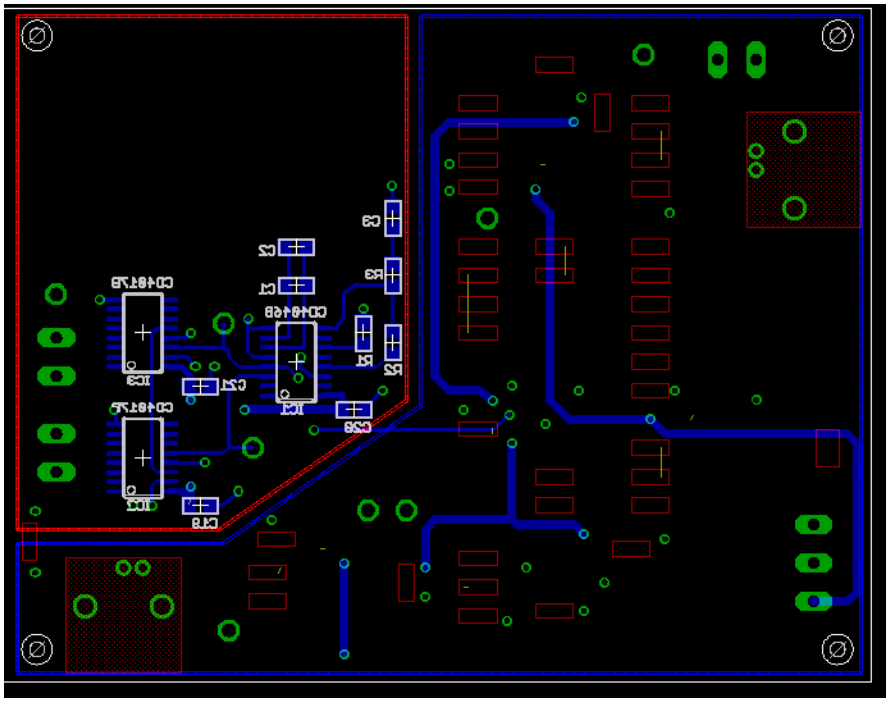

Figure D.3: ATF printed circuit board layout (Bottom side).

APPENDIX E

C CODES FOR TFR IMPLEMENTATION ON ADSP-21061

C Code Section to Implement WFT

```
void main ( void )
{
      /* Initialize windowed sequence to zero */
      for (i = 0; i < N ; i++)
    {
     wfreal_output[i] = 0;
     wfimag_output[i] = 0;
     }

     /* Generating Gaussian window of length L */
    gen_gaussian(w, 2.5, 1, 2*L+1);

    /*for (n = 0; n < N;  n++)
    { */
    n=700;
      /* Midlle of window index */
      m = L;

      /* End of window index */
      q = 2*L;

      /* Compute actual length of window to acount for insufficient */
      /* data lengths at ends of data                               */
      Mmin = min (n,L);
      Mmax = min (0,N-n-L);
      k=n;
      for (i = m-Mmin; i <= q-Mmax ; i++)
      {
      wfreal_input[k] = real_input[k]*w[i];
      wfimag_input[k] = imag_input[k]*w[i];
      k++;
      }

      /* Compute FFT of windowed sequence */
      cfft1024 (wfreal_input, wfimag_input, wfreal_output,
wfimag_output);

      /* Calculate magnitude of spectrum */
            for (i = 0; i < N ; i++)
      {
      wf[i] =
sqrt(wfreal_output[i]*wfreal_output[i]+wfimag_output[i]*wfimag_output[i
]);
      }

      /* Local maxima computation - ridge detection */
```

```
      /* } */
      exit(0);
}
```

C Code Section to Implement PWVD

```
#define     M_2PI 6.283185307179586477
#include"fircoef.h"           /* Coefficients for Hilbert Transform */


#define TAPS      81                /* Hilbert's Filter length */
#define SAMPLES   1024        /* Buffer Length */
#define     LEN         1024
#define     LENT  8
#define     TIME_M      1100        /* After getting 1100 samples we
                                              start obtaining the WVD
*/

int done=0, done_t=0;         // for ezktv2a_com0
float dm y,dline[TAPS+1],tindex[30];
float fr[LEN],fi[LEN],fx[LEN/2],fy[LEN/2];
float WVr[LENT][LEN/2],WVi[LENT][LEN/2];
main()
{
 int i, j, k, c1,c2=0,c3,c4;

// first we initialize the data
 for(i=0;i<TAPS+1;i++)
  dline[i]=0;

 c1=1024-41;      // this index takes into account the filter's delay

 // Each data sample should pass through the fir filter
 // This algorithm can be arranged to produce a WVD time slice
 // after acquiring a new data sample. In here we just wait
 // for M samples to be acquired before start measuring the WVD
 // then we process two time slices at once

 done=1;                      // this should be 1 for ezktv2a_com0
 i=0;
 do
  {
//   y=sin(M_2PI*i*20.0/1024.0)+sin(M_2PI*i*40.0/1024.0);   // New data
input
   fr[c2]=y;
   y=fir(y, coefs, dline, TAPS); // Hilbert transformation
   c1 = circindex(c1, 1, LEN);    // Increment the index
   c2 = circindex(c2, 1, LEN);
   fi[c1]=-y;   // now we have the analytic function

   if(i>TIME_M)
    {
     set_flag(SET_FLAG1, CLR_FLAG);
     // Here we build the auto-correlation
```

```
     c3=circindex(c1,-512,LEN);
     c4=circindex(c1,-512,LEN);

     for(j=1;j<=LEN/2;j++)
      {
       fx[j-1]=fr[c3]*fr[c4]+fi[c3]*fi[c4];
       fy[j-1]=fi[c3]*fr[c4]-fi[c4]*fr[c3];
       c3=circindex(c1,j,LEN);
       c4=circindex(c1,-j,LEN);
      }
     // we wait for new data since we are processing two
     // time slices at once
     set_flag(SET_FLAG1, SET_FLAG);
     i++;
     y=sin(M_2PI*i*20.0/1024.0)+sin(M_2PI*i*40.0/1024.0);   // New data
input
     fr[c2]=y;
     y=fir(y, coefs, dline, TAPS); // Hilbert transformation
     c1 = circindex(c1, 1, LEN);    // Increment the index
     c2 = circindex(c2, 1, LEN);
     fi[c1]=-y;   // now we have the analytic function
     // here we build the auto-correlation
     c3=circindex(c1,-512,LEN);
     c4=circindex(c1,-512,LEN);
     for(j=1;j<=LEN/2;j++)
      {
       fy[j-1]+=(fr[c3]*fr[c4]+fi[c3]*fi[c4]);
       fx[j-1]-=(fi[c3]*fr[c4]-fi[c4]*fr[c3]);
       c3=circindex(c1,j,LEN);
       c4=circindex(c1,-j,LEN);
      }
     // Here we get the WVD for two time slices one in the real part
and
     // other in the imag part
     cfft512(fx,fy,WVr[k],WVi[k]);
     k++;
     i = TIME_M;
    }
   i++;
  }while (i<TIME_M+2*LENT);

 done_t=5;   // this should be 5 for ezktv2a_com0
 for(;;)
  {
      asm("nop;");
  }
}
```

Courtesy: Prof. Jose Restrepo (Univ. Simon Bolivar)

C Code Section to Implement CWD

```
#define     M_2PI 6.283185307179586477
#include"fircoef.h"           /* Coefficients for Hilbert Transform */
```

```
#define TAPS      81               /* Hilbert's Filter length */
#define SAMPLES   1024        /* Buffer Length */
#define     LEN         1024
#define     LENT  8
#define     TIME_M      1100        /* After getting 1100 samples we
                                          start obtaining the WVD
*/
#define     NK          1024
#define     MK          128

int done=0, done_t=0;         // for ezktv2a_com0
float dm y,dline[TAPS+1],tindex[30];
float fr[LEN],fi[LEN],fx[LEN/2],fy[LEN/2];
float WVr[LENT][LEN/2],WVi[LENT][LEN/2];
float ker[NK][MK]; // the kernel is both an even and real function

main()
{
 int i, j, k, c1,c2=0,c3,c4;

// first we initialize the data
 for(i=0;i<TAPS+1;i++)
  dline[i]=0;

// then we calculate the kernel
 for(j=0;j<NK/4;j++)
  {
   J0=2*j*(M_2+1);
   J1=J0+(M_2+1);
   for(i=0;i<=MK/2;i++)
    {
     r[J0+i]=(float)Ev_Fun2(stack2,contb,(double)i,(double)j*2.);
     r[J1+i]=(float)Ev_Fun2(stack2,contb,(double)i,(double)(2.*j+1.));
    }
  }
 c1=1024-41;      // this index takes into account the filter's delay

 // Each data sample should pass through the fir filter
 // This algorithm can be arranged to produce a WVD time slice
 // after acquiring a new data sample. In here we just wait
 // for M samples to be acquired before start measuring the WVD
 // then we process two time slices at once

 done=1;                      // this should be 1 for ezktv2a_com0
 i=0;
 do
  {
   y=sin(M_2PI*i*20.0/1024.0)+sin(M_2PI*i*40.0/1024.0);     // New data
input
   fr[c2]=y;
   y=fir(y, coefs, dline, TAPS); // Hilbert transformation
   c1 = circindex(c1, 1, LEN);    // Increment the index
   c2 = circindex(c2, 1, LEN);
   fi[c1]=-y;   // now we have the analytic function

   if(i>TIME_M)
```

```
    {
     // Here we build the auto-correlation
     c3=circindex(c1,-512,LEN);
     c4=circindex(c1,-512,LEN);

     for(j=1;j<=LEN/2;j++)
      {
       fx[j-1]=fr[c3]*fr[c4]+fi[c3]*fi[c4];
       fy[j-1]=fi[c3]*fr[c4]-fi[c4]*fr[c3];
       c3=circindex(c1,j,LEN);
       c4=circindex(c1,-j,LEN);
      }
     // we wait for new data since we are processing two
     // time slices at once
     i++;
     y=sin(M_2PI*i*20.0/1024.0)+sin(M_2PI*i*40.0/1024.0);   // New data
input
     fr[c2]=y;
     y=fir(y, coefs, dline, TAPS); // Hilbert transformation
     c1 = circindex(c1, 1, LEN);    // Increment the index
     c2 = circindex(c2, 1, LEN);
     fi[c1]=-y;   // now we have the analytic function
     // here we build the auto-correlation
     c3=circindex(c1,-512,LEN);
     c4=circindex(c1,-512,LEN);
     for(j=1;j<=LEN/2;j++)
      {
       fy[j-1]+=(fr[c3]*fr[c4]+fi[c3]*fi[c4]);
       fx[j-1]-=(fi[c3]*fr[c4]-fi[c4]*fr[c3]);
       c3=circindex(c1,j,LEN);
       c4=circindex(c1,-j,LEN);
      }
     // Here we get the WVD for two time slices one in the real part
and
     // other in the imag part
     cfft512(fx,fy,WVr[k],WVi[k]);
     k++;
    }
   i++;
  }while (i<TIME_M+2*LENT);

 done_t=5;   // this should be 5 for ezktv2a_com0
 for(;;)
  {
      asm("nop;");
  }
}
```

Courtesy: Prof. Jose Restrepo (Univ. Simon Bolivar)

REFERENCES

[1] MICROCHIP TECHNOLOGY, “Brushless DC (BLDC) motor fundamentals.,” Application note, AN885, 2003.

[2] N. BIANCHI, S. BOLOGNANI, and M. ZIGLIOTTO, “Analysis of PM synchronous motor drive failures during flux weakening operation,” in Proc. 27th Annual IEEE Power Electronics Specialist Conference - PESC'96, 1996, pp. 1542-1548.

[3] M. H. HAYES, Statistical Digital Signal Processing and Modeling. New York: John Wiley & Sons, ISBN: 0471594318, 1996.

[4] T. M. JAHNS, “Variable frequency permanent magnet AC machine drives,” in Power Electronics and Variable Frequency Drives: Technology and Applications. B. K. Bose (ed.), Piscataway, NJ: IEEE Press, ISBN: 81-86308-74-1, 1996.

[5] N. MOHAN, Electric Drives – An Integrative Approach. Minnesota: MNPERE, ISBN: 0-9663530-1-3, 2001.

[6] A. KUSKO and S. M. PEERAN, “Definition of the brushless DC motor,” in Proc. IEEE-IAS Annual Meeting, 1988, pp. 20-22.

[7] T. J. E. MILLER, Brushless PM and Reluctance Motor Drives. Oxford: Clarendon Press, ISBN: 0198593694, 1989.

[8] P. J. TAVNER and J. PENMAN, Condition Monitoring of Electrical Machines. Hertfordshire, England: Research Studies Press Ltd, ISBN: 0863800610, 1987.

[9] J. A. HAYLOCK, B. C. MECROW, A. G. JACK, and D. J. ATKINSON, “Operation of Fault Tolerant Machines with Winding Failures,” IEEE Trans. Energy Convers., vol. 14, no. 4, pp.1490-1495, 1999.

[10] R. R. OBAID, “Detection of rotating mechanical assymetries in small induction machines,” Georgia Institute of Technology, Atlanta, GA, Ph.D. Thesis, pp. 28-29, 2003.

[11] J. M. CAMERON, W. T. THOMSON, and A. B. DOW, “Vibration and current monitoring for detecting airgap eccentricity in large induction motors,” IEE Proceedings, vol. 133, pt. B, no. 3, pp.155-163, 1986.

[12] M. BRADFORD, “Unbalanced magnetic pull in a 6-pole induction motor,” IEE Proceedings, vol. 115, no. 11, pp. 1619-1627, 1968.

[13] D. G. DORELL, W. T. THOMSON, and S. ROACH, “Analysis of airgap flux, current, and vibration signals as a function of the combination of static and

dynamic airgap eccentricity in 3-phase induction motors," IEEE Trans. Ind. Appl., vol. 33, no. 1, pp.24-34, 1997.

[14] S. K. PAL, "Direct drive high energy permanent magnet brush and brushless dc motors for robotic applications," in Proc. IEE Colloquium on 'Robotic Actuators, 1991, pp.12/1-12/4.

[15] S. K. PAL, "Design criteria for brushless dc motors with hollow rotor of samarium cobalt for applications above 25000 rpm in vacuum," in Proc. 5th International Conference on Electrical Machines and Drives, 1991, pp.115-120.

[16] R. FISHER, "Design and cost considerations for permanent magnet dc motor applications," Power Conversion and Intelligent Motion Control, vol. 17, pp.18-24, 1991.

[17] MOTOR RELIABILITY WORKING GROUP, "Report on Large Motor Reliability Survey of Industrial and Commercial Installations, Part I," IEEE Trans. Ind. Appl., vol. IA-21, no. 4, pp.853-864, 1985.

[18] S. NANDI and H. A. TOLIYAT, "Condition Monitoring and Fault Diagnosis of Electrical Machines – A Review," in Proc. 34th Annual Meeting of the IEEE Industry Applications, 1999, pp. 197-204.

[19] J. S. HSU and J. STEIN, "Shaft Signals of Salient-Pole Synchronous Machines for Eccentricity and Shorted-Field_Coil Detections," IEEE Trans. Energy Convers., vol. 9, no. 3, pp.572-578, 1994.

[20] G. DALPIAZ and U. MENEGHETTI, "Monitoring fatigue cracks in gears," NDT & E International, vol. 24, issue 6, pp.303-306, 1991.

[21] W. J. WANG and P. D. MCFADDEN, "Early detection of gear failure by vibration analysis--ii. interpretation of the time-frequency distribution using image processing techniques," Mechanical Systems and Signal Processing, vol. 7, issue 3, pp.205-215, 1993.

[22] B. A. PAYA, I. I. ESAT and M. N. M. BADI, "Artificial neural network based fault diagnostics of rotating machinery using wavelet transforms as a preprocessor," Mechanical Systems and Signal Processing, vol. 11, issue 5, pp.751-765, 1997.

[23] W. WANG, "Early detection of gear tooth cracking using the resonance demodulation technique," Mechanical Systems and Signal Processing, vol. 15, issue 5, pp.887-903, 2001.

[24] F. BUCHSBAUM, Design and Application of Small Standardized components. Data Book 757, Vol. 2, Stock Drive Products, ISBN: 0960987819, 1983.

[25] N. P. CHIRONIS (editor), Gear Design and Application. New York: McGraw-Hill Book Co., Inc., ISBN: 0070107874, 1967.

[26] D. W. DUDLEY, Gear Handbook. New York: McGraw-Hill Book Co., Inc., ISBN: 0070179034, 1962.

[27] J. E. SHIGLEY and C. R. MISCHKE, Mechanical Engineering Design. New York: McGraw-Hill Book Co., Inc., ISBN: 0072921935, 1989.

[28] J. D. SMITH, Gears and their Vibration: A Basic Approach to Understanding Gear Noise. New York, NY: Marcel Dekker, Inc., ISBN: 082471797X, 1983.

[29] R. K. MOBLEY, An Introduction to Predictive Maintenance. New York: Van Nostrand Reinhold, ISBN: 0442318286, 1990.

[30] R. R. SCHOEN, "On-line current-based condition monitoring of three-phase induction machines," Georgia Institute of Technology, Atlanta, GA, Ph.D. Thesis, 1994.

[31] P. MILANFAR and J. H. LANG, "Monitoring the Thermal Condition of Permanent-Magnet Synchronous Motors," IEEE Trans. Aerosp. Electron. Syst., vol. 32, no. 4, pp.1421-1429, 1996.

[32] J. R. STACK, "Fault signature detection for rolling element bearings in electric machines," Georgia Institute of Technology, Atlanta, GA, Ph.D. Thesis, 2002.

[33] G. B. KLIMAN and J. STEIN, "Methods of motor current signature analysis," Electric Machines and Power Systems, vol. 20, no. 5, pp. 463-474, 1992.

[34] C. M. RILEY, B. K. LIN, T. G. HABETLER, and G. B. KLIMAN, "Stator Current Harmonics and Their Causal Vibrations: A Preliminary Investigation of Sensorless Vibration Monitoring Applications," IEEE Trans. Ind. Appl., vol. 35, no. 1, pp.94-99, 1999.

[35] C. M. RILEY, "Current-based sensorless vibration monitoring of small AC machines," Georgia Institute of Technology, Atlanta, GA, Ph.D. Thesis 1998.

[36] W. LE ROUX, "On-line detection of rotor faults in permanent magnet machines using only terminal quantities," Georgia Institute of Technology, Atlanta, GA, Ph.D. Thesis, 2002.

[37] C. KRAL, T. G. HABETLER, and R. G. HARLEY, "Detection of mechanical imbalances of induction machines without spectral analysis of time-domain signals", IEEE Trans. Ind. Appl., vol. 40, issue 4, pp. 1101–1106, 2004.

[38] WILCOXON RESEARCH, MD. Gearbox tutorial. [Online]. Available: http://www.wilcoxon.com/knowdesk/gear.pdf, Last Accessed: 17 June, 2006.

[39] R. B. RANDALL, “A new method for modeling gear faults,” ASME Journal of Mechanical Design 104, pp. 259-267, 1982.

[40] P. D. MCFADDEN, “Low frequency vibration generated by gear tooth impacts,” NDT International, pp. 279-282, 1985.

[41] H. B. ATTIA, B. DAGUES, J. C. HAPIOT, and I. S. BELKHODJA, “A contribution to the detection and the localization of the failures of a mechanical load driven by an induction motor,” ___.

[42] B. D. FORRESTER, “Use of the Wigner–Ville distribution in helicopter transmission fault detection,” in Proc. Australian Symposium on Signal Processing and Applications -ASSPA-89, 1989, pp. 17.-19.

[43] B. D. FORRESTER, “Analysis of gear vibrations in the time-frequency domain,” in Proc. 44th Meeting of the Mechanical Failures Prevention Group of the Vibration Institute, 1989, pp. 225-239.

[44] B. D. FORRESTER, “Time–frequency analysis in machine fault detection,”in Time–Frequency Signal Analysis. B. Boashash (ed.), Melbourne: Longman Cheshire, pp. 406-423, 1992.

[45] P. D. MCFADDEN and W. J. WANG, “Time–frequency domain analysis of vibration signals for machinery diagnostics (1) - introduction to the Wigner–Ville distribution,” Department of Engineering Science, University of Oxford, Report No. OUEL1859/90, 1990.

[46] P. D. MCFADDEN and W. J. WANG, “Time–frequency domain analysis of vibration signals for machinery diagnostics (2) – The weighted Wigner–Ville distribution,” Department of Engineering Science, University of Oxford, Report No. OUEL1891/90, 1991.

[47] P. D. MCFADDEN and W. J. WANG, “Early detection of gear failure by vibration analysis - I. Calculation of the time– frequency distribution,” Mechanical System and Signal Processing, pp. 193-203, 1991.

[48] W. J. STASZEWSKI, K. WORDEN, and G. R. TOMLINSON, “Time-frequency analysis in gearbox fault detection using the Wigner-Ville distribution and pattern recognition,” Mechanical Systems and Signal Processing 11(5), pp. 673-692, 1997.

[49] S. K. LEE and P. R. WHITE, “Higher order time-frequency analysis and its applications to fault detection in rotating machinery,” Mechanical Systems and Signal Processing 11(4), pp. 637-650, 1997.

[50] S. U. LEE, D. ROBB, and C. BESANT, “The directional Choi-Williams distribution for the analysis of rotor-vibration signals,” Mechanical Systems and Signal Processing 15(4), pp. 789-811, 2001.

[51] C. J. STANDER, P. S. HEYNS, and W. SCHOOMBIE, “Using vibration monitoring for local fault detection on gears operating under fluctuating load conditions,” Mechanical Systems and Signal Processing 16(6), pp. 1005-1024, 2002.

[52] B. YAZICI and G. B. KLIMAN, “An adaptive statistical time-frequency method for detection of broken bars and bearing faults in motors using stator current,” IEEE Trans. Ind. Appl., vol.35, no. 2, pp. 442-452, 1999.

[53] K. KIM and A. G. PARLOS, “Induction motor fault diagnosis based on neuropredictors and wavelet signal processing,” IEEE/ASME Trans. Mechatronics, vol. 7, no. 2, pp. 201-219, 2002.

[54] C. COMBASTEL, S. LESECQ, S. PETROPOL and S. GENTIL, “Model-based and wavelet approaches to induction motor on-line fault detection,” Control Engineering Practice, vol. 10, issue 5, pp. 493-509, 2002.

[55] R. BURNETT, J. F. WATSON, and S. ELDER, “The application of modern signal processing techniques for use in rotor fault detection and location within three-phase induction motors,” in Proc. 1995 IEEE Instrumentation and Measurement Technology Conference (IMTC/95), 1995, pp. 426-431.

[56] M. BLODT, M. CHABERT, J. FAUCHER, and B. DAGUES, “Mechanical Load Fault Detection in Induction Motors by Stator Current Time-Frequency Analysis,” in Proc. IEEE International Conference on Electric Machines and Drives (IEMDC 2005), 2005, pp. 1881-1888.

[57] L. EREN and M. J. DEVANEY, “Motor bearing damage detection via wavelet analysis of the starting current transient,” in Proc. 18th IEEE Instrumentation and Measurement Technology Conference (IMTC 2001), 2001, pp. 1797-1800.

[58] H. DOUGLAS, P. PILLAY, and A. K. ZIARANI, “A new algorithm for transient motor current signature analysis using wavelets,” IEEE Trans. on Ind. Appl., vol. 40, pp. 1361-1368, 2004.

[59] S. RAJAGOPALAN, W. LE ROUX, R. G. HARLEY and T. G. HABETLER, “Diagnosis of potential rotor faults in brushless DC machines,” in Proc. Second International Conference on Power Electronics, Machines and Drives (PEMD 2004), 2004, pp. 668-673.

[60] R. B. RANDALL, “A new method for modeling gear faults,” ASME Journal of Mechanical Design 104, pp. 259-267, 1982.

[61] R. B. RANDALL, “Frequency analysis,” Brüel & Kjaer, Copenhagen, 1977.

[62] A. V. OPPENHEIM, R. W. SCHAFER, and J. R. BUCK, Discrete-Time Signal Processing. Prentice Hall, ISBN: 0137549202, 1999.

[63] P. VAS, Parameter Estimation, Condition monitoring, and diagnosis of electrical machines. Clarendron Press, Oxford, ISBN: 0198593759, 1993.

[64] L. COHEN, “Time-frequency distributions – A review,” in Proc. IEEE, vol. 77, no. 7, pp. 941-981, 1989.

[65] L. COHEN, “Introduction: A Primer on Time–frequency Analysis,”in Time–Frequency Signal Analysis. B. Boashash (ed.), Melbourne: Longman Cheshire, ISBN: 0-582-71286-6, pp. 3-42, 1992.

[66] F. HLAWATSCH and G. F. BOUDREAUX-BARTELS, “Linear and quadratic time-frequency signal representations,” IEEE Signal Process. Mag., vol. 9, pp. 21-67, 1992.

[67] M. VETTERLI and C. HERLEY, “Wavelets and filter banks: theory and design,” IEEE Trans. Signal Process., vol.40, no. 9, pp. 2207-2232, 1992.

[68] S. MALLAT, A Wavelet Tour of Signal Processing. Academic Press, CA, ISBN: 0-12-466606-X, 1999.

[69] J. M. ALLER, T. G. HABETLER, R. G. HARLEY, R. M. TALLAM, and S. B. LEE, “Sensorless speed measurement of AC machines using Analytic Wavelet Transform,” IEEE Trans. Ind. Appl., vol.38, no. 5, pp. 1344-1350, 2002.

[70] L. R. RABINER, “A tutorial on hidden markov models and selected applications in speech recognition,” in Proc. IEEE, vol. 77, no. 2, pp. 257-286, 1989.

[71] E. HATZIPANTELIS and J. PENMAN, “The use of hidden markov models for condition monitoring electrical machines,” in Proc. Sixth International Conference on Electrical Machines and Drives, 1993, pp. 91-96.

[72] L. P. HECK and J. H. MCCLELLAN, “Mechanical system monitoring using hidden markov models,” in Proc. 1991 IEEE International Conference on Acoustics, Speech and Signal Processing, 1991, pp. 1697-1700.

[73] L. M. D. OWSLEY, L. E. ATLAS, and G. D. BERNARD, “Self-organizing feature maps and hidden markov models for machine-tool monitoring,” IEEE Trans. on Signal Process., vol. 45, no. 11, pp. 2787-2798, 1997.

[74] L. WANG, M. G. MEHRABI, and E. KANNATEY-ASIBU, JR., “Hidden markov model-based tool wear monitoring in turning,” J. Manufacturing Science and Engineering, vol. 124, pp. 651-658, 2002.

[75] P. M. T. BROERSEN and S. DE WAELE, “Frequency selective time series analysis,” in Proc. 19th IEEE Instrumentation and Measurement Technology Conference (IMTC 2002), 2002, pp. 775-780.

[76] S. L. MARPLE, JR., Digital Spectral Analysis with Applications. Englewood Cliffs, New Jersey: Prentice-Hall, Inc., ISBN: 0132141493, 1987.

[77] L. B. FERTIG and J. H. MCCLELLAN, "Instantaneous frequency estimation using linear prediction with comparisons to the DESAs," IEEE Signal Process. Lett., vol. 3, no. 2, pp. 54-56, 1996.

[78] S. M. KAY, Modern Spectral Estimation: Theory and Application. Englewood Cliffs, New Jersey: Prentice-Hall, Inc., ISBN: 0130151599, 1988.

[79] S. W. LANG and J. H. MCCLELLAN, "Frequency estimation with maximum entropy spectral estimators," IEEE Trans. on Acoustics, Speech, and Signal Process., vol. ASSP-28, no. 6, pp. 716-724, 1980.

[80] M. NIEDZWIECKI, Identification of Time-Varying Processes. New York: John Wiley & Sons, ISBN: 0471986291, 2000.

[81] J. G. PROAKIS, C. M. RADER, F. LING, M. MOONEN, I. K. PROUDLER, and C. L. NIKIAS, Algorithms for Statistical Signal Processing. Englewood Cliffs, New Jersey: Prentice-Hall, Inc., ISBN: 0130622192, 2002

[82] N. DELPRAT, B. ESCUDIE, P. GUILLEMAIN, R. KROLAND-MARTINET, P. TCHAMITCHIAN, and B. TORRESANI, "Asymptotic wavelets and Gabor analysis: Extraction of instantaneous frequencies," IEEE Trans. Inf. Theory, vol. 3, pp. 644-664, 1992.

[83] WAVELAB802, Reference Manual. [Online]. Available: http://www-stat.stanford.edu/~wavelab, Last Accessed: 17 June, 2006.

[84] L. R. RABINER and B. GOLD, Theory and Application of Digital Signal Processing. Englewood Cliffs, NJ: Prentice-Hall, Inc., ISBN: 0139141014, 1975.

[85] FilterCAD, Software. [Online]. Available: http://www.linear.com/designtools/filtercad.jsp, Last Accessed: 17 June, 2006.

[86] LTC1061 – High Performance Triple Universal Filter Building Block, Linear Technologies Data Sheet. [Online]. Available: http://www.linear.com, Last Accessed: 17 June, 2006.

[87] MAX295, 8th Order, low pass, Switched-Capacitor Filters, Maxim Data Sheet. [Online]. Available: http://pdfserv.maxim-ic.com/en/ds/MAX291-MAX296.pdf, Last Accessed: 17 June, 2006.

[88] FilterPro MFB and Sallen-Key Low-Pass Filter Design Program. [Online]. Available: http://focus.ti.com/lit/an/sbfa001a/sbfa001a.pdf, Last Accessed: 17 June, 2006.

[89] E. J. ROTHWELL, K. M. CHEN, and D. P. NYQUIST, “An adaptive-window-width short-time Fourier transform for visualization of radar target substructure resonances,” IEEE Trans. Antennas Propag., vol. 46, issue 9, pp. 1393-1395, 1998.

[90] T. A. C. M. CLAASEN and W. F. G. MECKLENBRAUKER, “The Wigner distribution – a tool for timr-frequency analysis. Part 1: continuous time signals,” Philips Journal of Research 35, pp. 217-250, 1980.

[91] T. A. C. M. CLAASEN and W. F. G. MECKLENBRAUKER, “The Wigner distribution – a tool for timr-frequency analysis. Part 2: discrete time signals,” Philips Journal of Research 35, pp. 276-300, 1980.

[92] H. I. CHOI and W. J. WILLIAMS, “Improved time-frequency representation of multi-component signals using exponential kernels,” IEEE Trans. on Acoustics, Speech, and Signal Process., vol. 37, no. 6, pp. 862-871, 1989.

[93] Y. ZHAO, L. E. ATLAS, and R. J. MARKS II, “The use of cone-shaped kernels for generalized time-frequency representations of nonstationary signals,” IEEE Trans. on Acoustics, Speech, and Signal Process., vol. 38, no. 7, pp. 1084-1091, 1990.

[94] F. AUGER, P. FLANDRIN, P. GONCALVÈS, and O. LEMOINE, Time-frequency toolbox for use with MATLAB. CNRS France and Rice University, USA, 1996.

[95] ADSP-21061 Data Sheet, Analog Devices, Inc. [Online]. Available: http://www.analog.com/en/prod/0,2877,ADSP%252D21061,00.html, Last Accessed: 17 June, 2006.

[96] Visual DSP++ Evaluation Version 4.0, Analog Devices, Inc. [Online]. Available: http://www.analog.com/processors/resources/crosscore/visualDspDevSoftware.html, Last Accessed: 17 June, 2006.

[97] J. A. RESTREPO and P. BOWLER, “Analysis of Induction Machine Slot Harmonics in the TF Domain,” in Proc. 1st IEEE International Caracas Conference on Devices, Circuits and Systems, 1995, pp. 127-130.

[98] J. A. RESTREPO, T. PÉREZ , M. I. GIMÉNEZ, and V. M. GUZMÁN, “DSP Implementation of an AC-Machine Sensorless Speed Measurement system Using the Wigner Distribution,” in Proc. 7th European Conference on Power Electronics and Applications; 1997.

[99] B. BOASHASH and P. J. BLACK, “An efficient real-time implementation of the Wigner-Ville distribution,” IEEE Trans. on Acoustics, Speech, and Signal Process., vol. 35, no. 11, pp. 1611-1618, 1978.

[100] P. BECHARD, Fault Zone Analysis "Air Gap" in Proc. 2004 Motor Reliability Technical Conference. [Online]. Available: http://www.pdma.com/AirGapFaultZone.pdf, Last Accessed: 17 June, 2006.

[101] False positive. Available: http://en.wikipedia.org/wiki/Type_I_error, Last Accessed: 18 June, 2006.

[102] False negative. Available: http://en.wikipedia.org/wiki/Type_II_error, Last Accessed: 18 June, 2006.

[103] S. RAJAGOPALAN, T. G. HABETLER, R. G. HARLEY, T. SEBASTIAN, and B. LEQUESNE, "Current/voltage based detection of faults in gears coupled to electric motors," in Proc. International Electric Machines and Drives Conference 2005 (IEMDC 05), 2005, 1780-1787. Also accepted for publication in the IEEE Trans. Ind. Appl.

[104] S. RAJAGOPALAN, J. M. ALLER, J. A. RESTREPO, T. G. HABETLER, and R. G. HARLEY, "Diagnosis of Rotor Faults in Brushless DC (BLDC) Motors Operating under Non-Stationary Conditions Using Windowed Fourier Ridges," in Proc. 40th Annual Meeting of the Industry Applications Society (IAS 2005), 2005, pp. 26-33.

[105] S. RAJAGOPALAN, J. A. RESTREPO, J. M. ALLER, T. G. HABETLER, and R. G. HARLEY, "Wigner-Ville Distributions for Detection of Rotor Faults in Brushless DC (BLDC) Motors Operating Under Non-Stationary Conditions," in Proc. International Symposium on Diagnostics for Electric Machines, Power Electronics and Drives (SDEMPED 2005), 2005, CD proceedings.

[106] S. RAJAGOPALAN, J. A. RESTREPO, J. M. ALLER, T. G. HABETLER, and R. G. Harley, "Selecting Time-Frequency Representations for Detecting Rotor Faults in BLDC Motors Operating Under Rapidly Varying Operating Conditions," in Proc. 32nd Annual Conference of the Industrial Electronics Society (IECON 2005), 2005, pp. 2579-2584.

[107] S. RAJAGOPALAN, J. M. ALLER, J. A. RESTREPO, T. G. HABETLER, and R. G. HARLEY, "A novel analytic wavelet ridge detector for dynamic eccentricity detection in BLDC motors under dynamic operating conditions," in Proc. 32nd Annual Conference of the Industrial Electronics Society (IECON 2005), 2005, pp. 1143-1148.

[108] S. RAJAGOPALAN, J. A. RESTREPO, J. M. ALLER, T. G. HABETLER, and R. G. Harley, "Non-Stationary Motor Fault Diagnostics Using Recent Quadratic Time-Frequency Representations," to be presented at the 41th Annual Meeting of the Industry Applications Society (IAS 2006), 2006.

[109] S. RAJAGOPALAN, J. M. ALLER, J. A. RESTREPO, T. G. HABETLER, and R. G. HARLEY, "Diagnosis of Rotor Faults in Brushless DC (BLDC) Motors

Operating under Non-Stationary Conditions," Accepted for publication in the IEEE Trans. Ind. Appl.

[110] W. LE ROUX, S. RAJAGOPALAN, R. G. HARLEY and T. G. HABETLER, "On the detection of rotor faults in permanent magnet machines," in Proc. Electric Machines Technology Symposium 2004 (EMPS2004), 2004.

[111] S. RAJAGOPALAN, T. G. HABETLER, C. KRAL, and F. PIRKER, "Monitoring and Diagnostics for Electric Drivetrain Components in HEVs," in Proc. 2006 SAE World Congress, Detroit, April 2006.

[112] X. HUANG, T. G. HABETLER, and R. G. HARLEY, "Detection of rotor eccentricity faults in closed-loop drive-connected induction motors using an artificial neural network," in Proc. IEEE Power Electronics Specialist Conference 2004 (PESC'04), pp. 913-918, 2004.

[113] R. R. SCHOEN, B. K. LIN, T. G. HABETLER, J. H. SCHLAG, and S. FARAG, " An unsupervised, on-line system for induction motor fault detection using stator current monitoring," IEEE Trans. Ind. Appl., vol.31, issue 6, pp. 1280-1286, 1995.

[114] VFC32 – Voltage-to-frequency and Frequency-to-voltage Converter, Texas Instruments Data Sheet. [Online]. Available: http://focus.ti.com/docs/prod/folders/print/vfc32.html, Last Accessed: 17 June, 2006.

VITA

SATISH RAJAGOPALAN

Satish Rajagopalan was born on December 15, 1975 in Karnataka, India. He attended the University of Madras, India and received his Bachelor of Engineering degree in Electrical and Electronics Engineering in May, 1997. He received the M. S. degree in Electrical Engineering in August 2000 from Iowa State University, Ames, Iowa and was awarded the Research Excellence Award for the best Master's thesis in 2000. During the course of his M.S., Satish also interned with Rockwell Collins Inc., where he worked on the design and analysis of low voltage power supplies. From 2000 to 2001, he was employed by Baldor Motors and Drives Inc. as a Power Electronics Engineer, where he was involved in the design of electric motor drives. In January of 2002, Satish began his graduate studies at the Georgia Institute of Technology in Atlanta, Georgia. He was awarded the Ph.D. degree in electrical engineering in June of 2006. While at Georgia Tech, Satish was employed as a Graduate Research Assistant and worked on impact of battery chargers on airport distribution systems and development of power converters for portable power systems.